STATE OF THE CLIMATE IN 2023

THE ARCTIC

M. L. Druckenmiller, R. L. Thoman, and T. A. Moon, Eds.

Special Online Supplement to the *Bulletin of the American Meteorological Society*, Vol. 105, No. 8, August 2024

https://doi.org/10.1175/BAMS-D-24-0101.1

Corresponding author: Matthew L. Druckenmiller / druckenmiller@colorado.edu

STATE OF THE CLIMATE IN 2023
The Arctic

Editors

Jessica Blunden
Tim Boyer

Chapter Editors

Anthony Arguez
Josh Blannin
Peter Bissolli
Kyle R. Clem
Howard J. Diamond
Matthew L. Druckenmiller
Robert J. H. Dunn
Catherine Ganter
Nadine Gobron
Gregory C. Johnson
Rick Lumpkin
Rodney Martinez
Ademe Mekonnen
John B. Miller
Twila A. Moon
Marilyn N. Raphael
Carl J. Schreck III
Laura Stevens
Richard L. Thoman
Kate M. Willett
Zhiwei Zhu

Technical Editor

Lukas Noguchi

BAMS Special Editor for Climate

Timothy DelSole

American Meteorological Society

Cover Credit:
Windblown icebergs in Kong Oscars Harbor at Tasiilaq, Greenland, most likely sourced from the peripheral glaciers and ice caps feeding Angmagssalik Fjord. (Photo credit: Kristin Poinar, 10 June 2023.)

How to cite this document:
The Arctic is one chapter from the *State of the Climate in 2023* annual report and is available from https://doi.org/10.1175/BAMS-D-24-0101.1. Compiled by NOAA's National Centers for Environmental Information, *State of the Climate in 2023* is based on contributions from scientists from around the world. It provides a detailed update on global climate indicators, notable weather events, and other data collected by environmental monitoring stations and instruments located on land, water, ice, and in space. The full report is available from https://doi.org/10.1175/2024BAMSStateoftheClimate.1.

Citing the complete report:
Blunden, J. and T. Boyer, Eds., 2024: "State of the Climate in 2023". *Bull. Amer. Meteor. Soc.*, **105** (8), Si–S483 https://doi.org/10.1175/2024BAMSStateoftheClimate.1.

Citing this chapter:
M. L. Druckenmiller, R. L. Thoman, and T. A. Moon, Eds., 2024: The Arctic [in "State of the Climate in 2023"]. *Bull. Amer. Meteor. Soc.*, **105** (8), S277–S330, https://doi.org/10.1175/BAMS-D-24-0101.1.

Citing a section (example):
Burgess, D., G. Wolken, B. Wouters, L. M. Andreassen, C. Florentine, J. Kohler, B. Luks, F. Pálsson, L. Sass, L. Thomson, and T. Thorsteinsson, 2024: Glaciers and ice caps outside Greenland [in "State of the Climate in 2023"]. *Bull. Amer. Meteor. Soc.*, **105** (8), S307–S310, https://doi.org/10.1175/BAMS-D-24-0101.1.

Editor and Author Affiliations (alphabetical by name)

Andreassen, Liss Marie, Section for Glaciers, Ice and Snow, Norwegian Water Resources and Energy Directorate, Oslo, Norway

Ballinger, Thomas J., International Arctic Research Center, University of Alaska Fairbanks, Fairbanks, Alaska

Berner, Logan T., School of Informatics, Computing, and Cyber Systems, Northern Arizona University, Flagstaff, Arizona

Bernhard, Germar H., Biospherical Instruments Inc., San Diego, California

Bhatt, Uma S., Geophysical Institute, University of Alaska Fairbanks, Fairbanks, Alaska

Bigalke, Siiri, Plant, Soils and Climate Department, Utah State University, Logan, Utah

Bjerke, Jarle W., Norwegian Institute for Nature Research, Trondheim, Norway; FRAM – High North Research Centre for Climate and the Environment, Tromsø, Norway

Box, Jason E., Geological Survey of Denmark and Greenland (GEUS), Copenhagen, Denmark

Brettschneider, Brian, NOAA/NWS Alaska Region, Anchorage, Alaska

Brubaker, Mike, Alaska Native Tribal Health Consortium, Anchorage, Alaska

Burgess, David, Geological Survey of Canada, Natural Resources Canada, Ottawa, Canada

Butler, Amy H., NOAA Chemical Sciences Laboratory, Boulder, Colorado

Christiansen, Hanne H., Arctic Geophysics Department, University Centre in Svalbard, Longyearbyen, Norway; Geology Department, University Centre in Svalbard, Longyearben, Norway

Decharme, Bertrand, Centre National de Recherches Météorologiques, Météo-France/CNRS, Toulouse, France

Derksen, Chris, Climate Research Division, Environment and Climate Change Canada, Toronto, Canada

Divine, Dmitry, Norwegian Polar Institute, Fram Centre, Tromsø, Norway

Drost Jensen, Caroline, Danish Meteorological Institute, Copenhagen, Denmark

Druckenmiller, Matthew L., National Snow and Ice Data Center, Cooperative Institute for Research in Environmental Sciences, University of Colorado, Boulder, Boulder, Colorado

Elias Chereque, Alesksandra, Department of Physics, University of Toronto, Toronto, Canada

Epstein, Howard E., Department of Environmental Sciences, University of Virginia, Charlottesville, Virginia

Farrell, Sinead, Department of Geographical Sciences, University of Maryland, College Park, Maryland

Fausto, Robert S., Geological Survey of Denmark and Greenland (GEUS), Copenhagen, Denmark

Fettweis, Xavier, University of Liège, Liège, Belgium

Fioletov, Vitali E., Environment and Climate Change Canada, Toronto, Canada

Florentine, Caitlyn, Northern Rocky Mountain Science Center, U.S. Geological Survey, Bozeman, Montana

Forbes, Bruce C., Arctic Centre, University of Lapland, Rovaniemi, Finland

Frost, Gerald V. (JJ), Alaska Biological Research, Inc., Fairbanks, Alaska

Gerland, Sebastian, Norwegian Polar Institute, Fram Centre, Tromsø, Norway

Grooß, Jens-Uwe, Forschungszentrum Jülich (IEK-7), Jülich, Germany

Hanna, Edward, Department of Geography and Lincoln Climate Research Group, Lincoln, United Kingdom

Hanssen-Bauer, Inger, Norwegian Meteorological Institute, Oslo, Norway

Heatta, Máret J., Saami Council, Kárášjohka, Norway

Hendricks, Stefan, Alfred Wegener Institute, Helmholtz Centre for Polar and Marine Research, Bremerhaven, Germany

Ialongo, Iolanda, Finnish Meteorological Institute, Helsinki, Finland

Isaksen, Ketil, Norwegian Meteorological Institute, Oslo, Norway

Jeuring, Jelmer, Norwegian Meteorological Institute, Bergen, Norway

Jia, Gensuo, Institute of Atmospheric Physics, Chinese Academy of Sciences, Beijing, China

Johnsen, Bjørn, Norwegian Radiation and Nuclear Safety Authority, Østerås, Norway

Kaleschke, Lars, Alfred Wegener Institute, Helmholtz Centre for Polar and Marine Research, Bremerhaven, Germany

Kim, Seong-Joong, Korea Polar Research Institute, Incheon, South Korea

Kohler, Jack, Norwegian Polar Institute, Fram Centre, Tromsø, Norway

Labe, Zachary, M., Atmospheric and Oceanic Sciences Program, Princeton University, Princeton, New Jersey

Lader, Rick, International Arctic Research Center, University of Alaska Fairbanks, Fairbanks, Alaska

Lakkala, Kaisa, Finnish Meteorological Institute, Sodankylä, Finland

Lara, Mark J., Department of Plant Biology, University of Illinois, Urbana, Illinois; Department of Geography, University of Illinois, Urbana, Illinois

Lee, Simon H., Department of Applied Physics and Applied Mathematics, Columbia University, New York, New York

Loomis, Bryant D., NASA Goddard Space Flight Center, Greenbelt, Maryland

Luks, Bartłomiej, Institute of Geophysics, Polish Academy of Sciences, Warsaw, Poland

Luojus, Kari, Arctic Research Centre, Finnish Meteorological Institute, Helsinki, Finland

Macander, Matthew J., Alaska Biological Research, Inc., Fairbanks, Alaska

Magnússon, Rúna Í., Plant Ecology and Nature Conservation Group, Wageningen University & Research, Wageningen, Netherlands

Mankoff, Ken D., Business Integra, New York, New York; NASA Goddard Institute for Space Studies, New York, New York

Manney, Gloria, NorthWest Research Associates, Inc, Socorro, New Mexico; Department of Physics, New Mexico Institute of Mining and Technology, Socorro, New Mexico

Medley, Brooke, Cryospheric Sciences Laboratory, NASA Goddard Space Flight Center, Greenbelt, Maryland

Meier, Walter N., National Snow and Ice Data Center, Cooperative Institute for Research in Environmental Sciences, University of Colorado, Boulder, Colorado

Montesano, Paul M., NASA Goddard Space Flight Center, Greenbelt, Maryland

Moon, Twila A., National Snow and Ice Data Center, Cooperative Institute for Research in Environmental Sciences, University of Colorado, Boulder, Colorado

Mote, Thomas L., Department of Geography, University of Georgia, Athens, Georgia

Mudryk, Lawrence, Climate Research Division, Environment and Climate Change Canada, Toronto, Canada

Müller, Rolf, Forschungszentrum Jülich (IEK-7), Jülich, Germany

Neigh, Christopher S. R., NASA Goddard Space Flight Center, Greenbelt, Maryland

Nyland, Kelsey E., Department of Geography, George Washington University, Washington, DC

Overland, James E., NOAA Pacific Marine Environmental Laboratory, Seattle, Washington

Pálsson, Finnur, Institute of Earth Sciences, University of Iceland, Reykjavík, Iceland

Poinar, Kristin, University at Buffalo, Buffalo, New York

Perovich, Donald K., University of Dartmouth, Hanover, New Hampshire

Petty, Alek, NASA Goddard Space Flight Center, Greenbelt, Maryland

Phoenix, Gareth K., School of Biosciences, University of Sheffield, Sheffield, United Kingdom

Ricker, Robert, NORCE Norwegian Research Centre, Tromsø, Norway

Romanovsky, Vladimir E., Geophysical Institute, University of Alaska Fairbanks, Fairbanks, Alaska; Earth Cryosphere Institute, Tyumen Science Center, Tyumen, Russia

Sass, Louis, Alaska Science Center, U.S. Geological Survey, Anchorage, Alaska

Scheller, Johan H., Department of Ecoscience, Arctic Research Centre Aarhus University, Roskilde, Denmark

Serreze, Mark C., National Snow and Ice Data Center, Cooperative Institute for Research in Environmental Sciences, University of Colorado, Boulder, Colorado

Shiklomanov, Nikolay I., Department of Geography, George Washington University, Washington, DC

Editor and Author Affiliations (continued)

Smith, Benjamin E., Polar Science Center, Applied Physics Laboratory, University of Washington, Seattle, Washington

Smith, Sharon L., Geological Survey of Canada, Natural Resources Canada, Ottawa, Canada

Streletskiy, Dmitry A., Department of Geography, George Washington University, Washington, DC

Svendby, Tove, Norwegian Institute for Air Research (NILU), Kjeller, Norway

Tedesco, Marco, Lamont-Doherty Earth Observatory, Columbia University, Palisades, New York; NASA Goddard Institute of Space Studies, New York, New York

Thoman, Richard L., International Arctic Research Center, University of Alaska Fairbanks, Fairbanks, Alaska

Thomson, Laura, Queen's University, Kingston, Canada

Thorsteinsson, Thorsteinn, Icelandic Meteorological Office, Reykjavík, Iceland

Tian-Kunze, Xiangshan, Alfred Wegener Institute, Helmholtz Centre for Polar and Marine Research, Bremerhaven, Germany

Timmermans, Mary-Louise, Yale University, New Haven, Connecticut

Tømmervik, Hans, Norwegian Institute for Nature Research, Trondheim, Norway; FRAM – High North Research Centre for Climate and the Environment, Tromsø, Norway

Waigl, Christine F., Geophysical Institute, University of Alaska Fairbanks, Fairbanks, Alaska

Walker, Donald (Skip) A., Institute of Arctic Biology, University of Alaska Fairbanks, Fairbanks, Alaska

Walsh, John E., International Arctic Research Center, University of Alaska Fairbanks, Fairbanks, Alaska

Wang, Muyin, NOAA Pacific Marine Environmental Laboratory, Seattle, Washington, Cooperative Institute for Climate, Ocean, and Ecosystem Studies, University of Washington, Seattle, Washington

Webster, Melinda, Polar Science Center, Applied Physics Laboratory, University of Washington, Seattle, Washington

Wehrlé, Adrian, University of Zürich, Zürich, Switzerland

Wolken, Gabriel J., Alaska Division of Geological & Geophysical Surveys, Fairbanks, Alaska; University of Alaska Fairbanks, Fairbanks, Alaska

Wouters, Bert, Department of Geoscience & Remote Sensing, Delft University of Technology, Delft, The Netherlands

Yang, Dedi, Environmental Sciences Division, Oak Ridge National Laboratory, Oak Ridge, Tennessee

Editorial and Production Team

Allen, Jessicca, Graphics Support, Cooperative Institute for Satellite Earth System Studies, North Carolina State University, Asheville, North Carolina

Camper, Amy V., Graphics Support, Innovative Consulting and Management Services, LLC, NOAA/NESDIS National Centers for Environmental Information, Asheville, North Carolina

Haley, Bridgette O., Graphics Support, NOAA/NESDIS National Centers for Environmental Information, Asheville, North Carolina

Hammer, Gregory, Content Team Lead, Communications and Outreach, NOAA/NESDIS National Centers for Environmental Information, Asheville, North Carolina

Love-Brotak, S. Elizabeth, Lead Graphics Production, NOAA/NESDIS National Centers for Environmental Information, Asheville, North Carolina

Ohlmann, Laura, Technical Editor, Innovative Consulting and Management Services, LLC, NOAA/NESDIS National Centers for Environmental Information, Asheville, North Carolina

Noguchi, Lukas, Technical Editor, Innovative Consulting and Management Services, LLC, NOAA/NESDIS National Centers for Environmental Information, Asheville, North Carolina

Riddle, Deborah B., Graphics Support, NOAA/NESDIS National Centers for Environmental Information, Asheville, North Carolina

Veasey, Sara W., Visual Communications Team Lead, Communications and Outreach, NOAA/NESDIS National Centers for Environmental Information, Asheville, North Carolina

5. Table of Contents

5. THE ARCTIC

M. L. Druckenmiller, R. L. Thoman, and T. A. Moon, Eds.

a. Overview

—M. L. Druckenmiller, R. L. Thoman, and T. A. Moon

Arctic observations in 2023 provided clear evidence of rapid and pronounced climate and environmental change, shaped by past and ongoing human activities that release greenhouse gases into the atmosphere and push the broader Earth system into uncharted territory. This chapter provides a snapshot of 2023 and summarizes decades-long trends observed across the Arctic, including warming surface air and sea-surface temperatures, decreasing snow cover, diminishing sea ice, thawing permafrost, and continued mass loss from the Greenland Ice Sheet and Arctic glaciers. These changes are driving a transition to a wetter, greener, and less frozen Arctic, with serious implications for Arctic peoples and ecosystems, as well as for low- and midlatitudes.

Average surface air temperatures for 2023 (January–December) for the Arctic as a whole were the fourth highest since 1900, with the Arctic summer (July–September) being the warmest on record. These unprecedented surface temperatures aligned with record-positive geopotential height anomalies in the polar troposphere, which have been increasing alongside warming air temperatures since 1958, indicating the strong connection between long-term atmospheric circulation and regional temperature patterns.

Large-scale atmospheric circulation also strongly influences year-to-year variability and regional differences. For example, in 2023, a colder-than-normal spring across Alaska slowed snowpack and sea-ice melt, while parts of north-central Canada experienced their highest spring average temperatures on record. Short-term atmospheric events can also influence Arctic and midlatitude connections. A major Arctic sudden stratospheric warming (SSW) event in February 2023 is described in Sidebar 5.1—an event that can increase the likelihood of midlatitude cold-air outbreaks for several weeks to months, influencing subseasonal-to-seasonal predictability for midlatitude surface weather.

Warming seasonal air temperatures together with the timing and extent of summer sea-ice loss significantly influence multi-decadal trends and the substantial regional and year-to-year variability seen across both marine and terrestrial systems. Driven by accelerated sea-ice retreat and melt that started in July, the September 2023 sea-ice monthly extent, which is the lowest monthly extent of the year, was 4.37 million square kilometers—about 10% lower than the past two years and overall the fifth lowest in the 45-year satellite record. Additionally, the 17 lowest September sea-ice monthly extents have all occurred in the last 17 years. Spring and early-summer sea-ice loss exposes the dark ocean surface and allows time for solar heating of the ocean. Linked to early sea-ice loss, average sea-surface temperatures for August 2023 were much higher than the 30-year average in the Barents, Kara, Laptev, and Beaufort Seas. Anomalously low August 2023 sea-surface temperatures were observed in Baffin Bay and parts of the Greenland, Bering, and Chukchi Seas. Despite considerable year-to-year variability, almost all Arctic Ocean and marginal seas studied show a statistically significant 1982–2023 warming trend.

On land, the Arctic tundra is greening due to its sensitivity to rapidly increasing summer temperatures, as well as to rapidly evolving sea-ice, snow, and permafrost conditions. In 2023, circumpolar average peak tundra greenness was the third highest in the 24-year Moderate Resolution Imaging Spectroradiometer (MODIS) satellite record, a slight decline from the previous year. Closely aligned with air temperatures and nearshore sea-ice anomalies, peak vegetation greenness in 2023 was much higher than usual in the North American tundra, particularly in

the Beaufort Sea region. In contrast, tundra greenness was relatively low in the Eurasian Arctic, particularly in northeastern Siberia.

Long-term changes in permafrost conditions are also largely controlled by changes in air temperature. Across all Arctic regions, permafrost temperatures and active layer thickness (i.e., thickness of the soil layer above the permafrost that seasonally thaws and freezes) continue to increase on decadal time scales. In 2023, permafrost temperatures were the highest on record at over half of the reporting sites across the Arctic. Permafrost thaw disrupts Arctic communities and infrastructure and can also affect the rate of greenhouse gas release to the atmosphere, potentially accelerating global warming.

Analyses of Arctic precipitation reveal additional connections between a changing atmosphere and land. Precipitation in 2023 was above normal in all seasons for the Arctic as a whole, with short-duration heavy precipitation events breaking existing records at various locations. Arctic precipitation in the past year was also marked by important seasonal and regional variations. Unusually low precipitation and high temperatures produced severe drought and contributed to the record-breaking wildfire season in Canada's Northwest Territory. Snowpack in early spring 2023 was above normal for North America and Eurasia, but then rapid snow loss in much of the Arctic resulted in record-low average snow-water equivalent for the North American Arctic in May and near-record-low snow cover for the Eurasian Arctic in June.

Precipitation patterns also influence the Greenland Ice Sheet. Above-average snowfall over parts of the Greenland Ice Sheet between autumn 2022 and spring 2023 contributed to a relatively low (for the twenty-first century) total mass loss from the Greenland Ice Sheet despite extensive late-June-to-September ice melt. So, while the Greenland Ice Sheet lost mass in the past year, as it has every year since 1998, the loss for September 2022 to August 2023 was much lower than the 22-year average and similar to that of 2020/21. However, the cumulative melt-day area during summer 2023 was the second-highest in the 45-year satellite observational record.

Beyond the Greenland Ice Sheet, the Arctic's other glaciers and ice caps show a continuing trend of significant ice loss, especially in Alaska and Arctic Canada. All of the 25 monitored Arctic glaciers reported in this chapter for the 2022/23 mass balance year show an annual loss of ice, and for many glaciers these data indicate continued rapid wastage with substantial total contributions to global sea level.

The exceptionally warm Arctic summer alongside persistent long-term climate changes contributed to a range of societal and environmental impacts in 2023 (see Sidebars 5.2 and 7.1), providing stark reminders of the varied climate disruptions that Arctic peoples and broader societies increasingly face. For example, Canada experienced its worst national wildfire season on record. Multiple communities in the Northwest Territories were evacuated during August, including more than 20,000 people from the capital city of Yellowknife. In August 2023 near Juneau, Alaska, a glacial lake on a tributary of the Mendenhall Glacier burst through its ice dam and caused unprecedented flooding and severe property damage on Mendenhall River, a direct result of dramatic glacial thinning over the past 20 years. With increasing seasonal shifts and widespread disturbances influencing the flora, fauna, ecosystems, and peoples of the Arctic, the need for ongoing observation and collaborative research and adaptation has never been higher.

Special Note: This chapter includes a focus on glaciers and ice caps outside of Greenland (section 5h), which alternates yearly with a section on Arctic river discharge, as the scales of regular observation for both of these climate components are better suited for reporting every two years.

b. Atmosphere

—A. H. Butler, S. H. Lee, G. H. Bernhard, V. E. Fioletov, J.-U. Grooß, I. Ialongo, B. Johnsen, K. Lakkala, R. Müller, T. Svendby, and T. J. Ballinger

The Arctic is warming rapidly, not only at the surface but vertically throughout the troposphere (Cohen et al. 2020). Against the background of long-term warming, the atmospheric circulation contributes to the large year-to-year variability in regional temperature and precipitation patterns across the Arctic. The chemical composition in the Arctic stratosphere, which overlies the troposphere, may also have important climate effects (Polvani et al. 2020; Friedel et al. 2022). The Arctic atmosphere in 2023 was marked by a major sudden stratospheric warming (SSW) in February (Sidebar 5.1) and a persistent anticyclonic high-pressure system during summer that corresponded to record surface temperatures over the Arctic (section 5c), higher-than-normal melt days in Greenland (section 5g), and enhanced wildfire activity in the Northwest Territories (see Sidebar 7.1 for details).

One measure of large-scale atmospheric circulation is geopotential height, which is the altitude of a given atmospheric pressure (Fig. 5.1). The geopotential height tends to be higher where the atmosphere is warmer and lower where it is colder. In general, when the polar cap (60°N–90°N) averaged geopotential heights (PCHs) are anomalously positive, the stratospheric polar winds are weaker than normal, and the tropospheric jet stream is shifted equatorward (and vice versa when the PCHs are anomalously negative). Therefore, the PCHs encapsulate both the thermodynamic and dynamic variability of the high-latitude atmosphere and indicate when the polar atmosphere is vertically coupled (i.e., have the same-signed anomalies from the surface to the upper stratosphere). In 2023 (Fig. 5.1), a major SSW is evident as positive anomalies that first appeared in the stratosphere in February and descended to the troposphere (Sidebar 5.1). The other notable feature is a period of

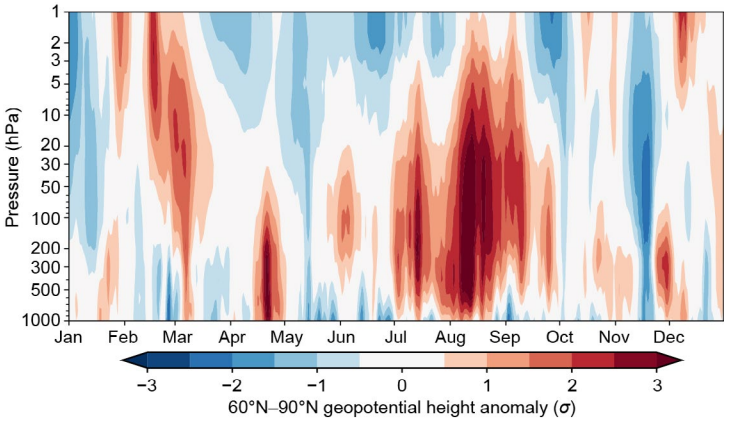

Fig. 5.1. Vertical profile of daily Arctic polar cap (60°N–90°N) standardized geopotential height anomalies (hPa) during 2023. Anomalies are shown with respect to a 30-day centered running-mean 1991–2020 climatology and standardized at each pressure level by the standard deviation of each calendar day during 1991–2020 (smoothed with a 30-day running mean). Data are from once-daily 0000 UTC ERA5 reanalysis (Hersbach et al. 2020).

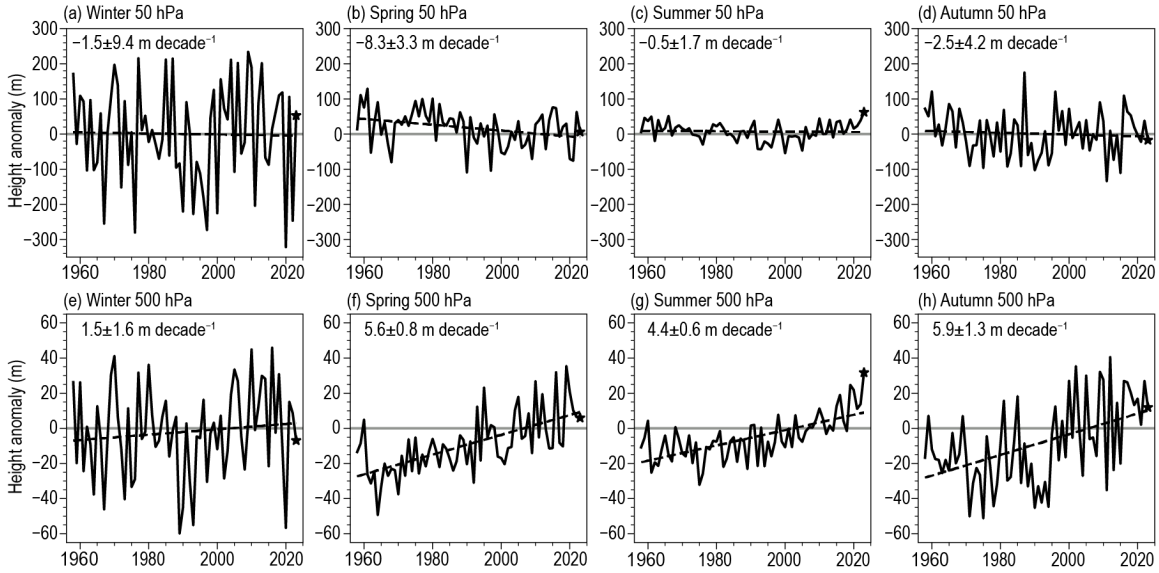

Fig. 5.2. Time series over the 1958–2023 period of polar-cap averaged height anomalies (m) at (a)–(d) 50 hPa and (e)–(h) 500 hPa for the four seasons: (a),(e) winter (JFM), (b),(f) spring (AMJ), (c),(g) summer (JAS), and (d),(h) autumn (OND). The dashed line is the linear least-squares fit, where the trend value ± the standard error of the trend (m decade^{-1}) is shown in the upper left. Geopotential height anomaly data are from monthly-mean ERA5 reanalysis; anomalies are calculated relative to the 1991–2020 climatology. The 2023 values are marked by a star.

persistent, record-high PCH from July to September that extended vertically from the surface to the mid-stratosphere.

Figure 5.2 illustrates the large year-to-year variability of the Arctic atmospheric circulation, particularly in winter, and places 2023 in the context of the historical record. The 2023 PCH anomalies in the troposphere (500 hPa) and stratosphere (50 hPa) were generally close to 1991–2020 climatological values in winter (January–March), spring (April–June), and autumn (October–December); however, record positive PCH anomalies in both the troposphere and stratosphere were observed in summer (July–September). In the troposphere, the record-high summer value is consistent with a significant linear trend in summer towards increasing tropospheric heights and thus warming air temperatures since 1958 (also evident in spring and autumn). In the stratosphere, linear trends since 1958 are negative in all seasons but generally not significant, except in spring (indicative of cooling stratospheric temperatures).

1. THE ARCTIC TROPOSPHERE IN 2023

Figure 5.3 shows the seasonally averaged 500-hPa geopotential height and wind anomalies across the Arctic in 2023. Winter (Fig. 5.3a) was marked by anomalously positive heights near the North Pacific and central Arctic and anomalously negative heights across northeastern Eurasia and North America. This pattern was associated both with La Niña teleconnections and the downward coupling of the stratospheric anomalies following the SSW (Fig. 5.1).

Spring (Fig. 5.3b) was characterized by negative height anomalies over the central Arctic and Alaska, associated with anomalous cold, and positive height anomalies over Canada and Scandinavia, associated with anomalous warmth. However, the seasonal average does not reflect strong monthly variations that occurred. In particular, PCH anomalies at 500 hPa were at their second most positive value since 1958 for April but were moderately negative in May (Fig. 5.1).

Summer (Fig. 5.3c) exhibited strongly anomalous positive heights (anticyclonic wind flow) across a broad region of the Arctic. This is consistent with the observed record-high surface temperatures (section 5c). The persistence and vertical extent (Fig. 5.1) of positive height anomalies likely contributed to higher-than-normal melt days in Greenland (section 5g) and enhanced wildfire activity in the Northwest Territories (see Sidebar 7.1).

A notable feature of autumn (Fig. 5.3d) was the presence of strongly negative height anomalies over the Scandinavian region, linked to cold anomalies there. Height anomalies were otherwise broadly positive, particularly over Canada, where the associated strong anticyclonic wind anomalies likely contributed (via advection) to above-normal temperatures over the Canadian Arctic Archipelago (section 5c).

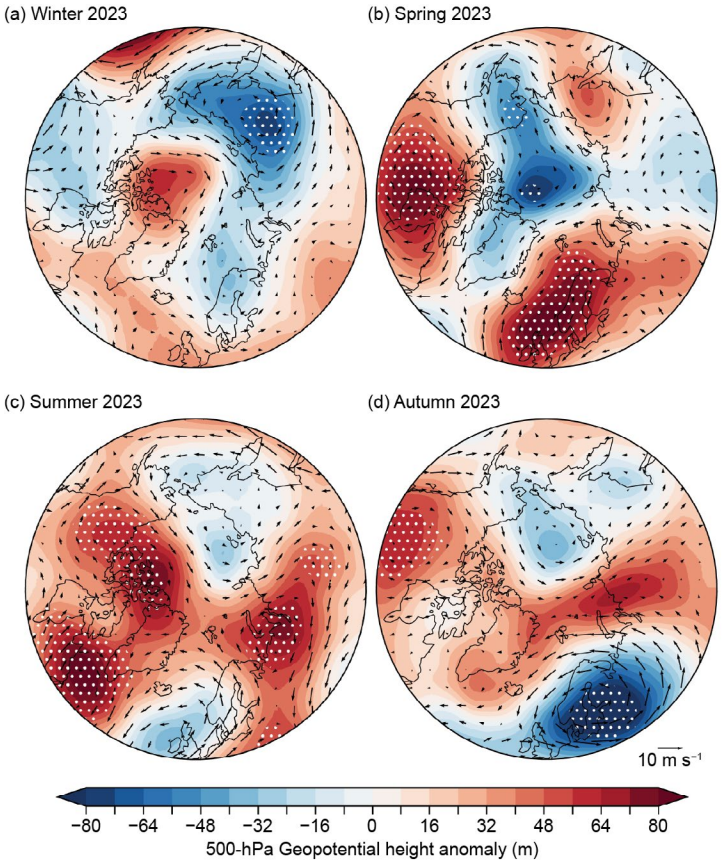

Fig. 5.3. 500-hPa geopotential height (m; shading) and 200-hPa wind (m s^{-1}; vectors) anomalies for (a) winter, (b) spring, (c) summer, and (d) autumn. Anomalies are calculated relative to the 1991–2020 climatology. Stippling indicates that the anomaly exceeds ±2 std. dev. of the 1991–2020 mean. The dashed circle indicates the 60°N latitude, and the area within denotes the polar-cap region. (Source: ERA5 reanalysis.)

2. THE ARCTIC STRATOSPHERE IN 2023

In January 2023, the Arctic stratospheric polar vortex was anomalously strong and cold, leading to strong chlorine activation and initiating chemical ozone loss. This was interrupted, however,

by a major SSW on 16 February (Sidebar 5.1), which resulted in higher-than-average polar total ozone column (TOC) in March. The stratospheric winds at 10 hPa and 60°N weakly returned to westerlies after the SSW and had a slightly later-than-average spring transition to easterly summer conditions. After the westerly winds returned in autumn, their strength stayed near climatological values until November when they strengthened for a couple of weeks (Fig. 5.1), setting near-records for daily zonal-mean wind speeds at 10 hPa and 60°N.

March has historically been the month with the largest potential for chemical ozone depletion in the Arctic (WMO 2022). In March 2023, the minimum Arctic daily TOC was 3.5% (13 Dobson units; DU) above the average since the start of satellite observations in 1979 (Fig. 5.4a). While the recovery of Arctic TOC to pre-1979 levels is expected due to the phase-out of ozone-depleting substances by the Montreal Protocol, it is difficult to detect due to large year-to-year variability (WMO 2022). Spatially, Arctic TOC anomalies varied between −8% and +24% but stayed within 2 std. dev. of past observations from the Ozone Monitoring Instrument (OMI; 2005–22), with the exception of a small area in northern Scandinavia and the adjacent Barents Sea (Fig. 5.4b). This enhancement of TOC was related to the February 2023 SSW, which transported ozone into the polar stratosphere and raised stratospheric temperatures enough to halt chemical processing and ozone loss.

Anomalies in monthly averages of the noontime ultraviolet (UV) Index (a measure of the intensity of solar ultraviolet radiation in terms of causing erythema [sunburn] in human skin) for March 2023 varied spatially between −55% and +67% and generally did not exceed 2 std. dev. of past OMI (2005–22) observations (Fig. 5.4c). Areas with high UV index values roughly match areas with low TOCs and vice versa, but UV index anomalies have larger spatial variability because of their added dependence on clouds (Bernhard et al. 2023). Anomalies calculated from satellite data (OMI instrument) and ground-based measurements generally agree well (Fig. 5.4c). Differences in excess of 5% can be explained by coastal (Andøya: OMI anomaly −6%; ground-based anomaly 0%) or urban (Trondheim: OMI anomaly −6%; ground-based anomaly +2%) effects.

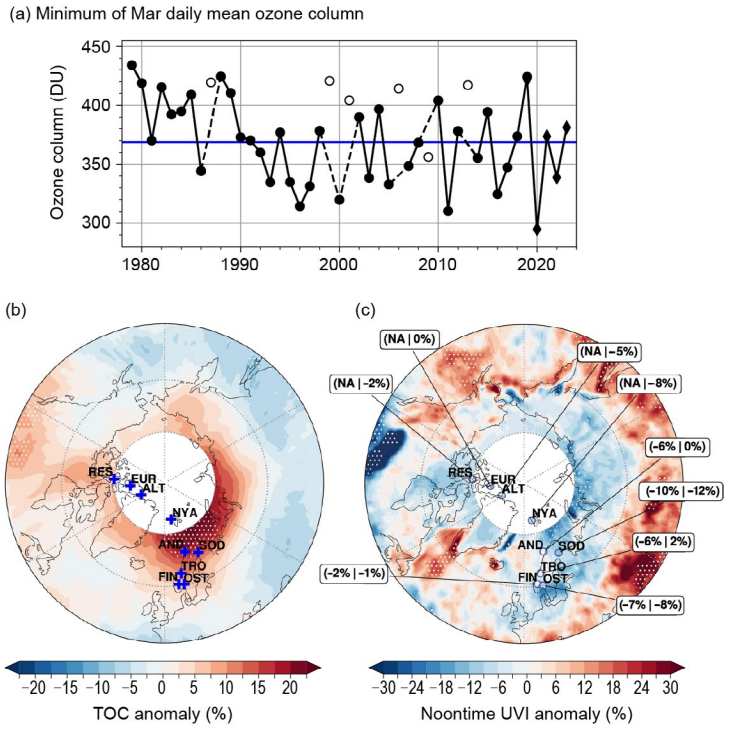

Fig. 5.4. (a) Time series of the minimum daily-mean total ozone column (TOC; Dobson units, DU) for March poleward of 63°N equivalent latitude, which represents the area enclosed by the stratospheric polar vortex (Butchart and Remsberg 1986) and is determined using ERA5 reanalysis data (adapted from Müller et al. [2008] and WMO [2022]). The blue line indicates the average TOC for 1979–2023. Open circles represent years in which the polar vortex was not well-defined in March. Ozone data for 1979–2019 are based on the combined NIWA-BS total column ozone database version 3.5.1 (Bodeker and Kremser 2021). Ozone data for 2020–23 are from the Ozone Monitoring Instrument (OMI). Monthly mean anomaly maps of (b) total ozone column (%) and (c) noontime ultraviolet index (UVI; %) for Mar 2023 relative to 2005–22 means, based on the OMTO$_3$ Version 3 total ozone product (Bhartia and Wellemeyer 2002), which is derived from OMI measurements. (c) compares UVI anomalies from OMI (first value in parenthesis) with ground-based measurements at nine locations (second value presented). Site acronyms of ground stations are ALT: Alert; EUR: Eureka; NYA: Ny-Ålesund; RES: Resolute; AND: Andøya; SOD: Sodankylä; TRO: Trondheim; FIN: Finse; and OST: Østerås. White areas centered at the North Pole indicate latitudes where OMI data are not available because of polar darkness. Stippling in (b) and (c) indicates pixels where anomalies exceed ±2 std. dev. of the 2005–22 OMI measurement climatology.

Sidebar 5.1: The February 2023 major sudden stratospheric warming

S. H. LEE, G. MANNEY, AND A. H. BUTLER

A major sudden stratospheric warming (SSW) occurred in the Arctic on 16 February 2023. Major SSWs, which occur in the Arctic on average six times per decade, are characterized by a rapid warming of the Arctic stratosphere by as much as 50°C in less than a week and a breakdown and reversal of the mean westerly circulation of the stratospheric polar vortex. Sudden stratospheric warming events induce long-lasting impacts on stratospheric chemical composition (notably ozone; section 5b) and can increase the likelihood of midlatitude cold-air outbreaks for several weeks to two months afterward, acting as a source of subseasonal-to-seasonal predictability for midlatitude surface weather (Domeisen et al. 2020).

CAUSE AND EVOLUTION OF THE EVENT

The SSW in February 2023 was the fourth major SSW in six consecutive winters, part of a recent clustering of events following no major SSWs during the preceding four winters from 2013/14 to 2016/17. The major 2023 SSW was preceded by a minor warming during the last few days of January that was driven by a pulse of enhanced upward-propagating planetary wave activity (Fig. SB5.1a, shading) that weakened the zonal-mean zonal winds in the mid-stratosphere to ~10 m s^{-1} (Fig. SB5.1a, contours). Around 14 February, another pulse of anomalous wave activity confined mostly within the stratosphere fully disrupted the vortex, and the winds at 10 hPa and 60°N reversed from westerly to easterly on 16 February, marking the date of the major SSW. During an SSW, the polar vortex either splits into two or more smaller vortices or is displaced away from the Arctic. The February 2023 SSW fell into the latter category, with the vortex in the stratosphere displaced toward Eurasia.

Because the SSW was not preceded by sustained anomalous tropospheric wave activity, the circulation anomalies prior to the event (Fig. SB5.1b) do not strongly resemble precursors of many SSWs. Nonetheless, pressure near the Aleutian Islands was slightly lower than normal during this time, while an anomalous anticyclone extended across parts of northwest Europe. Both of these features have been shown to contribute to SSWs by constructively interfering with the mean stationary wave pattern in the troposphere (Martius et al. 2009; Garfinkel et al. 2010).

At 10 hPa, the winds then returned to westerly during 22–23 February, reversed back to easterly on 24 February, became westerly again on 26 February, and then easterly once again through 10 March. Although several zonal wind reversals occurred, these all formed part of a single SSW event. Such fluctuations occasionally occur during SSWs, but are not typical. The multiple zonal wind reversals resulted from continued wave activity (Fig. SB5.1a) that eventually destroyed the vortex in the lower to mid-stratosphere sufficiently (Karpechko et al. 2017) for likely downward impacts on the troposphere in early March.

INFLUENCE ON WEATHER PATTERNS AND THEIR PREDICTABILITY

Following the February 2023 SSW, there was no immediate coupling between the stratosphere and the troposphere; in fact, for the first two weeks after the SSW, geopotential heights over the Arctic in the troposphere (below ~6 km) were anomalously low, in direct contrast to those in the stratosphere. However, during the first half of March, a brief period of stratosphere–troposphere coupling occurred, characterized by a negative North Atlantic Oscillation pattern at the surface (Fig. SB5.1c) as is typical following SSWs. The coupling occurred around 28 February together with the downward propagation of the weakened vortex into the lower stratosphere. This is consistent with the role of lower-stratospheric circulation anomalies in modulating the surface response to SSWs (e.g., Afargan-Gerstman et al. 2022). During this period of stratosphere–troposphere coupling, anomalously high surface temperatures were present around the Labrador Sea and Baffin Bay, with marginally below-normal temperatures across northwest Europe and northern Eurasia. This pattern of temperature anomalies is consistent with the average surface response to SSWs, albeit weaker and more transient. Unusually low temperatures also occurred after the SSW in western North America; however, this is more likely related to North Pacific ridging arising from the then-ongoing La Niña conditions, rather than the SSW itself. The lack of prolonged downward coupling, combined with onset of spring, meant that surface impacts from the February 2023 SSW were relatively minimal.

TRANSPORT OF WATER VAPOR FROM 2022 HUNGA-TONGA HA'APAI ERUPTION

The January 2022 eruption of the underwater Hunga Tonga–Hunga Ha'apai (HTHH) volcano increased the mass of water vapor in the stratosphere by about 10% (e.g., Millán et al. 2022). Water vapor injected in the southern tropics spread across the globe, with high anomalies extending above 60-km altitude in the tropics and midlatitudes and concentrated in the middle stratosphere (around 25 km–35 km) in the polar regions (see section 2g7 for details). The influence on radiative forcing of surface climate from the HTHH stratospheric water vapor increase is uncertain (including whether it produced net heating or cooling), but the impact is minor compared to that of climate change (e.g., Schoeberl et al. 2023).

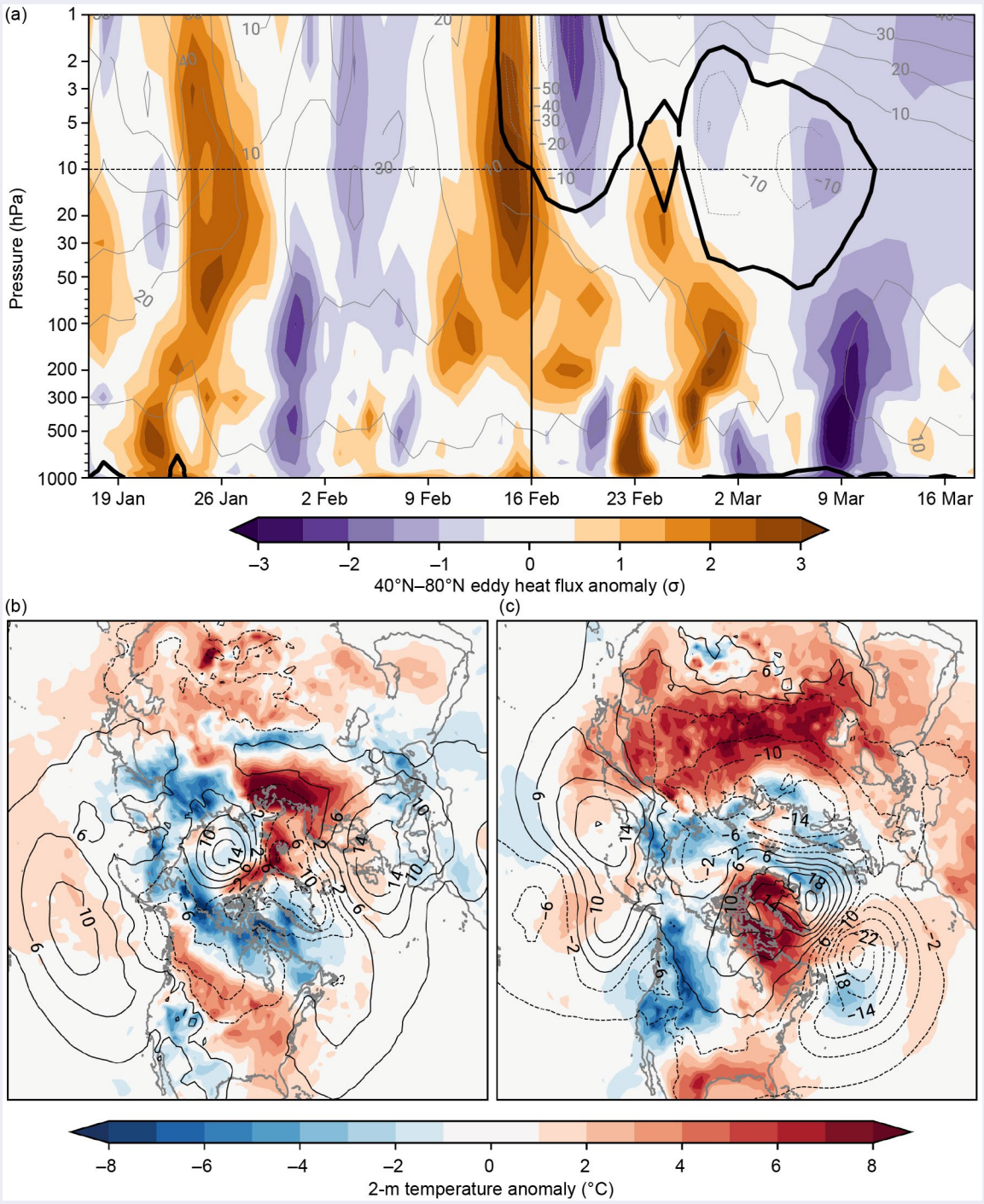

Fig. SB5.1. (a) Vertical profile of daily 40°N–80°N eddy heat flux anomalies (std. dev.; shading) and 60°N zonal-mean zonal winds (m s^{-1}; gray contours, with the zero-wind line in black) for 30 days before to 30 days after the 16 February 2023 sudden stratospheric warming (SSW). (b) Average 2-m temperature anomalies (°C, shading) and mean sea-level pressure anomalies (hPa, contours) for the 15 days prior to the SSW (1–15 February) and (c) during a period of stratosphere–troposphere coupling following the SSW (1–15 March). Data are from the ERA5 reanalysis (Hersbach et al. 2023a,b) and all anomalies are shown with respect to a 30-day centered smoothed 1991–2020 climatology.

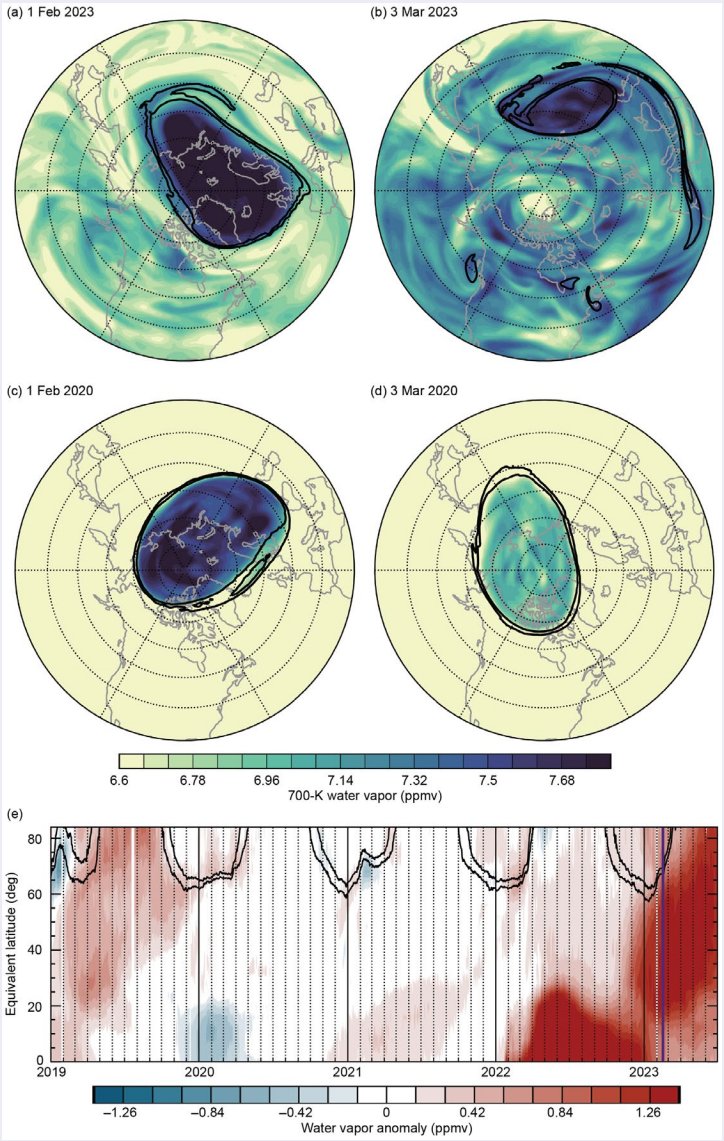

High water vapor concentrations from the HTHH eruption reached the Arctic stratospheric polar vortex edge in early January 2023. By that time, the vortex was well-developed, and the excess water vapor was largely blocked from crossing its edge (Fig. SB5.2e). Water vapor concentrations are typically high inside the vortex and low outside the vortex (Figs. SB5.2c,d show 2020, a year with a strong vortex). Prior to the SSW (Fig. SB5.2a), exceptionally high water vapor concentrations outside the vortex were well separated across the vortex edge from even higher water vapor concentrations inside (but the high water vapor concentrations inside the vortex were not as anomalous; Fig. SB5.2e).

The vortex rapidly broke down in the mid-stratosphere after the SSW, allowing mixing of the record-high midlatitude water vapor concentrations with the high concentrations inside the vortex by early March (Fig. SB5.2b). Compared to other winters with SSWs, the water vapor anomalies following the HTHH eruption resulted in increased water vapor near the polar vortex, whereas SSWs typically result in water vapor reductions near the vortex (e.g., low anomalies in Fig. SB5.2e in January/February 2019 and February 2021). Changes in radiative heating from these different water vapor distributions can affect polar vortex dynamics as well as heating or cooling at lower altitudes.

Fig. SB5.2. (a)–(d) Maps of water vapor concentration (mixing ratio in parts per million by volume [ppmv]) in the Northern Hemisphere mid-stratosphere near 27-km altitude (approx. 18 hPa) on the same two days of year in (a),(b) 2023 and (c),(d) 2020, from a gridded product based on Aura Microwave Limb Sounder (MLS) data (Global Modeling and Assimilation Office 2022; Wargan et al. 2023). (e) Time series of anomalies (departure from the daily mean for 2005–21) of MLS water vapor at the same altitude as the maps (Lambert et al. 2021). The purple vertical line is the initial date of the sudden stratospheric warming. In all panels, the black overlaid lines demarcate the stratospheric polar vortex edge, based on MERRA2 reanalysis (Global Modeling and Assimilation Office 2015).

c. Surface air temperature

—T. J. Ballinger, S. Bigalke, B. Brettschneider, R. L. Thoman, M. C. Serreze, A. H. Butler, U. S. Bhatt, E. Hanna, I. Hanssen-Bauer, S.-J. Kim, J. E. Overland, J. E. Walsh, and M. Wang

1. BRIEF SUMMARY OF IMPACTS AND OVERVIEW

Near-surface (i.e., two-meter) air and upper-ocean temperatures (section 5e) are increasing in today's Arctic. The air temperature warming rate in the Arctic continues to exceed the global mean rate, a phenomenon known as Arctic Amplification (e.g., Serreze and Barry 2011). Warming is leading to changes in the northern high-latitude hydrologic cycle, including increased seasonal precipitation (section 5d), as well as declines in terrestrial snow cover, Greenland Ice Sheet and glacier mass, permafrost stability, and sea-ice extent and thickness (Box et al. 2021; sections 5f, 5g, 5h, 5i). Rising Arctic air temperatures are aligned with more frequent temperature extremes that impact life and property within and beyond the Arctic (Moon et al. 2019; Walsh et al. 2020). Record Arctic warmth in summer 2023 was punctuated by widespread, high temperatures in the Northwest Territories, Canada. These high temperatures contributed to the region's amplified wildfire activity that devastated local communities and ecosystems and contributed to poor down-wind air quality that engulfed much of eastern North America (see Sidebar 7.1 for details). In this section, we provide historical context to 2023 Arctic (60°N–90°N) air temperatures followed by a seasonal overview of notable 2023 air temperature patterns.

2. ANNUAL PERSPECTIVES

Figure 5.5 shows the annual (January–December mean), long-term Arctic and global (90°S–90°N) surface air temperature anomalies from NASA's GISTEMP version 4 data product. The 2023 Arctic annual anomaly just exceeded +1°C and ranked as the fourth-warmest year since 1900. Moreover, all seasons in the Arctic during 2023 experienced >90th percentile warmth, highlighted by the warmest summer and second-warmest autumn since the onset of the twentieth century. While 2023 has emerged as the warmest year on record globally, Arctic temperature anomalies were comparatively higher. This Arctic Amplification signal remains persistent as 2023 marks the 14th consecutive year, and 18th out of the last 20, where the Arctic-averaged temperature exceeded the 1991–2020 mean. The six warmest years in the Arctic have all occurred since 2016, while the 16 warmest years have taken place from 2005 onward.

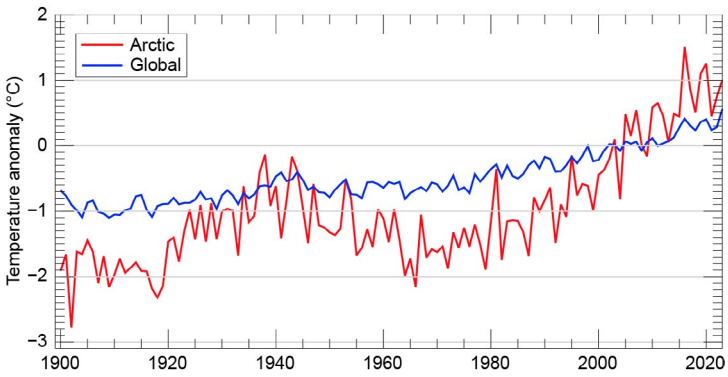

Fig. 5.5. Arctic (60°N–90°N, red) and global (90°S–90°N, blue) surface air temperature anomalies (°C) averaged across land and ocean areas. Temperature anomalies are shown relative to their 1991–2020 means. (Source: NASA GISTEMP v4 data are obtained from the NASA Goddard Institute for Space Studies.)

Complex and often interrelated processes and feedbacks underlie amplified Arctic warming. Less extensive and thinner sea ice (section 5f) tends to melt out earlier in the year. Longer open-water duration results in prolonged transfer of atmospheric energy into the Arctic Ocean. As a result, upper-ocean cooling and sea-ice production are delayed while accumulated upper-ocean heat is released back to the overlying atmosphere, warming the surface air temperatures in autumn and early winter. This process is a key contributor to Arctic Amplification (Serreze and Barry 2011). Marginal sea environments are rapidly changing, most notably in the Chukchi and Beaufort Seas (Ballinger et al. 2023) and Barents Sea (Isaksen et al. 2022a) and are also influencing overlying air temperatures. These and other examples are further touched upon in a seasonal context within the following section.

3. SEASONAL PATTERNS

Figure 5.6 shows seasonal surface air temperature anomalies for 2023, with seasons defined as: winter (January–March), spring (April–June), summer (July–September), and autumn (October–December).

The highest positive temperature anomalies in winter 2023 were observed over parts of the Barents Sea and northwestern Eurasia (~+5°C; Fig. 5.6a). Other notable positive anomalies were found over the Lincoln Sea and just north of the Canadian Arctic Archipelago and Greenland. This contrasts with much of central and eastern Siberia, Hudson Bay, the southern Canadian Arctic Archipelago, and the Greenland Sea, where negative anomalies prevailed. Negative sea-level pressure (SLP) anomalies across much of the Arctic landscape and over the Barents Sea (Fig. 5.7a) suggest that an active high-latitude winter storm track supported the observed mild temperatures, broadly consistent with above-average winter precipitation over the Arctic as a whole (section 5d).

Spring 2023 exhibited notable warmth over the Northwest Territories and Nunavut (~+5°C anomalies; Fig. 5.6b) associated with reduced snow cover and a shorter snow-cover duration (section 5i). The area stretching from the Labrador Sea southeast of Greenland to the Barents Sea was also characterized by above-average temperatures. In contrast, below-average air temperatures (~–2°C to –3°C) were found across Alaska, the northern Bering Sea, the southern Chukchi Sea, and Chukotka. Arctic Ocean air temperatures appeared near or slightly below average, associated with a negative SLP anomaly across the central Arctic Ocean (Fig. 5.7b).

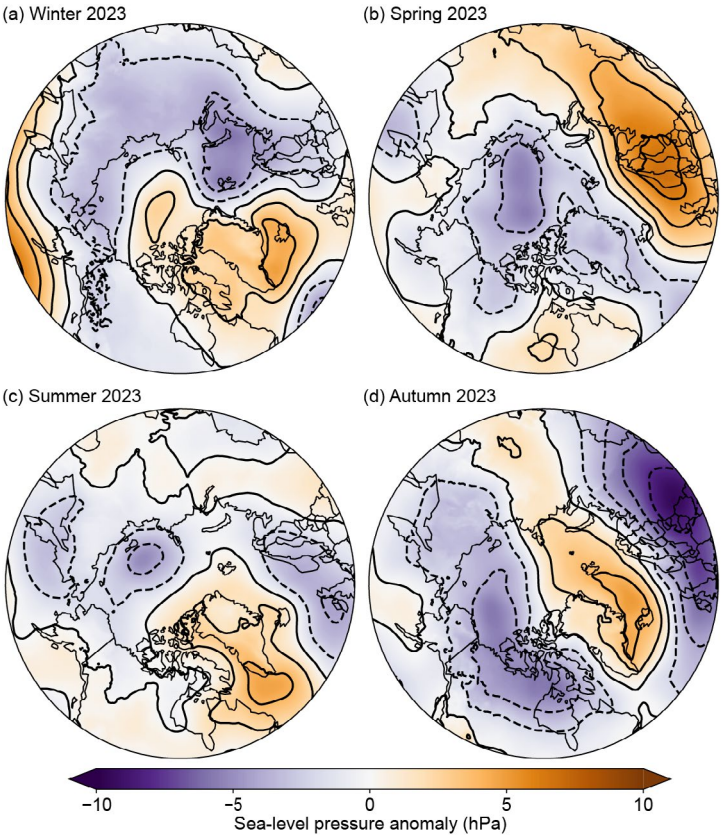

Fig. 5.7. Seasonal sea-level pressure (SLP) anomalies (hPa) during 2023 for (a) winter, (b) spring, (c) summer, and (d) autumn. SLP anomalies are shown relative to their 1991–2020 means. (Source: ERA5 reanalysis SLP data are obtained from the Copernicus Climate Change Service.)

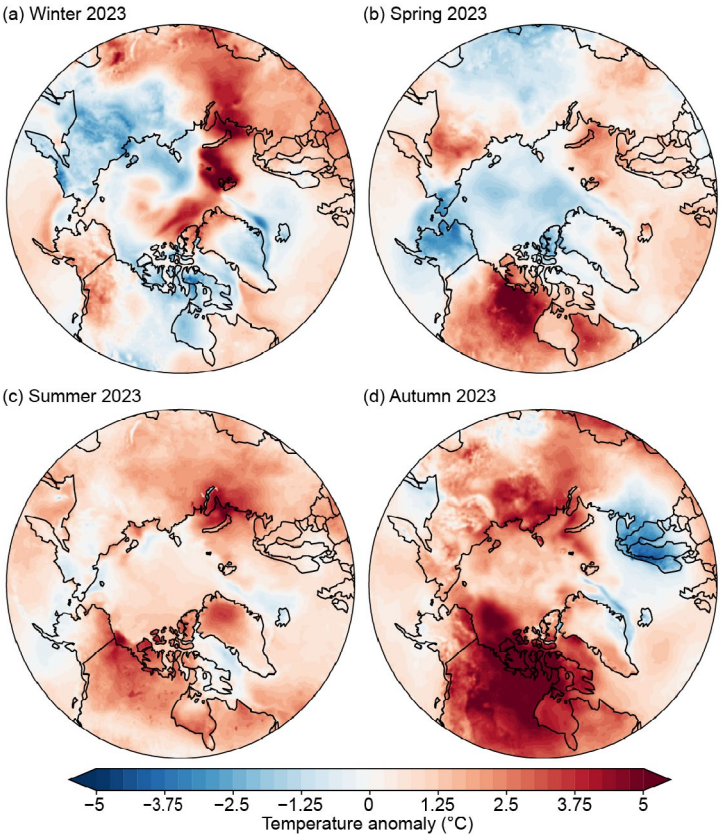

Fig. 5.6. Seasonal surface air temperature anomalies (°C) during 2023 for (a) winter, (b) spring, (c) summer, and (d) autumn. Temperature anomalies are shown relative to their 1991–2020 means. (Source: ERA5 reanalysis air temperature data are obtained from the Copernicus Climate Change Service.)

Summer 2023 was the warmest on record since at least 1900. This record-warm summer was characterized by anomalously high air temperatures over most of northern Canada and the southern reaches of the Barents and Kara Seas (Fig. 5.6c). The anomalous warmth in the Northwest Territories, Nunavut, and the Canadian Arctic Archipelago coincided with dry conditions over these areas (section 5d), supporting extreme wildfire activity (see Sidebar 5.2 for summer 2023 weather and climate impacts and Sidebar 7.1). Positive anomalies over Greenland were associated with an anomalously high number of surface melt days and extent (section 5g).

Above-normal air temperatures were also associated with negative SLP anomaly patterns over much of northern Europe, the Laptev Sea, the western Bering Sea, Kamchatka, and the Sea of Okhotsk (Fig. 5.7c).

Autumn 2023 exhibited a large magnitude and extensive pattern of unusual warmth (Fig. 5.6d), reflecting the second-warmest autumn in the available record. Surface air temperatures approaching 5°C above the 1991–2020 mean characterized most of Arctic Canada to the west and north of Hudson Bay. The Beaufort Sea and adjacent North Slope of Alaska and northwest Siberian lands extending south of the Kara Sea and Laptev Sea coastlines were also much warmer than normal. Meanwhile, isolated cold anomalies appeared confined to Scandinavia. The Canadian Arctic, northern Alaska, and Beaufort Sea warm anomalies were associated with lower-than-normal SLP (Fig. 5.7d). Such below-normal air pressure extended through the troposphere (section 5b), suggesting that a more active storm track may be responsible for sustaining the warm pattern.

Sidebar 5.2: **Summer 2023 weather and climate impacts**

R. L. THOMAN, M. BRUBAKER, M. HEATTA, AND J. JEURING

Summer 2023 (July–September) in the Arctic (land and sea poleward of 60°N) was the warmest on record, with nearly 90% of the Arctic having an average temperature above the 1991–2020 mean (based on ERA5 reanalysis data; section 5c). This sidebar summarizes some representative examples of societal and environmental impacts during the record warm 2023 Arctic summer (see Fig. SB5.3) that are consistent with expectations of environmental extremes in a rapidly warming Arctic. Some of these impacts were directly related to the record-high temperatures.

Wildfires in Arctic Canada burned the most area since comprehensive records began in 1980 (Thoman et. al. 2023; see Sidebar 7.1 for details). At some time during the summer, more than two-thirds of the Northwest Territories' 46,000 residents were displaced from their homes, in many cases for weeks at a time, with significant economic impacts from lost income, disrupted traditional activities, and infrastructure lost to the fires (Thompson 2023). The community of Enterprise, Northwest Territory, was largely destroyed by a fast-moving fire during 13–14 August 2023 (CBC News 2023). Smoke from these wildfires, and wildfires farther south, contributed to haze and reduced air quality from Alaska to Iceland. Poor air quality was also reported during August in portions of Siberia from wildfires in the region (Reuters 2023).

Drought conditions in August and September were observed over much of the Canadian Northwest Territories, including extreme drought in the area near and south of Great Slave Lake. Moderate to severe drought also covered parts of the Yukon Territory but did not extend westward into Alaska (North American Drought Monitor 2024). This dryness was a contributor to both the record coverage of wildfires in the region and the longevity of the fire season, with some fires

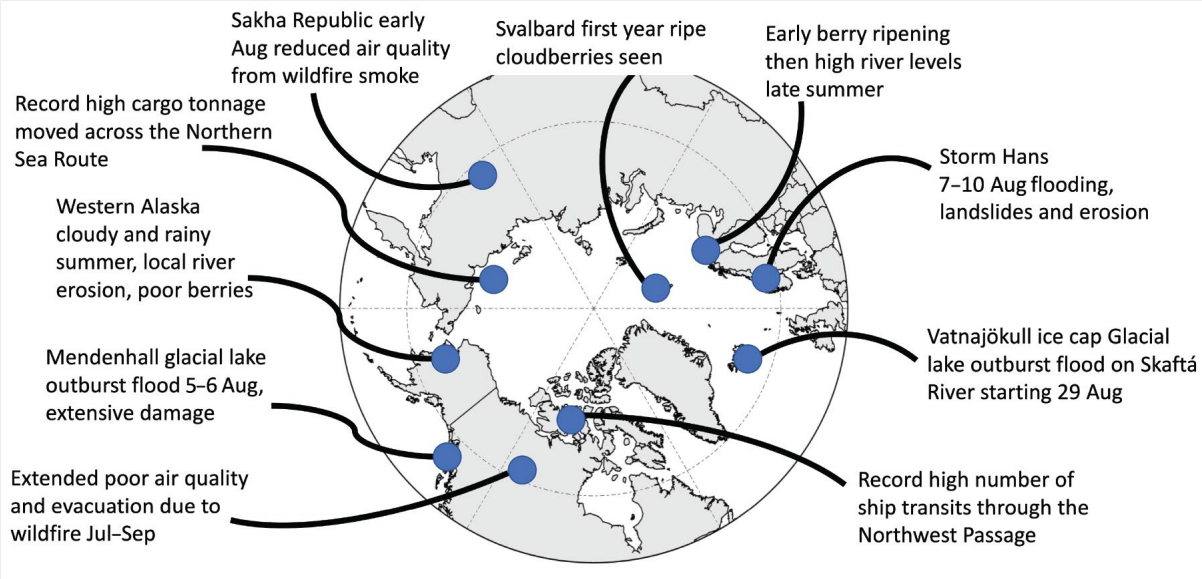

Fig. SB5.3. Impact headlines from around the Arctic during the record-warm 2023 Arctic summer.

actively burning into September, long past the typical end of the Arctic wildfire season (see Sidebar 7.1).

Two significant glacier outburst floods occurred in summer 2023. In Iceland, the Skaftá River (east of Reykjavik) flooded in late August. Flooding on this river occurs every year or two due to geothermal heating under the Vatnajökull ice cap. The 2023 flood was typical for most recent years and did not impact major roadways (Icelandic Met Office 2023). In dramatic contrast, flooding from a catastrophic glacial lake outburst flood occurred on the Mendenhall River near Juneau, Alaska, during 5–6 August. Glacial dam outbursts did not occur here prior to 2011, but thinning of side branches of the Mendenhall Glacier has resulted in annual releases of lake water since then. The 2023 outburst flood event was by far the most destructive on record for the Mendenhall Glacier due to unprecedented high-water levels and extreme erosion rates, which in some places exceeded 50 meters of riverbank lost within 36 hours. At least one home was swept into the river due to this erosion, and many homes and businesses suffered severe flooding, including structures that had no previous history of flooding (Juneau Empire 2023).

In the Nordic Arctic, Sámi observers reported a mild and dry early summer with low river levels and early berry ripening, followed by wet conditions later in the summer, which in some cases caused problems for reindeer herds due to high river levels. An early arrival of spring led to increased snow melt in the mountains and deprived reindeer of their refuge amongst the snow patches in higher elevations, where they typically seek relief from heat and insects (Skarin et al. 2004). The early summer's dryness and heat delayed the green-up process at a time when nutritious vegetation is crucial to provide for the high energy demand of small reindeer calves and lactating females. Overall, a poorer physical condition of reindeer due to insufficient access to food diminishes their preparedness for the coming winter season (Arctic Climate Forum 2023). Much farther north, at the Svalbard Airport (78.2°N), the mean July temperature exceeded 10°C for the first time on record (Sciencenorway 2024). Also for the first time, ripe cloudberries (sp. *Rubus chamaemorus*), usually a lower-latitude fruit, were seen in the Svalbard archipelago (Barents Observer 2023).

Portions of southern Norway and Sweden had extreme rainfall as Storm Hans passed through the region during 7–10 August (section 5d), producing severe flooding, erosion, and landslides. An estimated 4000 people were evacuated across parts of southern Norway as a result of the flooding, including 2000 residents from Hønefoss when the Storelva River flooded the town center. A railway bridge in Ringebu collapsed into the Lagen River on 14 August, and the Braskereidfoss hydro-electric power plant on the Glama River partially collapsed on 9 August. Many major roads were closed and rail services were disrupted during the days following the storm. In Hudiksvall, Sweden, on 7 August, a train partially derailed after heavy rains eroded an embankment, requiring clean-up and repairs into September (Guardian 2023; DW 2023).

With a record-warm summer, both the Northern Sea Route and Northwest Passage became accessible to non-ice-hardened marine traffic. The Northern Sea Route, connecting the European Arctic to the Pacific Ocean via the north coast of Russia and Bering Strait, saw 75 ship transits in the 2023 open season. This is the second-highest number of ships, but the 2.1 million tons of transported cargo (including crude oil) was the highest on record (High North News 2023). The Northwest Passage, connecting the Atlantic to the Pacific via northern Canada and Alaska waters, saw a record number of ship passages. A total of 42 ships made the complete Northwest Passage transit, including 13 cargo ships. The previous high was 33 ships in 2017 (McCague 2023).

Portions of western Alaska were among the few Arctic areas that were not warmer than normal in summer 2023, due in part to unusually persistent cloudy and rainy weather. At Nome, Alaska, measurable rain (≥0.3mm) fell on 62 days during summer, the highest number of days in more than 110 years of observation. This rain exacerbated Noatak River bank erosion near Noatak, Alaska, which has now accelerated for several years due to permafrost thaw and high-water events (LEO Network 2023).

d. Precipitation

—M. C. Serreze, S. Bigalke, R. Lader, T. J. Ballinger, and J. E. Walsh

1. INTRODUCTION

Climate models project increased Arctic precipitation and more frequent heavy precipitation events as the climate warms (see Walsh et al. [2023] and references therein). The latter includes more rain-on-snow events, which will in turn lead to icy crusts that inhibit foraging by semi-domesticated reindeer, caribou, and musk oxen, sometimes leading to mass starvation events (Serreze et al. 2021). However, obtaining accurate measurements of Arctic precipitation is challenging. The precipitation gauge network is sparse (Serreze et al. 2003) and limited to land areas (Barrett et al. 2020). Gauges also suffer from undercatch of solid precipitation (Ye et al. 2021), and correction techniques have large uncertainties (Behrangi et al. 2019). Studies of Arctic precipitation have hence increasingly relied on output from atmospheric reanalyses based on the European Center for Medium Range Weather Forecasts' ERA-Interim and ERA5 products. ERA5 performs slightly better than other atmospheric reanalyses at matching observed precipitation (Barrett et al. 2020; Loeb et al. 2022) and is used here to provide an overview of 2023 Arctic precipitation anomalies. In this section, the Arctic is taken as the region poleward of 60°N and winter, spring, summer, and autumn are defined as January–March, April–June, July–September, and October–December, respectively.

Studies report that Arctic precipitation trends over the past several decades vary regionally (Walsh et al. 2020; White et al. 2021; Yu and Zhong 2021). However, as discussed in the *State of the Climate in 2022* report (Walsh et al. 2023), pan-Arctic precipitation now has a detectable upward trend based on ERA5 (land and ocean measurements; Hersbach et al. 2020) and the gauged-based GPCC V.2022 dataset (land-only measurements; Becher et al. 2013; Schneider et al. 2022) back to 1950.

2. 2023 SUMMARY

Pan-Arctic precipitation for 2023 was about 102% of the 1991–2020 average based on ERA5. Corresponding percentages for winter, spring, summer, and autumn are 107%, 95%, 100%, and 105%. Computed trends remain essentially unchanged since the *State of the Climate in 2022* report (Walsh et al. 2023), which showed that the pan-Arctic trends are positive and statistically significant in all seasons. Short-duration (several days) heavy precipitation broke existing records at various locations within the Arctic.

3. REGIONAL ANOMALIES

Regional anomalies with respect to 1991–2020 means are compared in Fig. 5.8. Winter anomalies were generally small. Modest positive departures characterized the Bering Sea, the panhandle of Alaska, the Barents Sea, and part of northern Europe. Spring was characterized by dry conditions over northern Canada, extending across much of the northern North Atlantic and across western Eurasia. The dry conditions over western Eurasia are consistent with above-average sea-level pressure (as much as +10 hPa) over the region (section 5c,

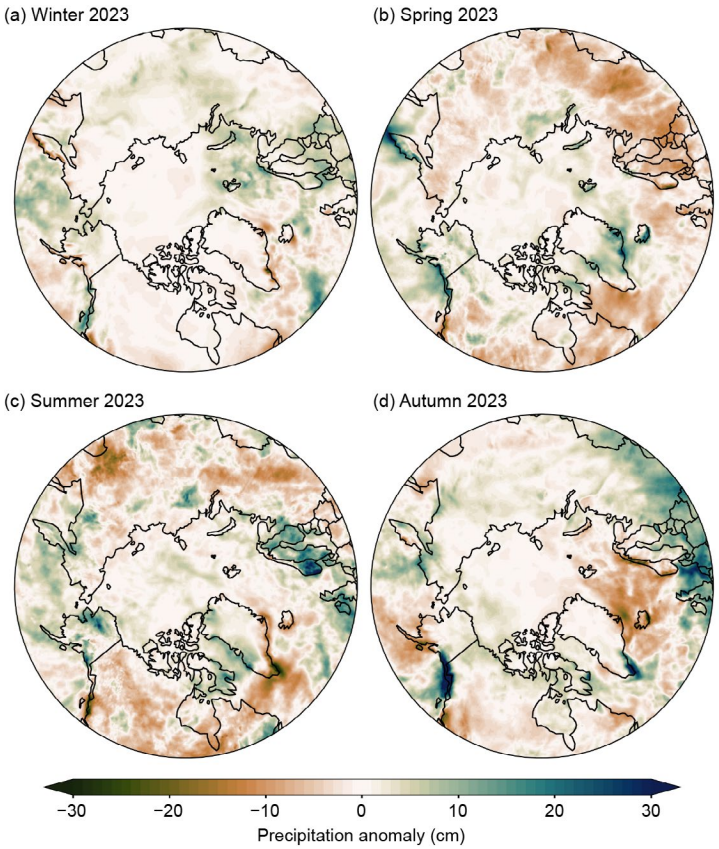

Fig. 5.8. Seasonal departures of Arctic precipitation in 2023 from the 1991–2020 climatological means for (a) winter, (b) spring, (c) summer, and (d) autumn. Green shades denote above-normal precipitation, brown shades denote below-normal precipitation. (Source: ERA5.)

see Fig. 5.7b). Above-average temperatures contributed to the dryness in regions of Canada (section 5c, see Fig. 5.6b). While spring had below-average precipitation for the Arctic as a whole, the season was modestly wet along the Pacific coast of Alaska, part of Greenland, and Kamchatka.

Summer remained notably dry over northern Canada, as well as over parts of Eurasia, contrasting with wet conditions and flood-producing rains over Scandinavia in August. Summer precipitation was also above average over much of Alaska. Portions of the Northwest Territories, Canada, experienced extreme drought during August and September (NOAA North American Drought Monitor), contributing to wildfires that continued through late summer in the Northwest Territories (see Sidebar 7.1 for details). Parts of the Greenland Ice Sheet saw high precipitation (snow) in June (section 5g), but this is not readily seen in the ERA5 data.

Autumn was extremely wet in southeastern Alaska. The airport at Anchorage, Alaska, had the wettest October–December in its 71-year history, breaking the record set just a year earlier in autumn 2022. Autumn also featured positive precipitation anomalies from the United Kingdom to southern Norway, consistent with the belt of negative sea-level pressure anomalies from the United Kingdom to northern Europe (Fig. 5.10d).

4. HISTORICAL PERSPECTIVE

Time series of Arctic precipitation anomalies using ERA5 and the GPCC follow in Fig. 5.9. There are some substantial differences in anomalies between ERA5 and GPCC for individual years, including the considerably lower 2023 precipitation from GPCC for winter, spring and, to a lesser extent, the annual mean. This is not surprising given that the GPCC product covers land only, while ERA5 covers both ocean and land. However, trends computed from the GPCC and ERA5 are similar. ERA5 depicts increases of about 10% in annual precipitation over 1950–2023, with more substantial increases in winter than in summer. For the more recent period 1979–2023, when ERA5 satellite data assimilation increased, trends in ERA5 (and also GPCC) precipitation are larger and remain statistically significant ($p < 0.05$) for the full year and for all seasons except spring. Spring trends for 1979–2023 are weaker than for 1950–2023 and insignificant in both datasets. Increased precipitation is especially pronounced in the subpolar Pacific south of Alaska during autumn, winter, and summer and in the subpolar North Atlantic during winter. The southwestern coast of Norway is dominated by increases in all seasons. Negative trends are most prominent in the subarctic during spring and summer.

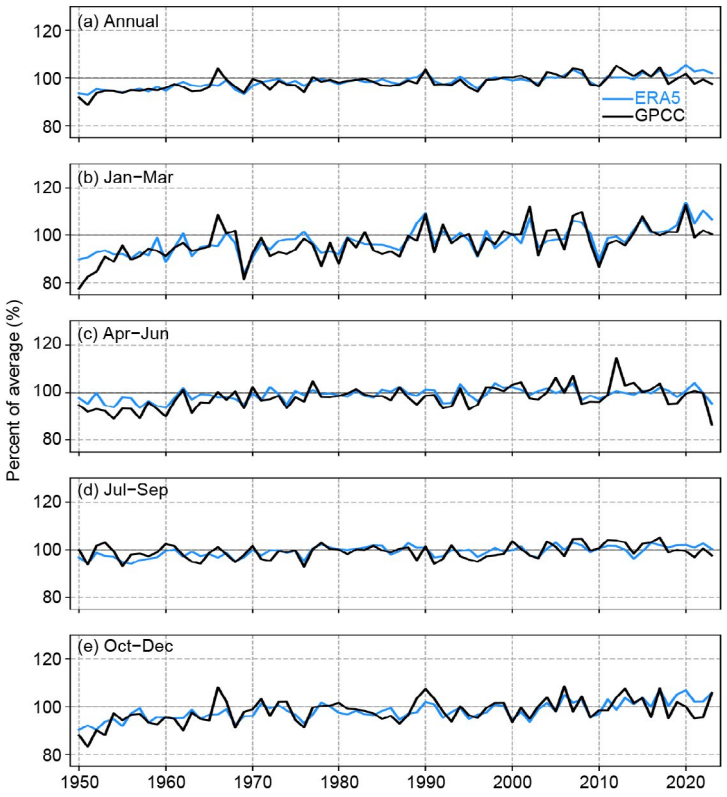

Fig. 5.9. Time series of Arctic precipitation (poleward of 60°N) from 1950 through 2023 expressed as a percentage of the 1991–2020 average (the average, which is 100%, is shown by the horizontal black lines). The 1950–2020 data are from the GPCC Full Data Monthly Version 2022, January 2021–November 2023 data are from the GPCC Monitoring Product Version 2022, and the December 2023 data are from the GPCC First Guess Monthly dataset.

5. HEAVY PRECIPITATION EVENTS

Figure 5.10 shows ranks (relative to the 1950–2023 historical period) of the maximum five-day precipitation events in each season of 2023. During all seasons, heavy precipitation events were scattered across the Arctic, with no clear spatial pattern. Several spatially elongated features are apparent, such as the ones extending poleward along the dateline in

winter and north of the Svalbard Archipelago in summer. Southeastern Greenland also experienced heavy precipitation in spring. There were very few heavy precipitation events in Canada in summer, consistent with drought conditions that contributed to the record wildfire year.

Locally, based on ground station data, northern Europe experienced heavy rains in early August, though this is not readily apparent in Fig. 5.10, likely due to the challenge of comparing station (point) measurements to ERA5 grid cell values (31-km grid resolution). The heaviest rains in 25 years occurred in southern Norway, causing a dam to break (see Sidebar 5.2). In the North American subarctic, more than 100 mm of rain that fell over a two-day period in late November, which was attributable to an atmospheric river, led to landslides and multiple fatalities in Wrangell, Alaska.

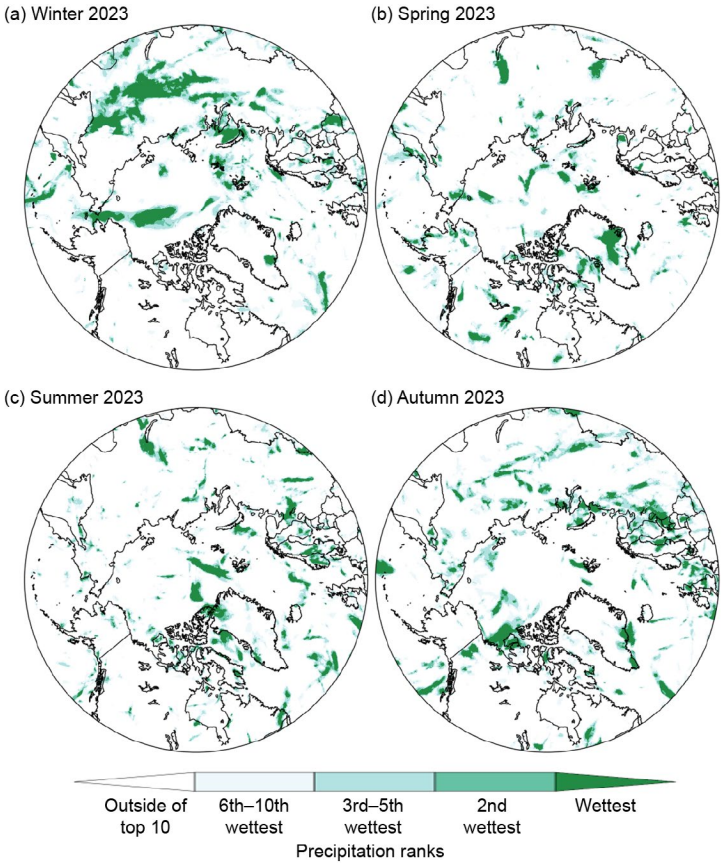

Fig. 5.10. Ranks of maximum five-day precipitation amounts in 2023 for (a) winter, (b) spring, (c) summer, and (d) autumn (based on events from 1950–2023). (Source: ERA5.)

e. Sea-surface temperature

—M.-L. Timmermans and Z. Labe

Arctic Ocean sea-surface temperatures (SSTs) in the summer are driven by the amount of incoming solar radiation absorbed by the sea surface and by the flow of warm waters into the Arctic from the North Atlantic and North Pacific Oceans. Solar warming of the Arctic Ocean surface is influenced by sea-ice distribution (with greater warming occurring in ice-free regions), cloud cover, and upper-ocean stratification. Inflows of relatively warm Arctic river waters can provide an additional heat source in the coastal regions.

Arctic SST is an essential indicator of the strength of the ice–albedo feedback cycle in any given summer sea-ice melt season. As the sea-ice cover decreases, more incoming solar radiation is absorbed by the darker ocean surface and, in turn, the warmer ocean melts more sea ice. Marine ecosystems are also influenced by SSTs, which affect the timing and development of primary production cycles, as well as available habitat. In addition, higher SSTs are associated with delayed autumn freeze-up and increased ocean heat storage throughout the year. An essential point for consideration, however, is that the total heat content contained in the ocean surface layer (i.e., the mixed layer) depends on mixed-layer depth; a shallower mixed layer with higher SSTs could contain the same amount of heat as a deeper mixed layer with lower SSTs. We discuss only SSTs here and do not quantify ocean heat content due to a lack of in situ observations.

The monthly mean SST data presented here are from the 0.25° × 0.25° NOAA OISST Version 2.1 product, a blend of in situ and satellite measurements (Reynolds et al. 2002, 2007; Huang et al. 2021; NOAA 2024). In January 2023, OISST Version 2.1 replaced the 1° × 1° NOAA OISST Version 2, which was analyzed in previous annual *State of the Climate* reports; reported trends are statistically indistinguishable between the two versions (for further details, see Timmermans and Labe 2023). The period of analysis is June 1982 to September 2023, with 1991–2020 used as the climatological reference period.

Here, we focus most closely on August 2023 mean SSTs in context with the climatological record. August mean SSTs provide the most appropriate representation of Arctic Ocean summer SSTs because sea-ice extent is near a seasonal low at this time of year, and there is not yet the influence of surface cooling and subsequent sea-ice growth that typically takes place in the latter half of September.

August 2023 mean SSTs were as high as ~11°C in the Barents, Kara, and Beaufort Seas

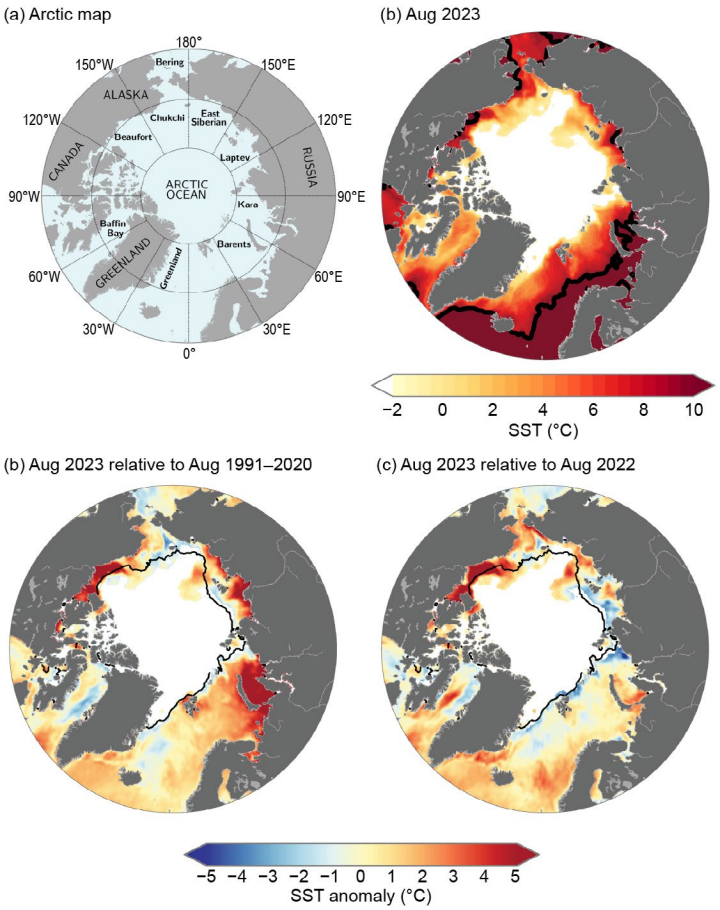

Fig. 5.11. (a) Arctic Ocean map showing marginal sea locations. (b) Mean sea-surface temperature (SST; °C) in Aug 2023. Black contours indicate the 10°C-SST isotherm. (c) SST anomalies (°C) in Aug 2023 relative to the Aug 1991–2020 mean. (d) Difference between Aug 2023 SSTs and Aug 2022 SSTs (negative values indicate where 2023 was cooler). White shading in all panels is the Aug 2023 mean sea-ice extent. Black lines in (c) and (d) indicate the Aug 1991–2020 median ice edge. Sea-ice concentration data are the NOAA National Snow and Ice Data Center's (NSIDC) Climate Data Record of Passive Microwave Sea Ice Concentration, Version 4 (https://nsidc.org/data/g02202) for the 1982–2022 period of record, and Near-Real-Time NOAA/NSIDC Climate Data Record of Passive Microwave Sea Ice Concentration, Version 2 (https://nsidc.org/data/g10016) (Peng et al. 2013; Meier et al. 2021a,b) for Jun–Sep 2023; a threshold of 15% concentration is used to calculate sea-ice extent.

and reached values as high as ~8°C in other Arctic basin marginal regions (e.g., eastern Chukchi Sea and Laptev Sea; Figs. 5.11a,b). August 2023 mean SSTs were anomalously high compared to the 1991–2020 August mean (around 5°C–7°C higher) in the Barents, Kara, Laptev, and Beaufort Seas, and anomalously low in Baffin Bay and parts of the Greenland, Bering, and Chukchi Seas (around 1°C–3°C lower than the 1991–2020 mean; Fig. 5.11c). These regional variations differ significantly from year to year. For example, there were considerably higher SSTs in the Beaufort Sea in August 2023 compared to August 2022, with differences of up to 7°C, and mostly lower 2023 SSTs in the Laptev Sea (Fig. 5.11d).

Warm river inflows may have influenced marginal sea SSTs with anomalously high August 2023 SSTs in the Beaufort Sea where the Mackenzie River enters, in the Kara Sea in the vicinity of the Ob and Yenisei River inflows, and in the Laptev Sea where the Lena River enters (Fig. 5.11c). This corresponds with anomalously high surface air temperatures in June–August 2023 over northern North America and Siberia that warmed the rivers (section 5c).

The above-normal SSTs in the Beaufort Sea in August 2023, which were also observed in July (Fig. 5.12b), relate to relatively low August 2023 sea-ice concentrations in the region extending from the Beaufort to East Siberian Seas (second only to the record-low August 2012 sea-ice conditions for the area; section 5f). The timing of seasonal sea-ice retreat from the Beaufort Sea, where sea ice was almost entirely absent by July 2023 (Fig. 5.12), also links to high SSTs via the ice–albedo feedback (section 5f). A similar spatial pattern of SST anomalies persisted through the melt season end in September (Fig. 5.12d) although with generally reduced warm anomalies in the marginal seas, signifying cooling in the latter half of the month.

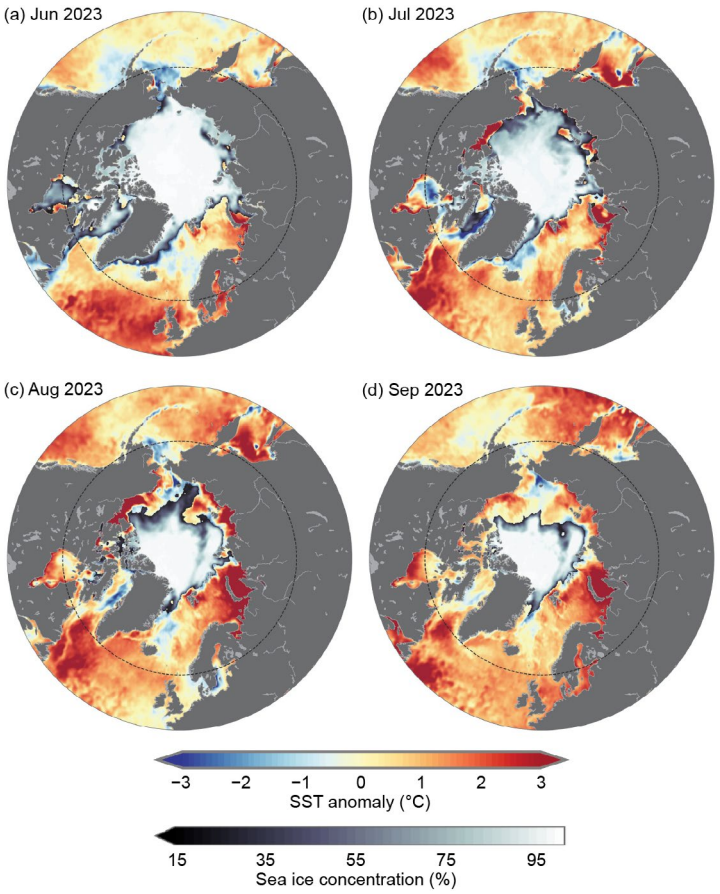

Fig. 5.12. Sea-surface temperature (SST) anomalies (°C) for (a) Jun 2023, (b) Jul 2023, (c) Aug 2023, and (d) Sep 2023 relative to the 1991–2020 mean for the respective months. The mean sea-ice concentration for the corresponding month is also shown. The evolution of sea-ice concentration over the months of Jun to Aug illustrates why it is not appropriate to evaluate long-term SST trends in Jun and Jul over most of the Arctic marginal seas, which still have significant sea-ice cover in those months. While sea-ice extent is lowest in Sep, SSTs cool in the latter part of the month. The dashed circle indicates the latitudinal bound of the Fig. 5.11 and Fig. 5.13 map images. See Fig. 5.11 caption for sea-ice dataset information.

The below-normal August 2023 SSTs in Baffin Bay are consistent with below-normal surface air temperatures in the region in June–August 2023 (section 5c). Early summer sea-ice extent in Baffin Bay was close to the climatological average, with almost full ice cover in June 2023 (Fig. 5.12a), which is further consistent with the anomalously low SSTs (section 5f).

The Arctic Ocean has experienced mean August SST warming trends from 1982 to 2023, with statistically significant (at the 95% confidence interval) linear warming trends in almost all regions (Fig. 5.13a). Mean August SSTs for the Arctic Ocean and marginal seas between 65°N and 80°N exhibit a linear warming trend of 0.05±0.01°C yr^{-1} (Fig. 5.13b; SSTs for 80°N–90°N are omitted since this region is largely perennially ice covered). Even while anomalously low SSTs in

Baffin Bay were prominent in August 2023 (Fig. 5.11c), SSTs show a linear warming trend over 1982–2023 of 0.07±0.02°C yr^{-1} for this region (Fig. 5.13c) although with considerable interannual variability in mean August values.

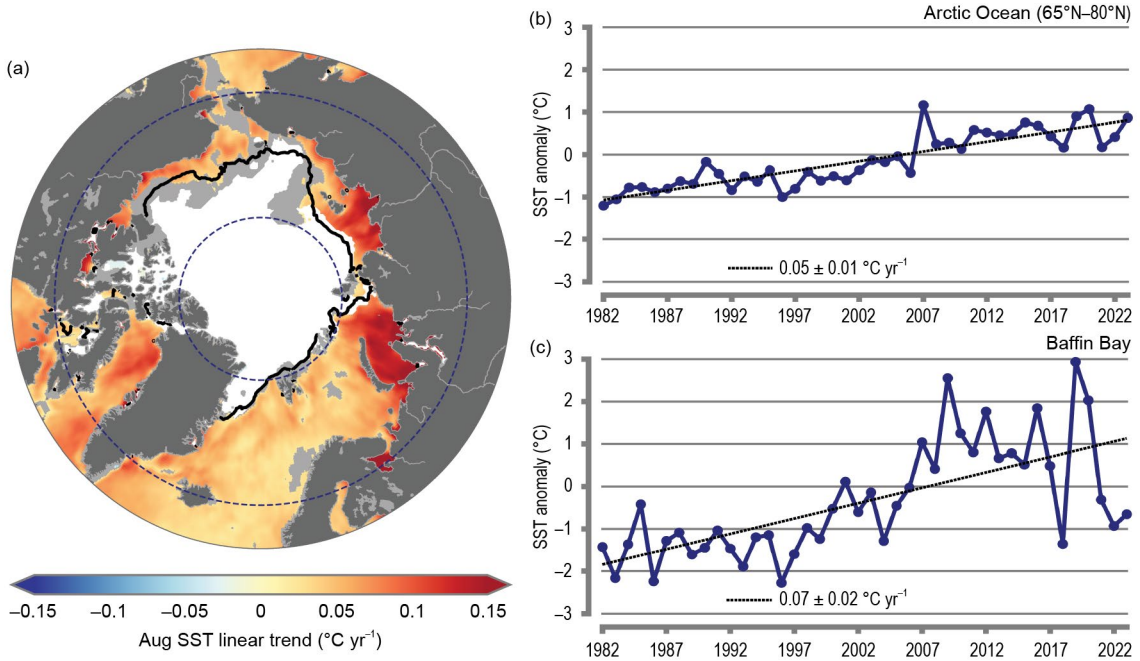

Fig. 5.13. (a) Linear sea-surface temperature (SST) trend (°C yr^{-1}) for Aug of each year from 1982 to 2023. The trend is only shown for values that are statistically significant at the 95% confidence interval; the region is shaded light gray otherwise. White shading is the August 2023 mean sea-ice extent, and the black line indicates the August 1991–2020 median ice edge. (b),(c) Area-averaged SST anomalies (°C) for Aug of each year (1982–2023) relative to the 1991–2020 Aug mean for (b) the Arctic Ocean between 65°N and 80°N (indicated by the dashed blue circles in [a]), and (c) Baffin Bay (see Fig. 5.11a). The dotted lines show the linear regression of the SST anomaly over the period shown with trends in °C yr^{-1} (with 95% confidence intervals) indicated on the plots. See Fig. 5.11 caption for sea-ice dataset information.

f. Sea ice

—W. N. Meier, A. Petty, S. Hendricks, D. Perovich, S. Farrell, M. Webster, D. Divine, S. Gerland, L. Kaleschke, R. Ricker, and X. Tian-Kunze

Sea ice is the frozen interface between the ocean and atmosphere in the Arctic. It limits ocean–atmosphere exchanges of energy and moisture and plays a critical role in Arctic ecosystems and Earth's climate. The presence of sea ice modulates human activities in the Arctic, including Indigenous hunting and transportation, marine navigation, and national security responsibilities. Arctic sea-ice conditions during 2023 continued to illustrate the profound changes underway in the Arctic due to climate change.

1. SEA-ICE EXTENT

Arctic sea-ice extent in winter (January–March) 2023 was lower than in 2022 and overall was the third-lowest winter average in the record that began in 1979. Extent values are from the National Snow and Ice Data Center's Sea Ice Index (Fetterer et al. 2017), one of several extent products (Ivanova et al. 2014; Lavergne et al. 2019) derived from satellite-borne passive microwave sensors operating since 1979. Winter extent was particularly low in the Barents Sea region and slightly lower than the 1991–2020 average in the Sea of Okhotsk and Gulf of St. Lawrence.

By March, the month with the most extensive coverage, the total sea-ice extent of 14.44×10^6 km^2 was 0.59×10^6 km^2 (3.9%) lower than the 1991–2020 average and the sixth-lowest March extent in the 45-year record. The March 2023 extent continued the statistically significant downward trend of –2.6% per decade over the 1979–2023 record (Fig. 5.14a). On a regional basis, March 2023 was characterized by below-average extent across most of the Arctic, with slightly higher-than-average extent in the Greenland Sea (Fig. 5.14b).

After March, the seasonal retreat of sea ice began. The Northern Sea Route along the northern Russian coast was relatively slow to open; sea ice extended southward to the coast in the eastern Kara Sea and the East Siberian Sea through July, but by late August, open water was present throughout the entire route. The Northwest Passage through the Canadian Arctic Archipelago became relatively clear of ice by September. And though ice largely blocked the western end of the northern route through M'Clure Strait throughout the melt season, ice extent in the Passage reached near-record lows (Sidebar 5.2).

September, the month of the annual minimum extent, was characterized by below-average coverage in the Pacific sector with open water extending far northward from the coast in the Beaufort, Chukchi, and Siberian Seas (Fig. 5.14c). The September 2023 sea-ice extent of 4.37×10^6 km^2 was 1.21×10^6 km^2 (21.6%) lower than the 1991–2020 average and the fifth-lowest September extent on record. The September trend from 1979 through 2023 is

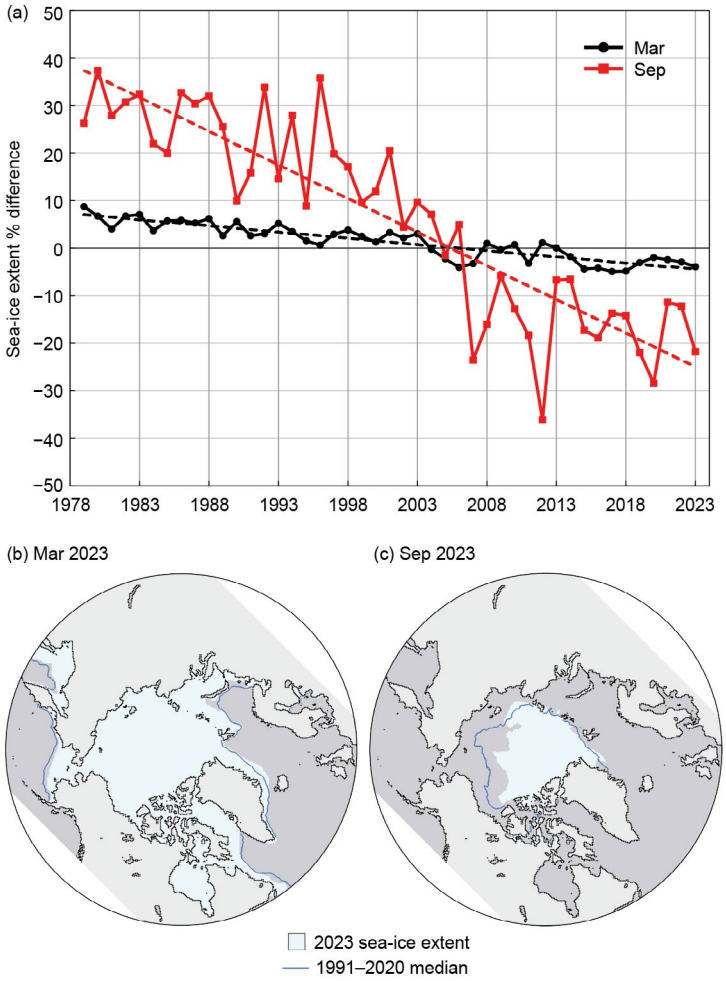

Fig. 5.14. (a) Monthly sea-ice extent anomalies (%, solid lines) and linear trend lines (%, dashed lines) for Mar (black) and Sep (red) from 1979 to 2023. The anomalies are relative to the 1991–2020 average for each month. (b) Mar 2023 and (c) Sep 2023 monthly average sea-ice extent; the 1991–2020 median extent is shown by the blue contour.

–13.9% per decade and like all other monthly trends is statistically significant. The 17 lowest September extents in the satellite record have all occurred in the last 17 years (2007–23).

2. SEA-ICE AGE, THICKNESS, AND VOLUME

Sea-ice age is a rough proxy for thickness as multiyear ice (ice that survives at least one summer melt season) grows thicker over successive winters. Sea-ice age is presented here (Fig. 5.15) for the period 1985–2023 based on Tschudi et al. (2019a,b). One week before the 2023 annual minimum extent, when the age values of the remaining sea ice are incremented by one year, the amount of multiyear ice remaining in the Arctic continued to be far lower than that in the 1990s (Fig. 5.15). Since 2012, the Arctic has been nearly devoid of the oldest ice (>4 years old); this continued in 2023, with an end-of-summer old ice extent of 93,000 km^2. In the 39 years since ice-age records began in 1985, the Arctic has changed from a region dominated by multiyear sea ice to one where seasonal sea ice prevails. A younger ice cover implies a thinner, less voluminous sea-ice pack and one that is more sensitive to atmospheric and oceanic changes.

Sea ice drifts with winds and ocean currents, while growing and melting thermodynamically. Ice divergence creates open water leads and, in freezing conditions, new ice forms, while ice convergence leads to dynamic thickening. Sea-ice thickness provides a record of the cumulative effect of dynamic and thermodynamic processes and thus is an important indicator of overall ice conditions. The ESA CryoSat-2/SMOS satellites have provided a record of seasonal (October–April) ice thickness and volume (Ricker et al. 2017; ESA 2023) since the 2010/11 winter. Since 2018, the NASA ICESat-2 satellite has also provided thickness estimates (Petty et al. 2020; 2023a,b). Some differences between these two products are seen in the monthly average winter Arctic thickness, but both products show monthly thicknesses from autumn 2022 through early spring 2023 (October through April) similar to the mean of this short period of observational overlap (2018 onwards, Fig. 5.16a). April 2023 thickness (Fig. 5.16b) from CryoSat-2/SMOS relative to the 2011–2023 April mean (Fig. 5.16c) shows that the eastern Beaufort Sea and the East Siberian Sea had relatively thinner sea ice than the 2011–22 mean, particularly near the Canadian Archipelago. Thickness was higher than average in much of the Laptev and Kara Seas and along the western and northwestern coasts of Alaska, extending northward toward the pole. The East Greenland Sea had a mixture of thicker- and thinner-than-average ice.

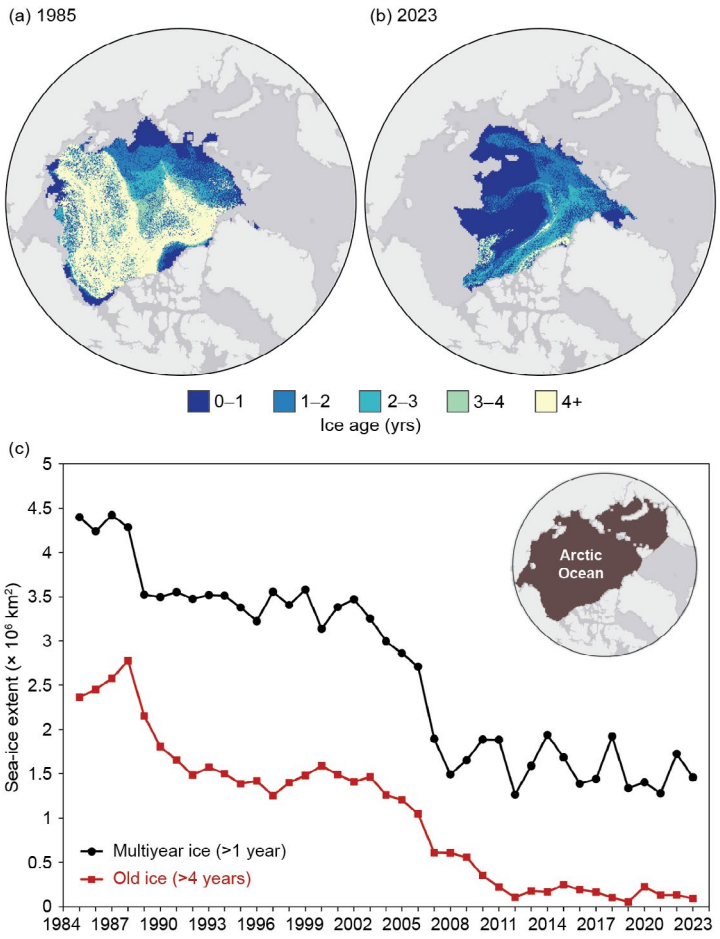

Fig. 5.15. Sea-ice age coverage map for the week before minimum total extent (when age values are incremented to one year older) in (a) 1985 and (b) 2023; (c) extent of multiyear ice (black) and ice >4 years old (red) within the Arctic Ocean (inset) for the week of the minimum total extent (× 10^6 km^2).

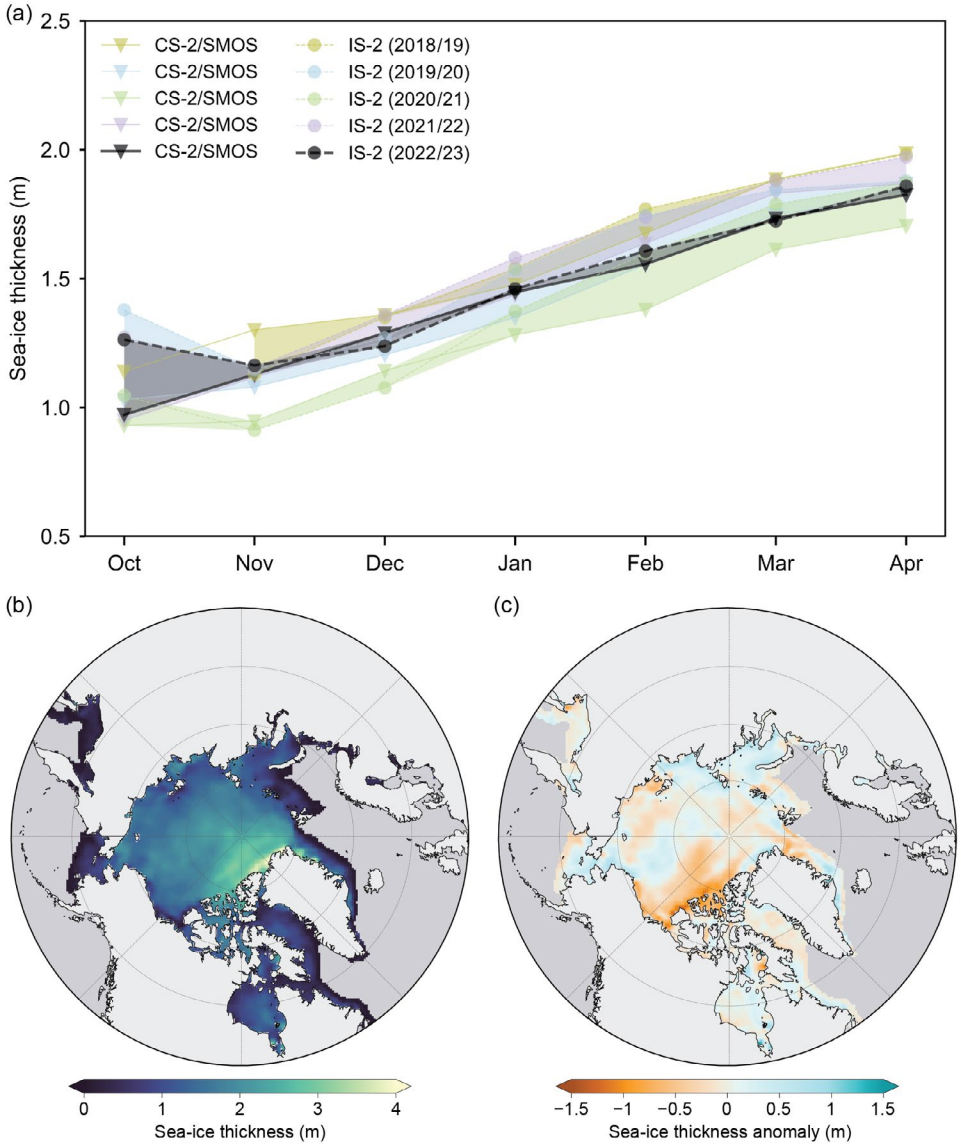

Fig. 5.16. (a) Oct–Apr monthly average sea-ice thickness (m), calculated over an Inner Arctic Ocean Domain, from ICESat-2 (circles) and CryoSat-2/SMOS (triangles) for 2018/19 through 2022/23; (b) average Apr 2023 sea-ice thickness (m) map from CryoSat-2/SMOS; (c) CryoSat-2/SMOS thickness anomaly (m) map for Apr 2023 relative to the 2010–22 average.

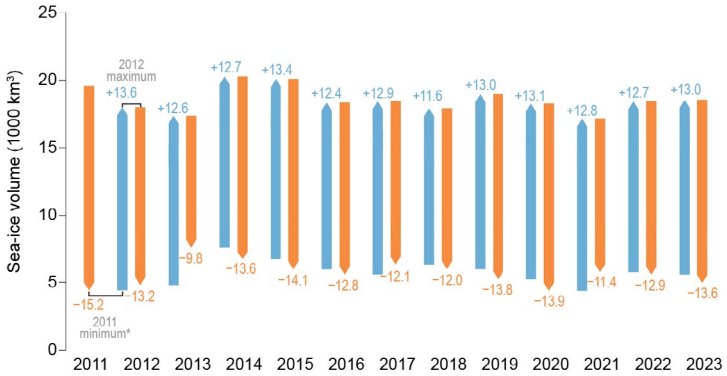

Fig. 5.17. Annual sea-ice volume loss (orange) and gain (blue) between the annual maximum and minimum values from CryoSat-2/SMOS. Units are in 1000 km³. Note: CryoSat-2/SMOS overestimates annual minimum sea-ice volume because Sep data are not available.

Sea-ice thickness from CryoSat-2/SMOS is integrated with ice concentration to provide winter volume estimates for 2010–23. The change from winter maximum volume to summer minimum and back to winter over the years illustrates the strong seasonal cycle and interannual variability (Fig. 5.17). There is little indication of a trend in the relatively short 12-year time series. Volume gain throughout the October 2022 to April 2023 growth season of 12,900 km³ was within the range of earlier years in the record and balanced the volume loss during the summer 2022 melt season, though the subsequent 2023 summer loss was greater.

g. Greenland Ice Sheet

—K. Poinar, K. D. Mankoff, X. Fettweis, B. D. Loomis, R. S. Fausto, B. E. Smith, B. Medley, A. Wehrlé, C. D. Jensen, M. Tedesco, J. E. Box, T. L. Mote, and J. H. Scheller

Mass loss from the Greenland Ice Sheet raises global mean sea level, affects coastal infrastructure, and increases coastal erosion, flooding, saltwater intrusion, and habitat loss. Its mass balance is the difference between accumulated snowfall and melt, sublimation, evaporation, and discharge of solid ice directly into the ocean (iceberg calving). We present three independent estimates of the total mass balance of the Greenland Ice Sheet over the 2023 mass balance year, 1 September 2022 to 31 August 2023: input-output-derived (–170±69 Gt), gravity-derived (–205±76 Gt), and elevation-derived (–183±43 Gt), values that agree within measurement uncertainties and that are close to or slightly more negative than the 1991–2020 mean. Although winter snow accumulation was above average, net mass loss occurred because ice discharge and meltwater runoff exceeded accumulation.

Surface mass balance (SMB), one component of total mass balance, comprises mass input from net snow accumulation and mass loss from meltwater runoff. Surface mass balance is driven by air temperature, snow cover, albedo, and bare-ice area. We summarize in situ and satellite observations of these quantities over the 2023 mass balance year.

Meteorological data collected by land-based weather stations (operated by the Danish Meteorological Institute) and on-ice weather station transects (operated by the Programme for Monitoring of the Greenland Ice Sheet, PROMICE) across Greenland (Fausto et al. 2021) indicate that monthly air temperatures during autumn (September–November 2022) were predominantly higher than the 1991–2020 mean, winter (December–February 2022/23) temperatures were close to or below average, and spring (March–May 2023) temperatures were close to or above average. At Summit Station in the ice sheet interior (3216 m a.s.l.), the autumn mean was record high (–23.0°C, +7.6°C anomaly). Summer (June–August [JJA] 2023) temperatures were below average in west Greenland and predominantly slightly above average in south and east Greenland. At Summit Station, the mean summer temperature was –10.3°C (+3.5°C anomaly). Summer snow accumulation was also the highest since 1940, at 34% above the mean.

Cooler-than-average conditions characterized the beginning of the 2023 melt season. In late June through mid-July, however, a persistent high-pressure system promoted multiple melt events. During a single week in July, record-setting ice ablation (loss) of 40 cm was recorded high on the ice sheet at South Dome (2893 m a.s.l.). Over 21–26 August, another high-pressure system caused warm, dry conditions in the north. On 21 August, the temperature at Summit Station reached –0.6°C, and PROMICE (Programme for Monitoring of the Greenland Ice Sheet) stations

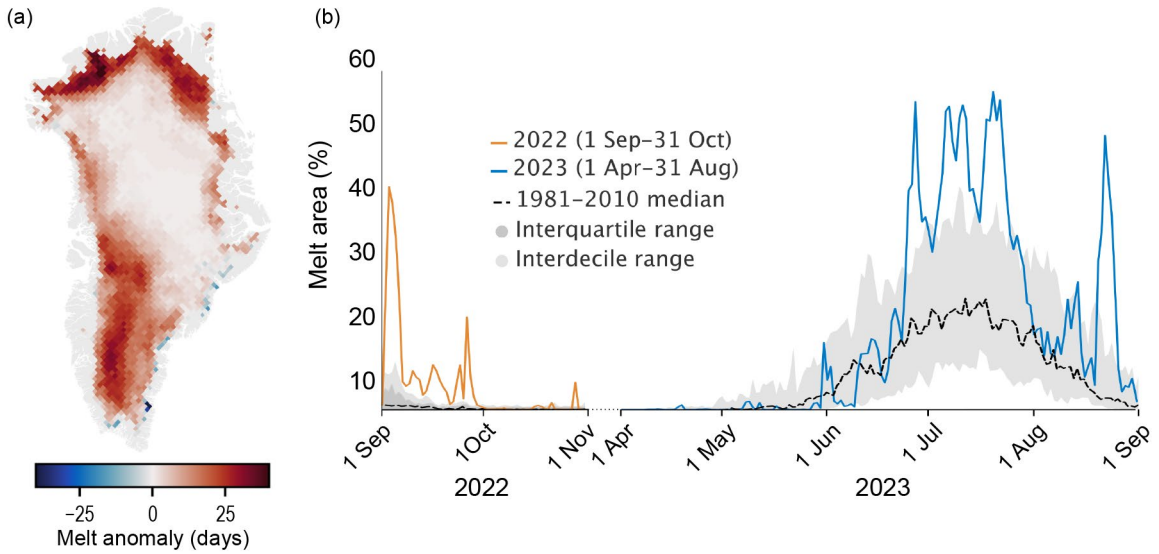

Fig. 5.18. (a) Number of surface melt days from 1 Apr to 31 Aug 2023, expressed as an anomaly with respect to the 1991–2020 period, from the daily Special Sensor Microwave Imager / Sounder (SSMIS) 37-GHz horizontally polarized passive microwave radiometer satellite data (Mote 2007). (b) Surface melt extent as a percentage of ice-sheet area across the 2023 mass balance year, also derived from SSMIS and including autumn 2022 (orange) and spring/summer 2023 (blue) and omitting winter 2022/23.

on the north and east coasts recorded temperatures up to 16°C above seasonal averages. Southern Greenland experienced high rainfall rates during this period. The total number of melt days measured across the ice sheet exceeded the 1991–2020 mean virtually everywhere (Fig. 5.18a). The cumulative melt-day area in 2023 (Fig. 5.18b) was the third-largest on record, 40% greater than the 1991–2020 mean.

The average albedo across Greenland, measured by the Moderate Resolution Imaging Spectroradiometer (MODIS) following Box et al. (2017), was the fifth lowest over the period 2000–23 (Fig. 5.19a), in part because melt onset did not occur until late June. This yielded low bare-ice area measured by Sentinel-3 SICE (Kokhanovsky et al. 2020; Wehrlé et al. 2021) in the early melt season, but by the end of the summer, the bare-ice area was above average (Fig. 5.19b). The late-summer warmth caused a lower- (darker-) than-average melt-season albedo, especially across southwestern and northern Greenland (Fig. 5.19c), although the climatic baseline for this dataset is quite short (2017–22).

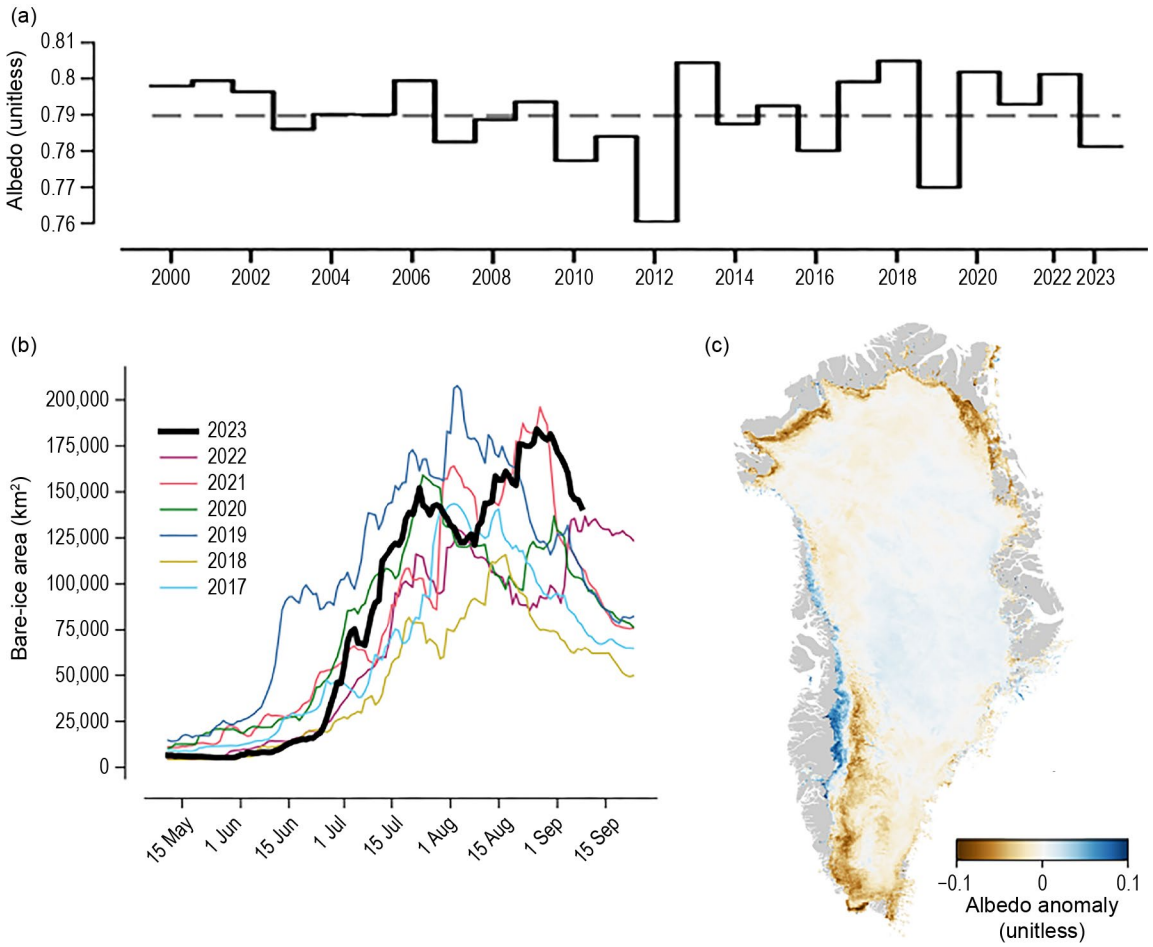

Fig. 5.19. (a) Time series of average summer albedo since 2000, from the Moderate Resolution Imaging Spectroradiometer (MODIS), with dashed line showing mean. (b) Bare-ice area (km²) measured from Sentinel-3 observations (Wehrlé et al. 2021). (c) Albedo anomaly for summer (June–August) 2023 measured from Sentinel-3 data, relative to summers 2017–22 (Wehrlé et al. 2021).

The MARv3.14 model (MAR; Fettweis et al. 2020) forced by ERA5 (Hersbach et al. 2020) provides SMB values at 5-km horizontal resolution. The ice-sheet-wide total SMB over the 2023 mass balance year was 337±51 Gt, 12% below the 1991–2020 mean. Snowfall accumulation in autumn 2022 and summer 2023 were each 34% higher than the 1991–2020 mean and were the highest on record since MAR-based reconstructions began in 1940. Winter and spring snow accumulation were each close to the mean. Total snowfall accumulation was 831 Gt, 14% above the mean and the sixth highest in the 84-year record dating back to 1940. Exceptional rainfall in September 2022 and above-average JJA 2023 rainfall pushed the rainfall total to 94 Gt, the highest on record and more than 4 std. dev. above the mean. Total precipitation (snowfall plus

rainfall) was also the highest on record, but this was compensated by high runoff, 542±81 Gt, 60% above the 1991–2020 mean, and 43 Gt of sublimation and evaporation.

Hundreds of marine-terminating glaciers discharge Greenland ice into the ocean as icebergs; this discharge is the other main way, alongside meltwater runoff, that the ice sheet loses mass. PROMICE combines satellite-derived ice velocity and ice thickness data to produce an ice-sheet-wide glacier discharge time series (Mankoff et al. 2020). For the 2023 mass balance year, this showed that Greenland Ice Sheet glaciers discharged 508±47 Gt. This is 10% above the 1991–2020 mean discharge of 465±43 Gt yr^{-1} but falls below the 1991–2020 increasing discharge trend of +2.4 Gt yr^{-1}.

We difference the SMB ice input from MAR (337±51 Gt) and the discharge ice output from PROMICE (508±47 Gt) to obtain an input-output total mass balance of –170±69 Gt over the 2023 mass balance year (Fig. 5.20). This is within 5% of the 1991–2020 input-output-derived mean of –162±88 Gt yr^{-1}.

The GRACE (2002–17) and GRACE-FO (2018–present) satellite missions measure gravity anomalies to deduce changes in total ice mass (Tapley et al. 2019). These data include ice-sheet ice and surrounding glaciers and ice masses; we therefore scale the results by 0.84 to include the ice sheet only (Colgan et al. 2015; see section 5h for glaciers and ice caps outside of Greenland). This yields –205±76 Gt over the 2023 mass balance year (Fig. 5.20), which is 20% less loss than the 2002–23 yearly mean of –257±9 Gt from GRACE/GRACE-FO.

The ICESat-2 mission measures ice-sheet surface height. Changes in this value reflect ice mass loss as well as changes in firn air content and short-term SMB anomalies. We thus subtract model-based estimates of these quantities from ICESat-2 data produced following the processing strategy outlined in Smith (2023), then recover the total mass change by adding back the modeled SMB anomalies (Fig. 5.20). The mass change over the 2023 mass balance year was –183±43 Gt.

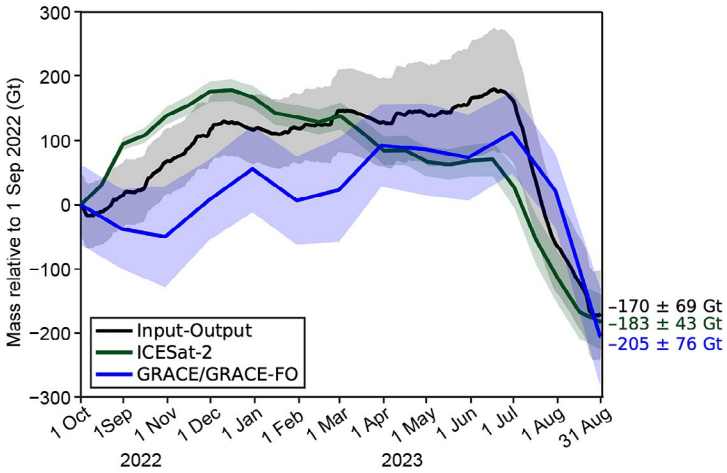

Fig. 5.20. Time series of three independent measurements of ice-sheet mass balance from 1 Sep 2022 through 31 Aug 2023. Results from ICESat-2 (green), the Gravity Recovery and Climate Experiment (GRACE)/GRACE Follow-On (GRACE-FO) (blue), input-output (black), and their associated uncertainties (shaded), each shown at appropriate time resolution (15, 30, and 1 days, respectively) with mass balance year totals to the right. For GRACE/GRACE-FO, 2-st. dev. uncertainties that include noise, processing differences, and non-trend leakages are shown.

Overall, in the 2023 mass balance year, the Greenland Ice Sheet lost a near-average to above-average amount of ice due to above-average accumulation that was nearly balanced by above-average meltwater runoff and slightly above-average solid ice discharge.

h. Glaciers and ice caps outside Greenland

—D. Burgess, G. Wolken, B. Wouters, L. M. Andreassen, C. Florentine, J. Kohler, B. Luks, F. Pálsson, L. Sass, L. Thomson, and T. Thorsteinsson

The Arctic hosts 60% of the world's mountain glaciers and ice caps by area outside of the ice sheets of Greenland and Antarctica (RGI Consortium 2023; Fig. 5.21). While their potential longer-term contribution to sea-level rise is small compared to the ice sheets, they are highly sensitive to changes in climate (Box et al. 2019) and have been a large contributor to recent sea-level rise in response to continued atmospheric warming (Hugonnet et al. 2021; Ciracì et al. 2020; Wouters et al. 2019). Recent increases in global temperature, amplified at high northern latitudes (section 5c; Fig. 5.21), have accelerated melting of Arctic glaciers and ice caps three-fold since the mid-1990s (Zemp et al. 2019). Observations of monitored Arctic glaciers and ice caps from 2022 and 2023 show regional and inter-annual variations in mass change, with a continuing trend of significant ice loss throughout the Arctic, especially in Alaska and Arctic Canada.

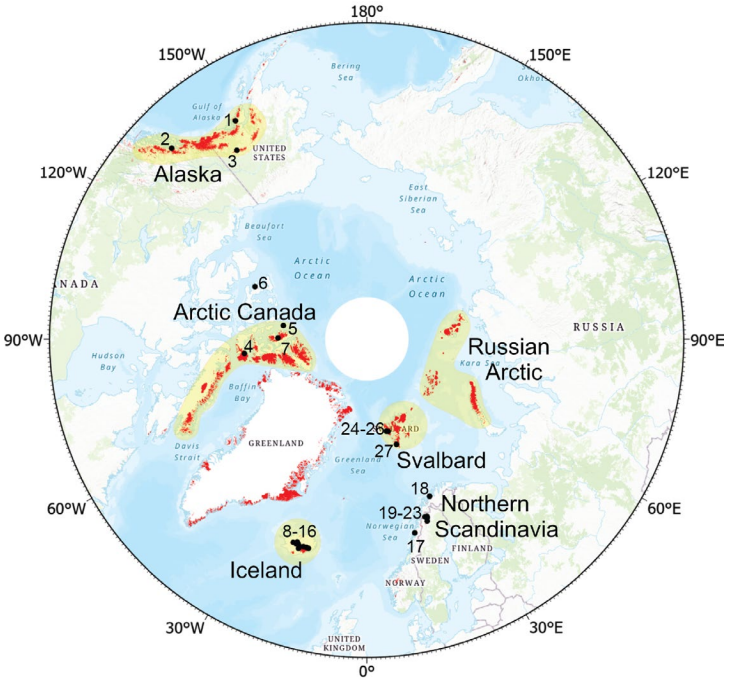

Fig. 5.21. Arctic glaciers and ice caps (red), including ice caps in Greenland that are separate from the ice sheet. Dashed lines delineate the Gravity Recovery and Climate Experiment (GRACE) and GRACE Follow-On (GRACE-FO)-derived mass anomaly domains used to estimate changes in annual glacier mass balance for heavily glacierized Arctic regions. Black dots indicate long-term Arctic glacier monitoring sites, with numbers linked to glacier/ice cap names in Table 5.1.

Glaciers and ice caps gain mass by snow accumulation and lose mass by surface melt and runoff as well as by iceberg calving, where they terminate in oceans or lakes. The total mass balance is defined as the difference between annual snow accumulation and annual mass losses (iceberg calving plus runoff). Of the 27 Arctic glaciers monitored, only Kongsvegen, Hansbreen, and Devon Ice Cap lose mass by iceberg calving, which is not accounted for in this study. We report the climatic mass balance (annual snow accumulation minus annual runoff), which is a measure of annual thickness change (in mm w.e., water equivalent) averaged across the entire ice cap or glacier.

Climatic mass balance (Bclim) is reported for the 2022/23 mass balance year (September 2022 to August 2023) for the 25 monitored Arctic glaciers for which data were available (Table 5.1). As some of these data are provisional, we add context to recent changes in pan-Arctic glacier mass balance by also reporting on 26 glaciers measured in the previous mass balance year of 2021/22 (WGMS 2024; Kjøllmoen et al. 2023). Of the 25 glaciers for which Bclim was measured in both years, five glaciers (four in Iceland, one in Norway) registered positive Bclim in 2021/22, while all glaciers monitored in 2022/23 experienced negative Bclim. Negative Bclim for all regions combined indicates net thinning for pan-Arctic monitored glaciers, with 2021/22 and 2022/23 being the 16th- and 2nd-most-negative years on record. Cumulative measurements of Bclim indicate regional thinning of ~–15 m w.e. across glaciers in Arctic Canada (1959–2023) to ~–37 m w.e. for glaciers in Alaska (1953–2023), with an overall average of ~–26 m w.e. for all regions combined (Fig. 5.22).

Regionally, the most thinning in the 2021/22 balance year occurred over Svalbard, where negative values of Bclim were recorded for Midtre Lovénbreen (–1416 mm w.e.), Austre Brøggerbreen (–1516 mm w.e.), Kongsvegen (–954 mm w.e.), and Hansbreen (–1457 mm w.e.) glaciers (Table 5.1). In Arctic Canada, the fourth-most-negative Bclim on record for the Melville Ice Cap (–1077 mm w.e.) coincided with a persistent warm surface air mass; 3°C–4°C above the 1991–2020 mean (Ballinger et al. 2022) situated over the western Queen Elizabeth Islands and

Beaufort Sea in 2022. Moderate summer melting and slightly higher-than-normal (~10%) winter snow accumulation (WGMS 2024) resulted in an average Bclim anomaly (relative to the 1991–2020 mean) of –290 mm w.e. for Alaskan monitored glaciers in 2022. Cool summer temperatures (Ballinger et al. 2022) and high winter accumulation (~20% above the 1991–2020 mean; WGMS 2024) resulted in a slightly negative mass balance of –111 mm w.e. (+637 mm w.e. relative to the 1991–2020 mean) for the monitored ice caps and glaciers in Iceland. Of the nine glaciers monitored, four on the Hofsjökull (Hofsjökull N) and Vatnajökull Ice Caps (Köldukvislarjökull, Dyngjujökull, and Bruarjökull) averaged a positive Bclim of +296 mm w.e. (st. dev. = 180 mm w.e.) for the 2021/22 balance year. Since the start of mass balance measurements in Iceland, positive Bclim has only been observed five times on Hofsjökull (since 1988), four times on Vatnajökull (since 1991), and two times on Langjökull (since 1997).

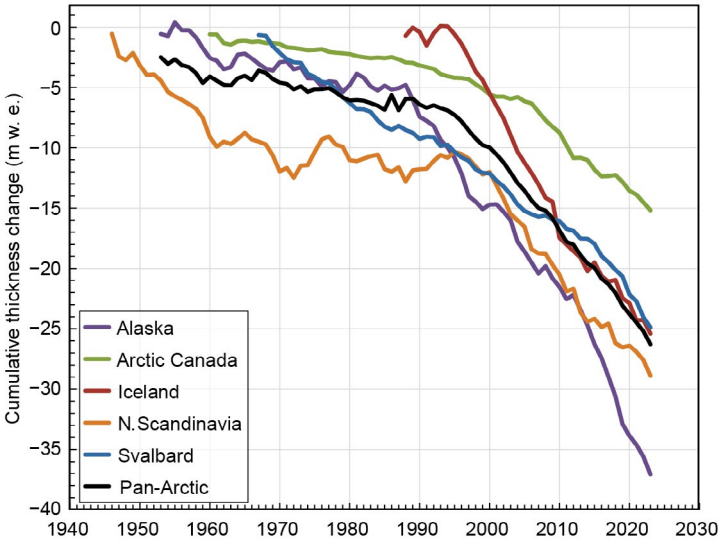

Fig. 5.22. Cumulative climatic mass balance (Bclim) in meters of water equivalent (m w.e.) for monitored glaciers in five Arctic regions and for the Arctic as a whole (pan-Arctic). Regional Bclim are derived as arithmetic means for all monitored glaciers within each region for each year, and these means are summed over the period of record and interpreted as cumulative thickness changes. Note the variable time periods over which cumulative changes are measured. Data are from the World Glacier Monitoring Service (WGMS 2024: https://wgms.ch/).

Table 5.1. Measured climatic mass balance (Bclim) for 26 glaciers in Alaska (3), Arctic Canada (4), Iceland (9), Svalbard (4), and northern Scandinavia (6) in 2021/22 and 25 measured glaciers in 2022/23, together with the 1991–2020 mean and standard deviation (* indicates one or more years of data missing from the record) for each glacier. Negative (positive) values for Bclim indicate mass loss (gain). Data were obtained from the World Glacier Monitoring Service (WGMS 2024: https://wgms.ch/) with results for 2022/23 as tentative and subject to revision. Bias corrections were applied to Bclim for Hofsjökull glaciers (N, E, and SW), Iceland, using methods outlined in Jóhannesson et al. (2013). Numbers in the left-hand column correspond to glacier locations in Fig. 5.21.

Alaska				
Glacier (record length, years)	**Bclim Mean** (mm w.e. yr^{-1}) 1991–2020	**Bclim Std. dev.** (mm w.e. yr^{-1}) 1991–2020	**Bclim** (mm w.e. yr^{-1}) 2021/22	**Bclim** (mm w.e. yr^{-1}) 2022/23
1) Wolverine (58)	–770	984	–1110	–1080
2) Lemon Creek (71)	–1200	839	–1440	–2250
3) Gulkana (58)	–759	830	–1050	–180
Arctic Canada				
Glacier (record length, years)	**Bclim Mean** (mm w.e. yr^{-1}) 1991–2020	**Bclim Std. dev.** (mm w.e. yr^{-1}) 1991–2020	**Bclim** (mm w.e. yr^{-1}) 2021/22	**Bclim** (mm w.e. yr^{-1}) 2022/23
4) Devon Ice Cap (63)	–257	215	–508	–388
5) Meighen Ice Cap (64)	–326	422	–451	–549
6) Melville S. Ice Cap (61)	–458	487	–1077	–1032
7) White (64)	–341	323	–545	–660

Iceland				
Glacier (record length, years)	**Bclim Mean** (mm w.e. yr^{-1}) 1991–2020	**Bclim Std. dev.** (mm w.e. yr^{-1}) 1991–2020	**Bclim** (mm w.e. yr^{-1}) 2021/22	**Bclim** (mm w.e. yr^{-1}) 2022/23
8) Langjökull S. Dome (27)	–1247	841*	–50	–1430
9) Hofsjökull E (35)	–980	840	–490	–1510
10) Hofsjökull N (36)	–820	706	+30	–1320
11) Hofsjökull SW (35)	–960	951	–50	–1200
12) Köldukvislarjökull (32)	–466	707*	+386	–740
13) Tungnaarjökull (32)	–1141	780*	–1355	–1529
14) Dyngjujökull (31)	–44	792	+422	–308
15) Brúarjökull (30)	–237	621*	+344	–713
16) Eyjabakkajökull (32)	–700	766	–359	–1417

Scandinavia				
Glacier (record length, years)	**Bclim Mean** (mm w.e. yr^{-1}) 1991–2020	**Bclim Std. dev.** (mm w.e. yr^{-1}) 1991–2020	**Bclim** (mm w.e. yr^{-1}) 2021/22	**Bclim** (mm w.e. yr^{-1}) 2022/23
17) Engabreen (54)	–62	972	+145	–1101
18) Langfjordjokulen (33)	–953	771*	–1909	–1652
19) Marmaglaciaren (32)	–494	568*	–427	–1256
20) Rabots (42)	–533	648*	–943	–1565
21) Riukojietna (37)	–701	734*	–795	–1347
22) Storglaciaren (78)	–235	747	–212	–812
23) Tarfalaglaciaren (30)	–331	1170	—	—

Svalbard				
Glacier (record length, years)	**Bclim Mean** (mm w.e. yr^{-1}) 1991–2020	**Bclim Std. dev.** (mm w.e. yr^{-1}) 1991–2020	**Bclim** (mm w.e. yr^{-1}) 2021/22	**Bclim** (mm w.e. yr^{-1}) 2022/23
24) Midre Lovenbreen (56)	–498	407	–1416	–976
25) Austre Broggerbreen (57)	–619	451	–1516	–948
26) Kongsvegen (37)	–146	404	–954	–622
27) Hansbreen (34)	–419	469*	–1457	—

Arctic-wide glacier thinning in 2022/23 was strongest in Scandinavia, where the Bclim average was ~801 mm w.e. more negative than the 1991–2020 mean. Notably, extreme melt across Langfjordjokulen (Bclim = –1652 mm w.e.) coincided with the second consecutive year that summer ablation has extended across the entire glacier surface (Kjøllmoen et al. 2023). Icelandic glacier mass balance in 2022/23 was opposite of the previous year, with enhanced summer melting (section 5c) and reduced winter accumulation resulting in the seventh-most-negative Bclim on record (–1238 mm w.e.; WGMS 2024) for this region. Reduced winter accumulation along the Gulf of Alaska coastline (section 5i) contributed to a low negative Bclim anomaly of –260 mm w.e. for Alaskan glaciers in the 2022/23 balance year.

Glaciers and ice caps at high northern latitudes have been increasingly important contributors to global sea-level rise since the early 1990s (Box et al. 2018). Gravity anomalies measured from the combined GRACE (2002–16) and GRACE-FO (2018–23) satellite missions indicate that pan-Arctic glaciers and ice caps have lost mass at a rate of –177±21 Gt yr^{-1} since 2002 (Fig. 5.23; methods as per Wouters et al. 2019). This rate of annual mass loss was sustained primarily by shrinkage of ice caps and glaciers in Arctic Canada (44%), Svalbard (25%), and the Russian Arctic (21%), which resulted in pan-Arctic losses of –191±20 Gt for the 2021/22 balance year. Decreased mass loss from pan-Arctic glaciers to –157±29 Gt in 2022/23 was associated mainly with reduced mass loss from Arctic Canada, which accounted for only 11% of the 2022/23 total. Conversely, mass loss of –86±40 Gt from Alaskan glaciers accounted for 55% of the total ablated mass in the 2022/23 balance year. Mass loss from pan-Arctic glaciers and ice caps totaling –348±49 Gt between September 2021 and August 2023 contributed 0.96±0.14 mm to global sea-level rise for this two-year period.

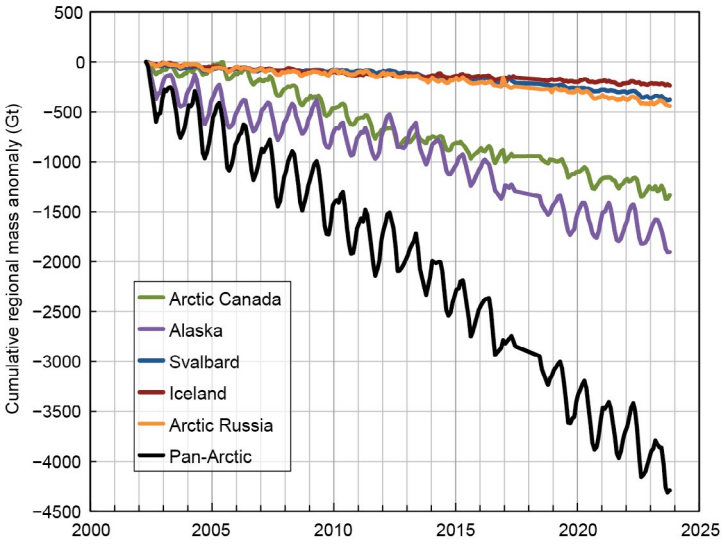

Fig. 5.23. Cumulative changes in regional total stored water (Gt) for the period 2002–23 derived from the Gravity Recovery and Climate Experiment (GRACE) and GRACE Follow-On (GRACE-FO) satellite gravimetry for the five regions shown in Fig. 5.21 and for the total of these five regions (i.e., pan-Arctic). Linear interpolation is applied through a measurement gap between the GRACE and GRACE-FO missions from Jul 2017 to May 2018.

i. Terrestrial snow cover

—L. Mudryk, A. Elias Chereque, C. Derksen, K. Luojus, and B. Decharme

Many components of the Arctic land surface are directly influenced by snow cover, including the surface energy budget, permafrost, terrestrial and freshwater ecosystems, and the ground thermal regime, with implications on the carbon cycle (Brown et al. 2017; Meredith et al. 2019; and references therein). Even following the snow-cover season, the influence of spring snow-melt timing persists through impacts on river-discharge timing and magnitude, surface water, soil moisture, vegetation phenology, and fire risk (Meredith et al. 2019).

Historical snow-cover extent (SCE) anomalies (relative to the 1991–2020 baseline) for May and June are shown separately for the North American and Eurasian sectors of the Arctic in Fig. 5.24 (data from the NOAA snow chart climate data record; Robinson et al. 2012; see also section 2c5). In 2023, North American May SCE was at a record low (lowest extent in the 57-year record) associated with spring temperatures up to 5°C above normal across the region (section 5c, see Fig. 5.6b), but rebounded slightly by June (fourth lowest). In the Eurasian sector, May anomalies were close to the 1991–2020 average but were well below normal by June (ninth lowest in the 57-year record).

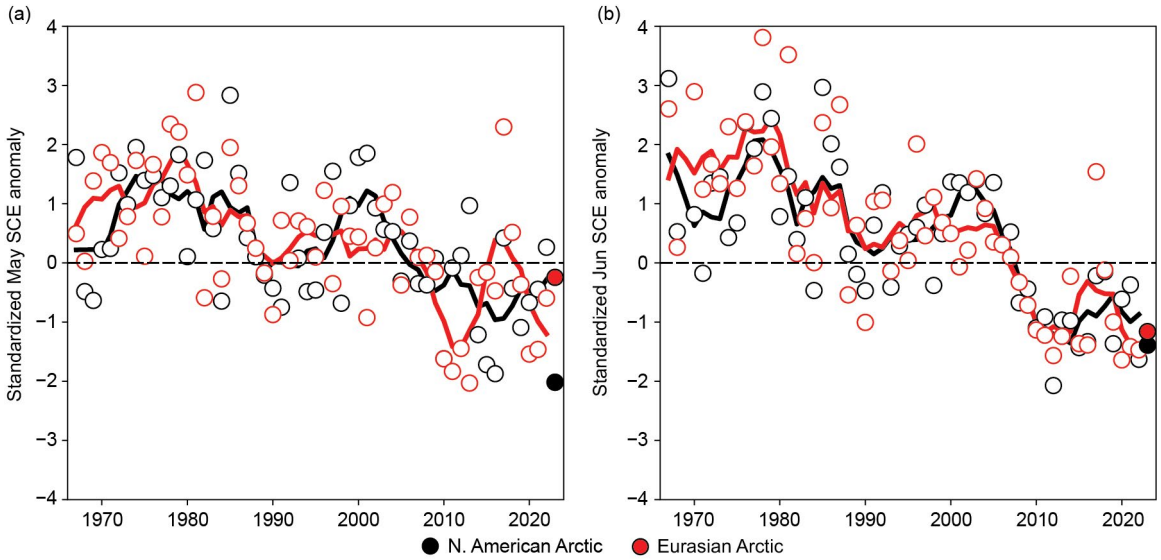

Fig. 5.24. Monthly snow cover extent (SCE) anomalies for Arctic terrestrial land areas (>60°N) for (a) May and (b) Jun from 1967 to 2023. Anomalies are relative to the average for 1991–2020 and standardized (each observation differenced from the mean and divided by the standard deviation, and thus unitless). Solid black and red lines depict five-year running means for North America and Eurasia, respectively. Filled circles highlight 2023 anomalies. (Source: Robinson et al. 2012.)

Snow-cover duration (SCD) anomalies for the 2022/23 snow season (relative to a 1998/99 to 2017/18 climatology) are shown across the Arctic in Figs. 5.25a,b (data from the NOAA daily Interactive Multisensor Snow and Ice Mapping System snow cover product; U.S. National Ice Center 2008). Anomalies in the total number of days with snow cover were computed separately for each half of the snow season: August 2022 to January 2023, referred to as "onset period" (Fig. 5.25a), and February 2023 to July 2023, referred to as "melt period" (Fig. 5.25b). Snow-cover duration anomalies indicate a combination of early and late snow onset with an especially variable pattern across the North American Arctic. Across central and eastern Eurasia, Arctic snow onset occurred earlier than normal while across western Eurasia there was a modest delay. While spring snow melt across Eurasia was not as extensive as in the previous two years (Thoman et al. 2022; Moon et al. 2023), far northern coastal regions across the continent still had above-normal numbers of snow-free days, indicative of earlier snow melt. Across North America, the extensive snow melt signaled by record-low May SCE is also apparent in spring SCD anomalies, where a broad swath of mainland Nunavut and Northwest Territories in Canada saw an increase of more than 50% in the number of snow-free days during the melt period. The early spring snow melt seen there was compounded by summer precipitation deficits (section 5d, see

Fig. 5.8c) and together likely contributed to the extensive summer 2023 wildfire season (see Sidebar 7.1), which forced the complete evacuation of numerous communities in the western Canadian Arctic.

Finally, snow-water equivalent (SWE), a measure of snow amount, is used to characterize Arctic snow accumulation over the 2022/23 season. The SWE fields during April–June were obtained from four daily-frequency gridded products over the 1981–2023 period: 1) the European Space Agency Snow Climate Change Initiative (CCI) SWE version 1 product derived through a combination of satellite passive microwave brightness temperatures and climate station snow depth observations (Luojus et al. 2022); 2) MERRA-2; (GMAO 2015) daily SWE fields; 3) SWE output from the ERA5-Land analysis (Muñoz Sabater 2019); and 4) the physical snowpack model

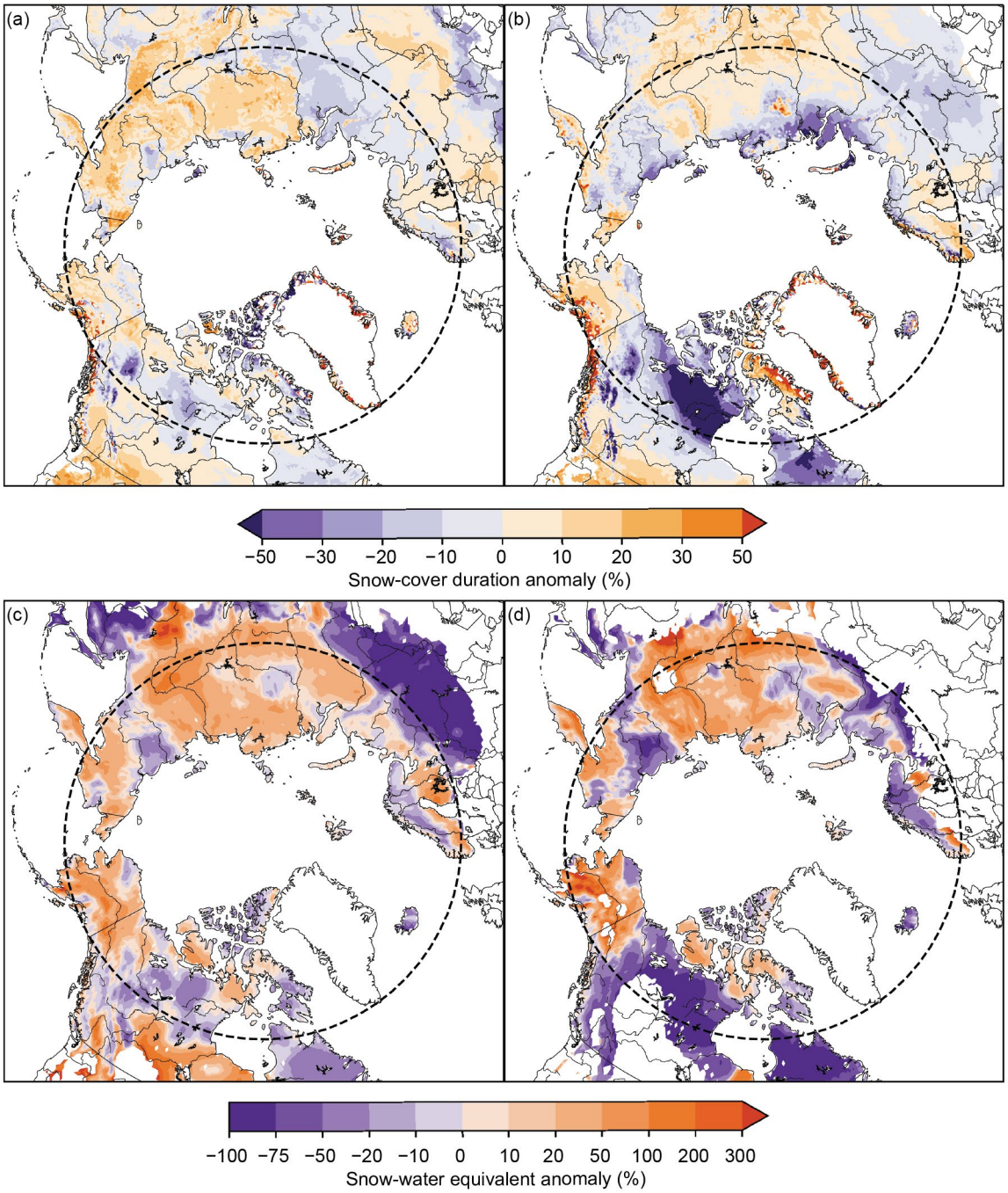

Fig. 5.25. Snow-cover duration anomalies (% difference relative to the climatological number of snow-free days for the 1998/99–2017/18 baseline) for the 2022/23 snow year: (a) snow onset period (Aug 2022–Jan 2023) and (b) snow melt period (Feb 2023–Jul 2023). Purple (orange) indicates more (fewer) snow-free days than average. Snow water equivalent (SWE) anomalies (% difference from the 1991–2020 baseline) in 2023 for (c) Apr and (d) May. Purple (orange) indicates lower (higher) snow amounts than average. Latitude 60°N is marked by the gray dashed circle; land north of this defines the Arctic terrestrial area considered in this study. (Source: [a],[b] U.S. National Ice Center [2008]; [c],[d] four SWE products from Snow CCI [Luojus et al. 2022]; MERRA2 [GMAO 2015]; ERA5-Land [Muñoz Sabater 2019]; and Crocus [Brun et al. 2013].)

Crocus (Brun et al. 2013) driven by near-surface meteorological variables from ERA5. Reduced availability of climate-station snow depth measurements limits the accuracy of the Snow CCI SWE product during May and June, hence it is omitted for those months. An approach using gridded products is required because in situ observations alone are too sparse to be representative of hemispheric snow conditions, especially in the Arctic.

For April, the SWE fields from each product were aggregated across the Arctic land surface (>60°N) for both North American and Eurasian sectors and standardized relative to the 1991–2020 baseline to produce standardized April snow-mass anomalies. The ensemble mean anomalies and the range of product estimates are presented in Fig. 5.26. April is chosen because it is the approximate month that total snow mass across the terrestrial pan-Arctic region peaks, reflecting total snowfall accumulations since the preceding autumn and before increasing May and June temperatures lead to melt. Snow-mass anomalies for April 2023 indicate snow accumulation above the 1991–2020 baseline across both continents (consistent with the wet winter reported in section 5d), but especially in Eurasia where it was the fifth-highest accumulation in the record. The spatial patterns of monthly mean SWE (Figs. 5.25c,d) illustrate how this accumulation varied regionally during April and May. Regions with positive SWE anomalies in April intensified through May (most of Alaska, large parts of central and eastern Siberia), which suggests that snow in these regions took longer to melt compared to the historical baseline (also supported by the longer-than-normal snow-cover duration during the melt season in Fig. 5.25b). However, mainland Arctic Canada experienced extensive reductions in SWE during May that extended northward into the southern Canadian Arctic Archipelago during June (not shown). By this time, snow had mostly melted across both continents except for Baffin and the Queen Elizabeth Islands in the Canadian Arctic Archipelago.

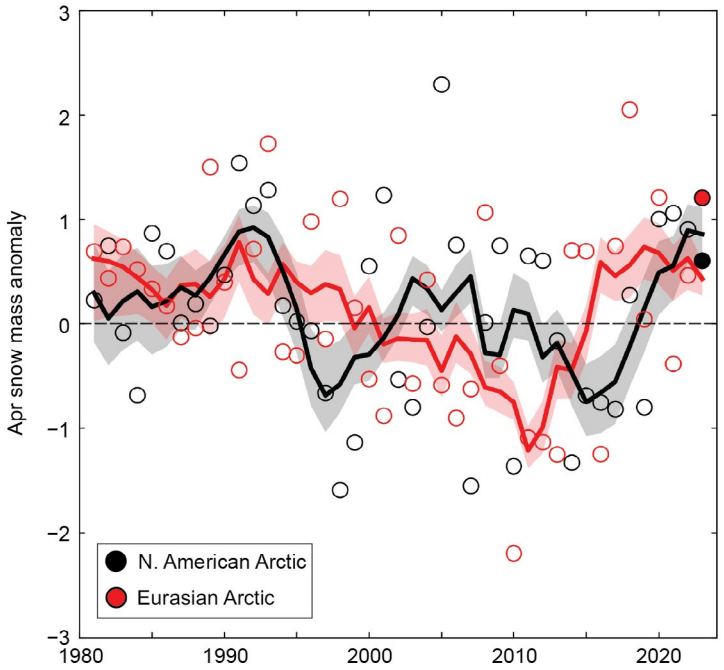

Fig. 5.26. Mean Apr snow-mass anomalies for Arctic terrestrial areas calculated for North American (black) and Eurasian (red) sectors of the Arctic over the period 1981–2023. Anomalies are relative to the 1991–2020 average and standardized (each observation differenced from the mean and divided by the standard deviation, and thus unitless). Filled circles highlight 2023 anomalies. Solid black and red lines depict five-year running means for North America and Eurasia, respectively, and the spread among the running means for individual datasets is shown in shading. (Source: Four snow water equivalent products from Snow CCI [Luojus et al. 2022], MERRA2 [GMAO 2015], ERA5-Land [Muñoz Sabater 2019], and Crocus [Brun et al. 2013].)

Overall, the 2022/23 snow season shares similarities with those from several recent years. Despite above-average seasonal snow accumulation, large springtime temperature anomalies still resulted in earlier-than-normal melt. During the 2022/23 season, this earlier-than-normal melt occurred across portions of North America, whereas in previous years, it occurred on the Eurasian continent. Looking historically across Eurasia, the June snow-extent values for 11 of the past 14 years represent near-complete absence of snow cover across the continent except for residual amounts in higher-elevation locations. Compared to historical conditions, early Eurasian spring melt has resulted in approximately two additional weeks of snow-free conditions.

j. Permafrost

—S. L. Smith, V. E. Romanovsky, K. Isaksen, K. E. Nyland, N. I. Shiklomanov, D. A. Streletskiy, and H. H. Christiansen

Permafrost refers to earth materials (e.g., bedrock, mineral soil, organic matter) that remain at or below 0°C for at least two consecutive years, although most permafrost has existed for centuries to many millennia. Extensive regions of high-latitude landscapes are underlain by permafrost. The active layer, which thaws and refreezes annually, overlies the permafrost. Warming of permafrost (especially if ice-rich), active layer thickening, and ground-ice melt cause changes in surface topography, hydrology, and landscape stability, with implications for Arctic infrastructure, ecosystem integrity, and human livelihoods (Romanovsky et al. 2017; Hjort et al. 2022; Wolken et al. 2021). Changes in permafrost conditions can also affect the rate of greenhouse gas release to the atmosphere, potentially accelerating global warming (Miner et al. 2022; Schuur et al. 2022).

Permafrost conditions respond to shifts in the surface energy balance through a combination of interrelated changes in ground temperature and active layer thickness (ALT). Ground temperatures fluctuate seasonally near the surface, while below the depth of seasonal temperature variation they reflect longer-term climate. Long-term changes in permafrost temperatures are driven by changes in air temperature (Romanovsky et al. 2017); however, permafrost temperature trends also show local variability due to other influences such as snow cover, vegetation characteristics, and soil moisture (Smith et al. 2022). Monitoring sites across the Arctic (Fig. 5.27) have been recording ground temperature in the upper 30 m for up to five decades, providing critical data on changes in permafrost condition. Observed changes in ALT are more reflective of shorter-term (year-to-year) fluctuations in climate and are especially sensitive to changes in summer air temperature and precipitation.

Permafrost temperatures continue to increase on a decadal time scale across the Arctic. Greater increases are generally observed in colder permafrost (temperature <–2°C) at higher latitudes (Smith et al. 2022, 2023), partly due to greater increases in air temperature (Figs. 5.27, 5.28). Over the last 29 years, positive ALT trends (Fig. 5.29) are evident from all permafrost regions examined, but trends are less apparent for the Alaskan North Slope, northwest Canada, and East Siberia (Smith et al. 2023).

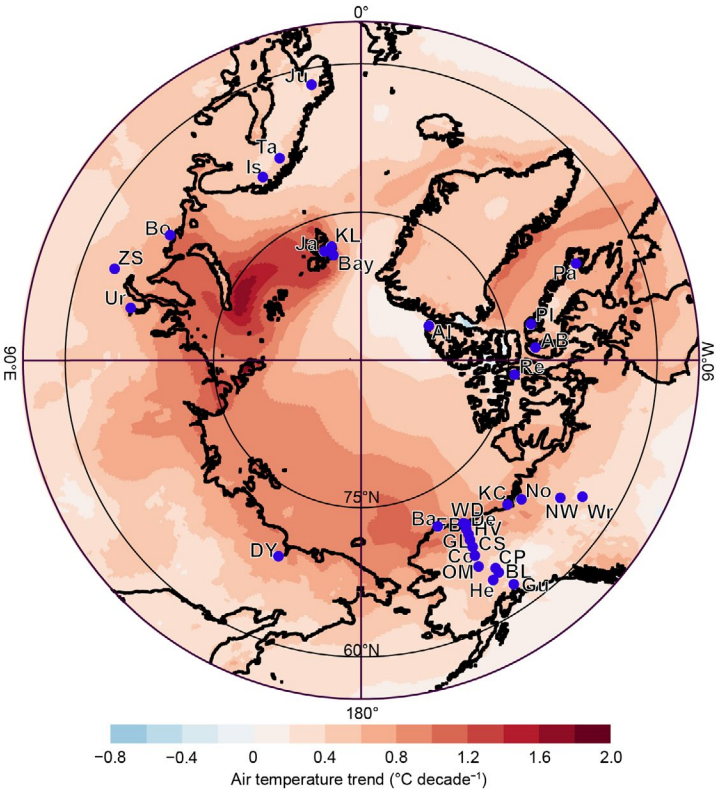

Fig. 5.27. Locations of the permafrost temperature monitoring sites (for which data are shown in Fig. 5.28), superimposed on average surface air temperature trends (°C decade^{-1}) during 1981–2023 from ERA5 reanalysis (Hersbach et al. 2020; data available at https://cds.climate.copernicus.eu), which largely covers the period of record for permafrost monitoring. See Table 5.2 for site names. Information about these sites is available at http://gtnpdatabase.org/ and https://permafrost.gi.alaska.edu/sites_map.

1. PERMAFROST TEMPERATURES

Permafrost temperatures in 2023 were the highest on record at 9 of 17 sites reporting (Table 5.2). However, cooling that began in 2020 has continued at some sites, and temperatures were lower in 2023 compared to 2022 at six North American sites (Figs. 5.28a,b). In the Beaufort-Chukchi region, permafrost temperatures in 2023 were <0.1°C lower than in 2022 at three sites (Fig. 5.28a). The observed permafrost cooling in this region resulted from lower mean annual air temperatures after 2019. At Deadhorse (Prudhoe Bay, Alaska), for example, the average air temperature was almost 4°C lower in 2022 compared to 2018 and 2019. However, the air temperature in 2023 was similar to 2018 and 2019, being 3°C higher than 2022,

but the full effect is not yet observed at depths of 15 m–20 m. For discontinuous permafrost in Alaska and northwestern Canada, the 2023 permafrost temperatures were the highest on record at two of six sites reporting with slightly lower or similar temperatures compared to 2022 at the other sites (Fig. 5.28b). In the high Arctic cold permafrost of Svalbard, where there was a short period of cooling after 2020 (Isaksen et al. 2022b), permafrost was warmer in 2023 compared to 2022 (Fig. 5.28d). In warmer permafrost at other Nordic sites, temperatures in 2023 were the highest on record (Fig. 5.28d; Table 5.2).

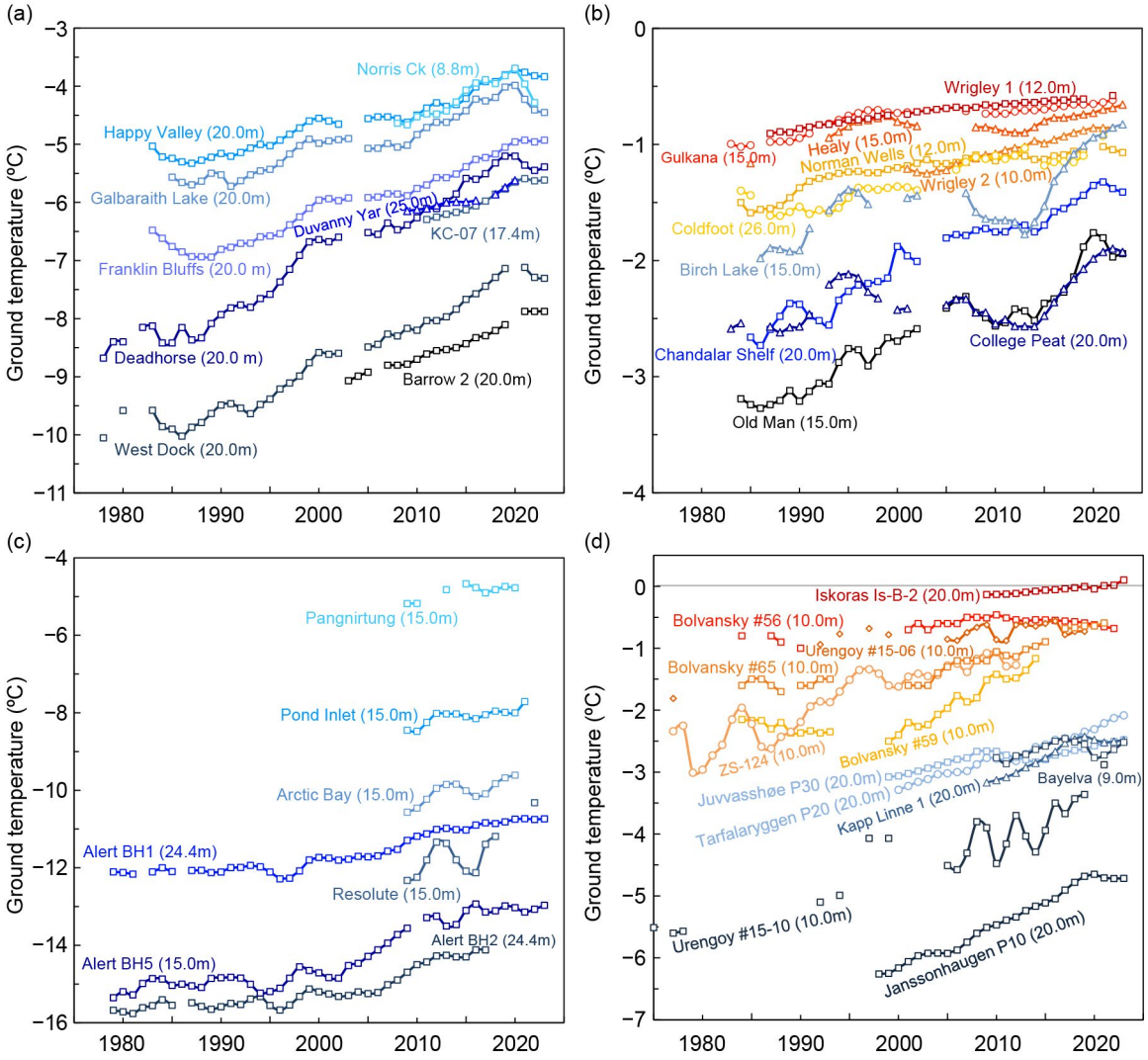

Fig. 5.28. Time series of mean annual ground temperature (°C) at depths of 9 m–26 m below the surface at selected measurement sites that fall roughly into Adaptation Actions for a Changing Arctic Project priority regions (see Romanovsky et al. 2017): (a) cold continuous permafrost of northwestern North America and northeastern East Siberia (Beaufort-Chukchi region); (b) discontinuous permafrost in Alaska and northwestern Canada; (c) cold continuous permafrost of eastern and High Arctic Canada (Baffin Davis Strait); and (d) continuous to discontinuous permafrost in Scandinavia, Svalbard, and Russia/Siberia (Barents region). Temperatures are measured at or near the depth of zero annual amplitude where the seasonal variations of ground temperature are less than 0.1°C. Note differences in y-axis value ranges. Red and orange lines are used for warmer permafrost, and blue and black lines are used for colder permafrost. Borehole locations are shown in Fig. 5.27 (data are updated from Smith et al. 2023).

Throughout the Arctic, warming of permafrost with temperatures ~0°C to –2°C is slower (generally <0.3°C decade^{-1}) than colder permafrost sites due to latent heat effects related to melting ground ice. At cold continuous permafrost sites in the Beaufort-Chukchi region, permafrost temperatures have increased by 0.4°C decade^{-1} to 0.8°C decade^{-1} with similar increases (0.4°C decade^{-1} to 1.1°C decade^{-1}) for the eastern and high Canadian Arctic (Figs. 5.28a,c; Table 5.2). Permafrost in Svalbard (Janssonhaugen and Kapp Linne) has warmed by up to 0.7°C decade^{-1} (Fig. 5.28d; Table 5.2), and significant permafrost warming has been detected to 100-m depth at Janssonhaugen (Isaksen et al. 2022b).

Table 5.2. Rate of change in mean annual ground temperature (°C decade^{-1}) for permafrost monitoring sites shown in Fig. 5.27. The periods of record are shown in parenthesis below the rates of change. For sites where measurements began prior to 2000, the rate of change for the entire available record and the period after 2000 are provided. Stations with record-high 2023 temperatures are underlined in red. Asterisks denote sites not reporting in 2023.

Region	Site	Entire Record	Since 2000
Northeast Siberia *(Beaufort-Chukchi Region)*	Duvany Yar (DY)*	NA	+0.4 (2009–20)
Alaskan Arctic plain *(Beaufort-Chukchi Region)*	West Dock (WD), Deadhorse (De), Franklin Bluffs (FB), Barrow (Ba)	+0.5 to +0.8 (1978–2023)	+0.5 to +0.7 (2000–23)
Northern foothills of the Brooks Range, Alaska *(Beaufort-Chukchi Region)*	Happy Valley (HV), Galbraith Lake (GL)	+0.4 (1983–2023)	+0.4 (2000–23)
Northern Mackenzie Valley *(Beaufort-Chukchi Region)*	Norris Ck (No)*, KC-07 (KC)	NA	+0.6 to +0.7 (2008–23)
Southern foothills of the Brooks Range, Alaska *(Discontinuous Permafrost: Alaska and NW Canada)*	Coldfoot (Co)*, Chandalar Shelf (CS), Old Man (OM)	+0.1 to +0.3 (1983–2023)	+0.2 to +0.3 (2000–23)
Interior Alaska *(Discontinuous Permafrost: Alaska and NW Canada)*	College Peat (CP), Birch Lake (BL), Gulkana (Gu)*, Healy (He)	+0.1 to +0.3 (1983–2023)	<+0.1 to +0.4 (2000–23)
Central Mackenzie Valley *(Discontinuous Permafrost: Alaska and NW Canada)*	Norman Wells (NW), Wrigley (Wr)*	+0.1 (1984–2023)	+0.1 to +0.2 (2000–23)
Baffin Island *(Baffin Davis Strait Region)*	Pangnirtung (Pa)*, Pond Inlet (PI)*	NA	+0.4 (2009–21)
High Canadian Arctic *(Baffin Davis Strait Region)*	Resolute (Re)*	NA	+1.1 (2009–22)
High Canadian Arctic *(Baffin Davis Strait Region)*	Alert (Al) @ 15 m, Alert (Al) @ 24 m	+0.6, +0.4 (1979–2023)	+0.9, +0.6 (2000–23)
Northwest Siberia *(Barents Region)*	Urengoy 15-06* and 15-08* (Ur)	+0.2 to +0.5 (1974–2021)	+0.1 to +0.8 (2005–21)
Russian European North *(Barents Region)*	Bolvansky 56* and 65* (Bo)	+0.1 to +0.3 (1984–2022)	0 to +0.5 (2001–22)
Svalbard *(Barents Region)*	Janssonhaugen (Ja), Bayelva (Bay)*, Kapp Linne 1 (KL)	+0.7 (1998–2023)	+0.1 to +0.7 (2000–23)
Northern Scandinavia *(Barents Region)*	Tarfalarggen (Ta), Iskoras Is-B-2 (Is)	NA	+0.1 to +0.5 (2000–23)
Southern Norway *(Barents Region)*	Juvvasshøe (Ju)	+0.2 (1999–2023)	+0.2 (2000–23)

In the discontinuous permafrost regions of Scandinavia (Juvvasshøe and Iskoras), warming is continuing at rates of about 0.1°C decade^{-1} to 0.2°C decade^{-1}, with thawing occurring at Iskoras (Fig. 5.28d; Isaksen et al. 2022b). Similar rates (Figs. 5.28b,d) are observed in the warm permafrost of northwestern North America (e.g., Smith et al. 2024) and Russia (Malkova et al. 2022).

2. ACTIVE LAYER THICKNESS

Active layer thickness is measured directly using mechanical probing and thaw tubes and indirectly by interpolating the maximum seasonal depth of the 0°C isotherm from borehole

temperature records. The ALT trends shown in Fig. 5.29 are primarily generated from spatially distributed mechanical probing across representative landscapes to determine the depth to the top of permafrost.

The Alaskan Interior and West Siberia experienced 2023 ALT well above the 2009–18 mean, continuing a several-year extreme trend in these regions (e.g., Kaverin et al. 2021). Increases in ALT are greatest for the Alaskan Interior, the Russian European North, and West Siberia at 0.03 m yr^{-1}, 0.01 m yr^{-1}, and 0.02 m yr^{-1}, respectively.

The ALT regional anomalies for 2023 were within 0.1 m of the 2009–18 mean for the North Slope of Alaska, Greenland, northwest Canada (2022), and East Siberia. Negligible trends in ALT from ice-rich sites on the North Slope of Alaska have been attributed to subsidence (Nyland et al. 2021). Widespread thaw and subsidence across northwest Canada have been documented (O'Neill et al. 2023). Consolidation within the ice-rich shallow permafrost layer resulting from decadal and longer-term thaw may not be detected with manual probing alone, and correcting ALT for ground surface displacement can improve the correspondence between increasing air temperatures and thaw depth (Nyland et al. 2021; Smith et al. 2022). Reduced ALT in 2023 for some regions, including Greenland, the Russian European North, and East Siberia, could also be due to short-term cooling superimposed on the overall positive trend (Smith et al. 2023). In Svalbard, record-high ALT anomalies occurred after western Spitsbergen experienced its warmest summer on record.

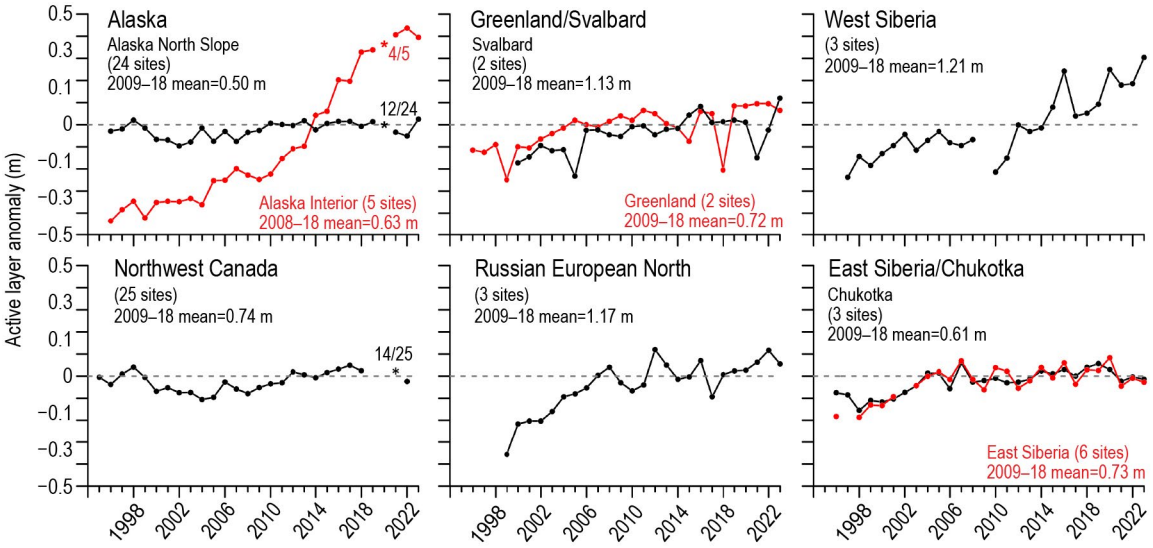

Fig. 5.29. Average annual active layer thickness (ALT) anomalies, relative to the 2009–18 mean, for six Arctic regions observed by the Circumpolar Active Layer Monitoring program. Positive and negative anomalies indicate thicker or thinner ALT than the 10-yr reference, respectively. Numbers of sites vary by region because only sites with >20 years of continuous thaw depth observations from the end of the thaw season are included. Asterisks represent atypical observations, for example, due to pandemic-related restrictions (fraction of sites for these years are provided on graph). Canadian ALT is derived from thaw tubes that record the maximum thaw depth over the previous year. Since Canadian sites were not visited in 2020 and 2021, the maximum thaw depth recorded during the 2022 visit could have occurred any summer from 2019 through 2021, although the data point is plotted in 2021. Site-specific data and metadata are available at www2.gwu.edu/~calm/.

k. Tundra greenness

—G. V. Frost, M. J. Macander, U. S. Bhatt, L. T. Berner, J. W. Bjerke, H. E. Epstein, B. C. Forbes, G. Jia, M. J. Lara, P. M. Montesano, R. Í. Magnússon, C. S. R. Neigh, G. K. Phoenix, H. Tømmervik, C. Waigl, D. A. Walker, and D. Yang

The Arctic tundra biome occupies Earth's northernmost lands, collectively encompassing a 5.1 million km^2 region that resembles a wreath bound by the Arctic Ocean to the north and the boreal forest biome to the south (Raynolds et al. 2019). While Arctic tundra ecosystems are treeless and lack the vertical structure of forest ecosystems, they are heterogeneous across multiple spatial scales, ranging from large-scale latitudinal climate gradients to local-scale gradients of soil, hydrological, and permafrost conditions (Fig. 5.30). The Arctic tundra biome is a global hotspot of contemporary environmental change due to the sensitivity of these ecosystems to rapidly changing temperature, sea-ice, snow, and permafrost conditions (Bhatt et al. 2021; sections 5c, 5e, 5i, 5j, respectively). In the late 1990s, Earth-observing satellites began to detect a sharp increase in the productivity of tundra vegetation, a phenomenon known today as "the greening of the Arctic."

Global vegetation has been continuously monitored from space since late 1981 by the Advanced Very High Resolution Radiometer (AVHRR), a series of sensors that is well into its fifth decade of operation onboard a succession of polar-orbiting satellites. In 2000, the Moderate Resolution Imaging Spectroradiometer (MODIS) entered service and provides an independent, complementary data record with higher spatial resolution and improved calibration, with future continuity ensured by the Visible Infrared Imaging Radiometer Suite (VIIRS) sensors, first launched in 2011 (Román et al. 2024). All of these spaceborne sensors monitor global vegetation greenness using

Fig. 5.30. The Arctic tundra biome spans wide climatic and environmental gradients that produce strong contrasts in vegetation biomass and height. High Arctic ecosystems support discontinuous cover of low-growing plants (upper left; Svalbard Archipelago, Norway), while warmer parts of the Low Arctic support mosaics of open tundra and tall shrubs (upper right; Ural Mountains foothills, northwestern Siberia). Tundra shrub expansion is a key driver of Arctic greening; tree expansion has also been documented but has generally been much slower (lower left; Brooks Range, Alaska). Permafrost processes, ecological disturbances, extreme weather events, and Arctic herbivores such as muskox (lower right; Yukon-Kuskokwim Delta, Alaska) introduce important sources of local variability that operate against the backdrop of long-term trends. Photos by G. Phoenix (upper left), G. V. Frost (upper right), and L. Berner (bottom row).

the Normalized Difference Vegetation Index (NDVI), a spectral metric that exploits the unique way in which green vegetation absorbs and reflects visible and infrared light.

The long-term AVHRR NDVI dataset reported here is GIMMS-3g+ with a spatial resolution of about 8 km (Pinzon et al. 2023). For MODIS, we computed trends at a much higher spatial resolution of 500 m, combining 16-day NDVI products from the *Terra* (MOD13A1, version 6.1) and *Aqua* (MYD13A1, version 6.1) satellites (Didan 2021a,b), referred to as MODIS MCD13A1. All data were masked to the extent of the Circumpolar Arctic Vegetation Map (Raynolds et al. 2019) and exclude permanent ice and water. We summarize the GIMMS-3g+ and MODIS records for the annual maximum NDVI (MaxNDVI), the peak greenness value observed in midsummer.

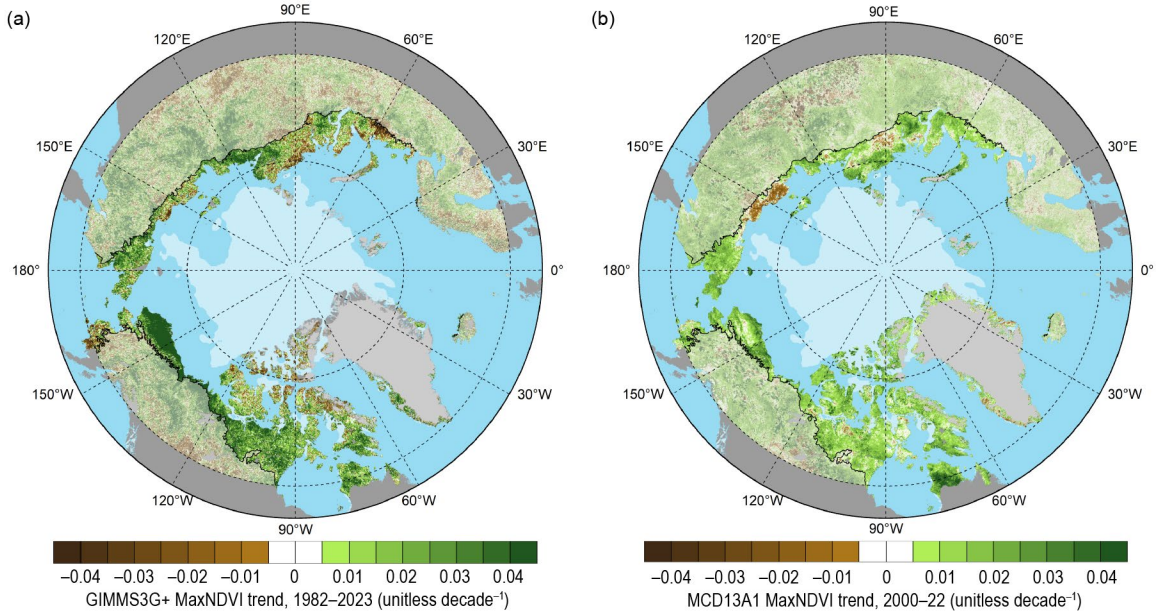

Fig. 5.31. Magnitude of the maximum Normalized Difference Vegetation Index (MaxNDVI) trend calculated as the change decade^{-1} via ordinary least-squares regression for Arctic tundra (solid colors), and boreal forest (muted colors) north of 60° latitude during (a) 1982–2022 based on the AVHRR GIMMS 3-g+ dataset, and (b) 2000–23 based on the MODIS MCD13A1 dataset. The circumpolar treeline is indicated by a black line, and the 2023 minimum sea-ice extent is indicated by light shading in each panel.

Both AVHRR and MODIS have recorded increasing MaxNDVI across most of the Arctic since 1982 and 2000, respectively (Figs. 5.31a,b), with the strongest greening trends in northern Alaska, continental Canada, and north-central Siberia. Both sensors show virtually identical trends in circumpolar mean MaxNDVI for the period of overlap (2000–23; Fig. 5.32), but the AVHRR record displays higher interannual variability and there are some differences in the trend spatial pattern. The AVHRR record generally shows strong greening in warmer, continental areas near treeline, but declining NDVI ("browning") in the High Arctic, particularly the Canadian Arctic Archipelago. MODIS has recorded greening virtually throughout the circumpolar Arctic except in portions of north-central and northeastern Siberia. Some of the AVHRR versus MODIS differences may reflect the different observational periods of the two records. The neighboring boreal forest biome

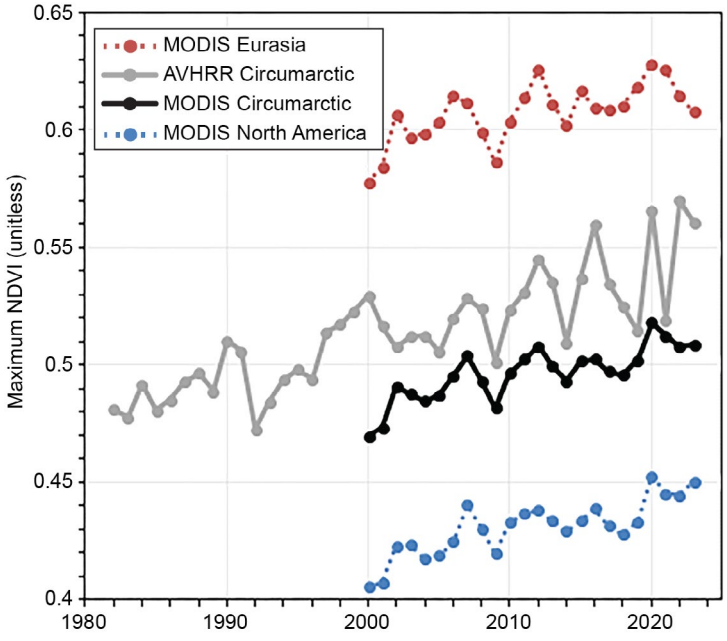

Fig. 5.32. Time series of the maximum Normalized Difference Vegetation Index (MaxNDVI) from the long-term AVHRR GIMMS-3g+ dataset (1982–2023) for the circumpolar Arctic (gray) and from the MODIS MCD13A1 (2000–23) dataset for the Eurasian Arctic (red), North American Arctic (blue), and the circumpolar Arctic (black).

(see Figs. 5.30a,b, 5.31), distributed across the North American and Eurasian continents, has also experienced rapid environmental change in recent decades and exhibits mixed trends that are linked to interactions among climate change, wildfire, human land use, and other factors (Berner and Goetz 2022).

In 2023, the circumpolar mean MaxNDVI for tundra regions was the third-highest value ever observed in both satellite records (Fig. 5.32). The AVHRR-observed MaxNDVI declined 1.9% from the record-high value set the previous year, while the MODIS-observed value increased slightly (0.3%) from the previous year. Notably, the three highest values in both the 42-year AVHRR and 24-year MODIS records have all been recorded within the last four years. Tundra greenness was much higher than normal across most of the North American Arctic and especially in the eastern Beaufort Sea region, which experienced exceptionally warm summer temperatures (Fig. 5.33; section 5c). The Eurasian Arctic, however, displayed comparatively low tundra greenness values, particularly in the East Siberian Sea region where sea ice remained extensive for much of the summer (Fig. 5.33), and newly burned areas have accumulated after multiple wildfires during 2019–23 (Zhu et al. 2023). Nonetheless, the overall trend in MODIS-observed circumpolar MaxNDVI remains strongly positive (greening).

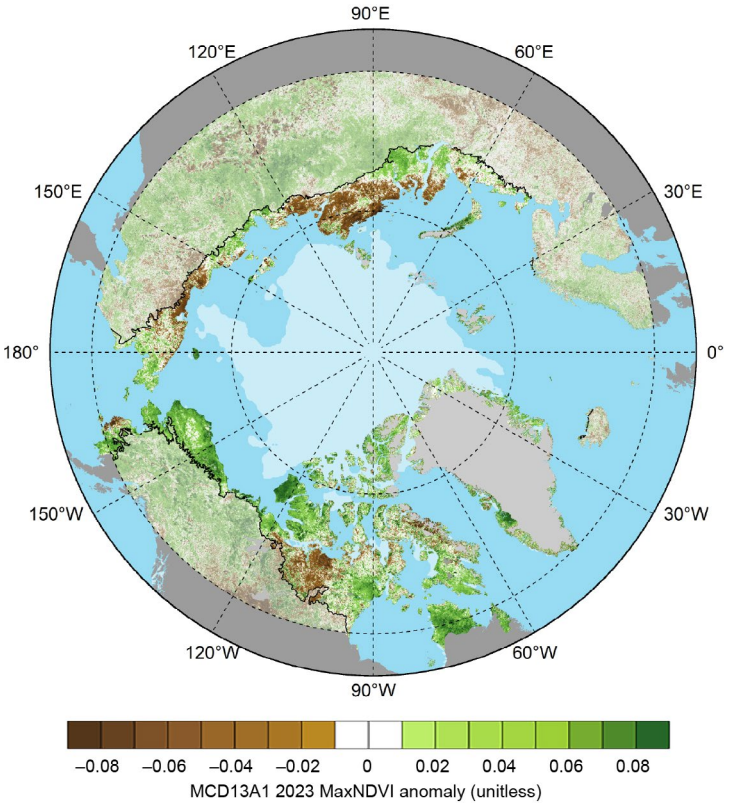

Fig. 5.33. Circumpolar maximum Normalized Difference Vegetation Index (MaxNDVI) anomalies for the 2023 growing season relative to mean values (2000–23) for Arctic tundra (solid colors) and boreal forest (muted colors) north of 60° latitude from the MODIS MCD13A1 dataset.

Earth-observing satellites provide foundational datasets for monitoring Arctic environmental change and help to overcome the long-standing barriers to access this region posed by its remoteness, along with new ones arising from the Russian invasion of Ukraine (López-Blanco et al. 2024). Nonetheless, field studies provide crucial information needed to connect spaceborne observations with patterns of change (or stability) on the ground. Increases in the abundance, distribution, and height of Arctic shrubs are a major driver of Arctic greening, and have important impacts on biodiversity, surface energy balance, permafrost temperatures, and biogeochemical cycling, particularly in the Low Arctic (Mekonnen et al. 2021). However, detailed vegetation datasets from colder tundra ecosystems of Victoria Island in the Canadian Arctic Archipelago reveal general increases in the cover of sedges and other herbaceous plants, but decreases in dwarf shrub cover from the early 1990s to circa 2020 (Schaefer 2023). While the driving of Artic greening by warming is likely to continue, ecological disturbances, extreme events, and other causes of browning are also increasing in frequency (Christensen et al. 2021; Magnússon et al. 2023). Understanding the regional variability of complex Arctic greening trends and attributing its drivers continues to be a subject of multi-disciplinary scientific research.

Appendix 1: Acronyms

ALT	active layer thickness
AVHRR	Advanced Very High Resolution Radiometer
Bclim	climatic mass balance
CCI	Climate Change Initiative
DU	Dobson unit
GRACE	Gravity Recovery and Climate Experiment
GRACE-FO	Gravity Recovery and Climate Experiment Follow-on
MaxNDVI	Maximum Normalized Difference Vegetation Index
MLS	microwave limb sounder
MODIS	Moderate Resolution Imaging Spectroradiometer
NDVI	Normalized Difference Vegetation Index
NSIDC	National Snow and Ice Data Center
OMI	Ozone Monitoring Instrument
PCH	polar cap averaged geopotential heights
PROMICE	Programme for Monitoring of the Greenland Ice Sheet
SCD	snow-cover duration
SCE	snow-cover extent
SLP	sea-level pressure
SMB	surface mass balance
SSMIS	Special Sensor Microwave Imager/Sounder
SST	sea-surface temperature
SSW	sudden stratospheric warming
SWE	snow water equivalent
TOC	total ozone column
UV	ultraviolet
UVI	ultraviolet index
VIIRS	Visible Infrared Imaging Radiometer Suite
WMO	World Meteorological Organization

Appendix 2: Datasets and sources

Section 5b Atmosphere

Sub-section	General Variable or Phenomenon	Specific dataset or variable	Source
5b, 5b1, 5b2	Geopotential Height	ERA5	https://www.ecmwf.int/en/forecasts/dataset/ecmwf-reanalysis-v5
5b2	Ozone, Total Column and Stratospheric	Aura OMI/MLS	https://disc.gsfc.nasa.gov/datasets/ML2O3_004/summary
5b2	Ozone, Total Column and Stratospheric	Bodeker Scientific	http://www.bodekerscientific.com/data/total-column-ozone
5b2	Ozone, Total Column and Stratospheric	OMTO3	https://disc.gsfc.nasa.gov/datasets/OMTO3_003/summary

Section 5c Surface air temperature

Sub-section	General Variable or Phenomenon	Specific dataset or variable	Source
5c2	Temperature, [Near] Surface	NASA GISTEMP v4	https://data.giss.nasa.gov/gistemp/
5c3	Temperature, [Near] Surface	ERA5	https://www.ecmwf.int/en/forecasts/dataset/ecmwf-reanalysis-v5
5c3	Pressure, Sea Level or Near-Surface	ERA5	https://www.ecmwf.int/en/forecasts/dataset/ecmwf-reanalysis-v5

Section 5d Precipitation

Sub-section	General Variable or Phenomenon	Specific dataset or variable	Source
5d2, 5d3, 5d4, 5d5	Precipitation	ERA5	https://www.ecmwf.int/en/forecasts/dataset/ecmwf-reanalysis-v5
5d4	Precipitation	GPCC	https://opendata.dwd.de/climate_environment/GPCC/html/download_gate.html

Section 5e Sea-surface temperature

Sub-section	General Variable or Phenomenon	Specific dataset or variable	Source
5e	Sea Surface Temperature	NOAA Optimum Interpolation SST (OISST) v2	https://www.ncei.noaa.gov/products/optimum-interpolation-sst
5e	Sea Ice Concentration	NOAA NSIDC Climate Data Record of Passive Microwave Sea Ice Concentration, Version 4	https://nsidc.org/data/g02202
5e	Sea Ice Concentration	NOAA/NSIDC Climate Data Record of Passive Microwave Sea Ice Concentration, Version 2	https://nsidc.org/data/g10016

Section 5f Sea ice

Sub-section	General Variable or Phenomenon	Specific dataset or variable	Source
5f1	Sea Ice Extent	NSIDC Sea Ice Extent	https://nsidc.org/data/g02135
5f2	Sea Ice Thickness	Cryosat-2/SMOS	https://earth.esa.int/eogateway/catalog/smos-cryosat-l4-sea-ice-thickness
5f2	Sea Ice Thickness	ICESat-2	https://icesat-2.gsfc.nasa.gov/icesat-2-data

Section 5g Greenland Ice Sheet

Sub-section	General Variable or Phenomenon	Specific dataset or variable	Source
5g	Albedo	MODIS (Greenland)	https://nsidc.org/data/MODGRNLD/versions/1
5g	Glacier Ablation	PROMICE Glacier Front Line (Greenland)	https://doi.org/10.22008/promice/data/calving_front_lines
5g	Glacier Mass, Area or Volume	Gravity Recovery and Climate Experiment Follow-on (GRACE/GRACE-FO)	https://grace.jpl.nasa.gov/data/get-data/
5g	Air temperature	DMI/PROMICE Weather Stations	https://eng.geus.dk/products-services-facilities/data-and-maps/glaciological-data-from-greenland-promice
5g	Ice Sheet Melt	Special Sensor Microwave Imager/Sounder (SSMIS)	https://nsidc.org/data/nsidc-0001

Sub-section	General Variable or Phenomenon	Specific dataset or variable	Source
5g	Ice Sheet Albedo	Moderate Resolution Imaging Spectroradiometer (MODIS)	https://nsidc.org/data/MODGRNLD/versions/1
5g	Ice Sheet Albedo	Sentinel-3 Snow and Ice Products (SICE)	https://eo4society.esa.int/projects/pre-operational-sentinel-3-snow-and-ice-products-sice/
5g	Ice Sheet Surface-Height	ICESat-2	https://icesat-2.gsfc.nasa.gov/icesat-2-data
5g	Ice Sheet Discharge	Ice Discharge (Greenland)	https://doi.org/10.22008/promice/data/ice_discharge/d/v02
5g	Ice Sheet Surface Mass Balance	Modèle Atmosphérique Régionale surface mass	https://mar.cnrs.fr/

Section 5h Glaciers and ice caps outside Greenland

Sub-section	General Variable or Phenomenon	Specific dataset or variable	Source
5h	Glacier Mass, Area or Volume	World Glacier Monitoring Service	http://dx.doi.org/10.5904/wgms-fog-2022-09
5h	Glacier Mass, Area or Volume	Gravity Recovery and Climate Experiment Follow-on (GRACE/GRACE-FO)	https://grace.jpl.nasa.gov/data/get-data/

Section 5i Terrestrial snow cover

Sub-section	General Variable or Phenomenon	Specific dataset or variable	Source
5i	Snow Properties	Crocus Snowpack Model	http://www.umr-cnrm.fr/spip.php?article265
5i	Snow Properties	ERA5	https://www.ecmwf.int/en/forecasts/dataset/ecmwf-reanalysis-v5
5i	Snow Properties	MERRA-2	http://gmao.gsfc.nasa.gov/reanalysis/MERRA-2/
5i	Snow Properties	European Space Agency Snow CCI SWE	https://snow-cci.enveo.at/
5i	Snow Properties	NOAA Interactive Multi-sensor Snow and Ice Mapping System (Snow Cover Duration)	https://usicecenter.gov/Products/ImsHome
5i	Snow Properties	Northern Hemisphere (NH) Snow Cover Extent (SCE), Version 1	http://doi.org/10.7289/V5N014G9

Section 5j Permafrost

Sub-section	General Variable or Phenomenon	Specific dataset or variable	Source
5i1	Permafrost	Global Terrestrial Network for Permafrost (GTN-P)	http://gtnpdatabase.org/
5i1	Permafrost	Permafrost Temperature	http://permafrost.gi.alaska.edu/sites_map
5i1	Temperature, [Near] Surface	ERA5	https://www.ecmwf.int/en/forecasts/dataset/ecmwf-reanalysis-v5
5i2	Permafrost	CALM Active Layer Thickness	www2.gwu.edu/~calm/

Section 5k Tundra greenness

Sub-section	General Variable or Phenomenon	Specific dataset or variable	Source
5k	Vegetative Index	Global Inventory Modeling and Mapping Studies (GIMMS) 3gv1	https://iridl.ldeo.columbia.edu/SOURCES/.NASA/.ARC/.ECOCAST/.GIMMS/.NDVI3g/.v1p0/index.htm
5k	Vegetative Index	MODIS Normalized Difference Vegetative Index (NDVI)	https://modis.gsfc.nasa.gov/data/dataprod/mod13.php

Sidebar 5.1: The February 2023 major sudden stratospheric warming

Sub-section	General Variable or Phenomenon	Specific dataset or variable	Source
SB5.1	Temperature, [Near] Surface	ERA5	https://www.ecmwf.int/en/forecasts/dataset/ecmwf-reanalysis-v5
SB5.1	Pressure	ERA5	https://www.ecmwf.int/en/forecasts/dataset/ecmwf-reanalysis-v5
SB5.1	Heat Flux	ERA5	https://www.ecmwf.int/en/forecasts/dataset/ecmwf-reanalysis-v5
SB5.1	Stratospheric Water vapor	Aura Microwave Limb Sounder (MLS)	https://gmao.gsfc.nasa.gov/reanalysis/MERRA-2/
SB5.1	Water Vapor, Total Column	MERRA-2	https://gmao.gsfc.nasa.gov/reanalysis/MERRA-2/

References

Afargan-Gerstman, H., B. Jiménez-Esteve, and D. I. V. Domeisen, 2022: On the relative importance of stratospheric and tropospheric drivers for the North Atlantic jet response to sudden stratospheric warming events. *J. Climate*, **35**, 6453–6467, https://doi.org/10.1175/JCLI-D-21-0680.1.

Arctic Climate Forum, 2023: 12th Arctic Climate Forum. Virtual, NOAA, https://www.arctic-rcc.org/acf-fall-2023.

Ballinger, T. J., and Coauthors, 2022: Surface air temperature. Arctic Report Card 2022, M. L. Druckenmiller, R. L. Thoman, and T. A. Moon, Eds., NOAA Tech. Rep. OAR ARC 22-02, 8–14, https://doi.org/10.25923/13qm-2576.

—— , and Coauthors, 2023: Alaska terrestrial and marine climate trends, 1957–2021. *J. Climate*, **36**, 4375–4391, https://doi.org/10.1175/JCLI-D-22-0434.1.

Barents Observer, 2023: Climate change brings cloudberry to Svalbard. Barents Observer, 3 October, https://thebarentsobserver.com/en/arctic/2023/10/climate-change-brings-cloudberry-svalbard.

Barrett, A. P., J. C. Stroeve, and M. C. Serreze, 2020: Arctic Ocean precipitation from atmospheric reanalyses and comparisons with North Pole drifting stations. *J. Geophys. Res. Oceans*, **125**, e2019JC015415, https://doi.org/10.1029/2019JC015415.

Becker, A., P. Finger, A. Meyer-Christoffer, B. Rudolf, K. Schamm, U. Schneider, and M. Ziese, 2013: A description of the global land-surface precipitation data products of the Global Precipitation Climatology Centre with sample applications including centennial (trend) analysis from 1901–present. *Earth Syst. Sci. Data*, **5**, 71–99, https://doi.org/10.5194/essd-5-71-2013.

Behrangi, A., A. Singh, Y. Song, and M. Panahi, 2019: Assessing gauge undercatch corrections in Arctic basins in light of GRACE observations. *Geophyis. Res. Lett.*, **46**, 11358–11366, https://doi.org/10.1029/2019GL084221.

Berner, L. T., and S. J. Goetz, 2022: Satellite observations document trends consistent with a boreal forest biome shift. *Global Change Biol.*, **28**, 3275–3292, https://doi.org/10.1111/gcb.16121.

Bernhard, G. H., A. F. Bais, P. J. Aucamp, A. R. Klekociuk, J. B. Liley, and R. L. McKenzie, 2023: Stratospheric ozone, UV radiation, and climate interactions. *Photochem. Photobiol. Sci.*, **22**, 937–989, https://doi.org/10.1007/s43630-023-00371-y.

Bhartia, P. K., and C. W. Wellemeyer, 2002: TOMS-V8 total O3 algorithm. OMI Algorithm Theoretical Basis Document Vol. II, NASA Goddard Space Flight Center Tech. Doc. ATBD-OMI-02, 15–31, https://eospso.gsfc.nasa.gov/sites/default/files/atbd/ATBD-OMI-02.pdf.

Bhatt, U. S., and Coauthors, 2021: Climate drivers of Arctic tundra variability and change using an indicators framework. *Environ. Res. Lett.*, **16**, 055019, https://doi.org/10.1088/1748-9326/abe676.

Bodeker, G. E., and S. Kremser, 2021: Indicators of Antarctic ozone depletion: 1979 to 2019. *Atmos. Chem. Phys.*, **21**, 5289–5300, https://doi.org/10.5194/acp-21-5289-2021.

Box, J. E., D. van As, and K. Steffen, 2017: Greenland, Canadian and Icelandic land-ice albedo grids (2000–2016). GEUS Bull., **38**, 53–56, https://doi.org/10.34194/geusb.v38.4414.

—— , W. Colgan, B. Wouters, D. Burgess, S. O'Neel, L. Thomson, and S. Mernild, 2018: Global sea-level contribution from Arctic land ice: 1971–2017. *Environ. Res. Lett.*, **13**, 125012, https://doi.org/10.1088/1748-9326/aaf2ed.

—— , and Coauthors, 2019: Key indicators of Arctic climate change: 1971–2017. *Environ. Res. Lett.*, **14**, 045010, https://doi.org/10.1088/1748-9326/aafc1b.

—— , and Coauthors, 2021: Recent developments in Arctic climate observational indicators. AMAP Arctic Climate Change Update 2021: Key Trends and Impacts, Arctic Monitoring and Assessment Programme, 7–29, https://www.amap.no/documents/doc/arctic-climate-change-update-2021-key-trends-and-impacts.-summary-for-policy-makers/3508.

Brown, R., D. V. Schuler, O. Bulygina, C. Derksen, K. L. Wang, and D. Yang, 2017: Arctic terrestrial snow cover. Snow, Water, Ice and Permafrost in the Arctic (SWIPA) 2017, Arctic, Monitoring and Assessment Programme, 25–64, https://www.amap.no/documents/doc/snow-water-ice-and-permafrost-in-the-arctic-swipa-2017/1610.

Brun, E., V. Vionnet, A. Boone, B. Decharme, Y. Peings, R. Valette, F. Karbou, and S. Morin, 2013: Simulation of northern Eurasian local snow depth, mass, and density using a detailed snowpack model and meteorological reanalyses. *J. Hydrometeor.*, **14**, 203–219, https://doi.org/10.1175/JHM-D-12-012.1.

Butchart, N., and E. E. Remsberg, 1986: The area of the stratospheric polar vortex as a diagnostic for tracer transport on an isentropic surface. *J. Atmos. Sci.*, **43**, 1319–1339, https://doi.org/10.1175/1520-0469(1986)043<1319:TAOTSP>2.0.CO;2.

CBC News, 2023: Enterprise, N.W.T., '90 per cent gone' after wildfire ravages community. Accessed 10 February 2024, https://www.cbc.ca/news/canada/north/enterprise-damage-wildfire-1.6936652.

Christensen, T. R., and Coauthors, 2021: Multiple ecosystem effects of extreme weather events in the Arctic. *Ecosystems*, **24**, 122–136, https://doi.org/10.1007/s10021-020-00507-6.

Ciracì, E., I. Velicogna, and S. Swenson, 2020: Continuity of the mass loss of the world's glaciers and ice caps from the GRACE and GRACE Follow-On missions. *Geophys. Res. Lett.*, **47**, e2019GL086926, https://doi.org/10.1029/2019GL086926.

Cohen, J., and Coauthors, 2020: Divergent consensuses on Arctic amplification influence on midlatitude severe winter weather. Nat. Climate Change, 10, 20–29, https://doi.org/10.1038/s41558-019-0662-y.

Colgan, W., and Coauthors, 2015: Hybrid glacier Inventory, Gravimetry and Altimetry (HIGA) mass balance product for Greenland and the Canadian Arctic. *Remote Sens. Environ.*, **168**, 24–39, https://doi.org/10.1016/j.rse.2015.06.016.

Didan, K., 2021a: MODIS/terra vegetation indices 16-day L3 global 500m SIN grid V061 [Data set]. NASA EOSDIS Land Processes DAAC, accessed 27 February 2023, https://doi.org/10.5067/MODIS/MOD13A1.061.

—— , 2021b: MODIS/aqua vegetation indices 16-day L3 global 500m SIN Grid V061 [Data set]. NASA EOSDIS Land Processes DAAC, accessed 27 February 2023, https://doi.org/10.5067/MODIS/MYD13A1.061.

Domeisen, D. I. V, and Coauthors, 2020: The role of the stratosphere in subseasonal to seasonal prediction: 2. *Predictability arising from stratosphere?troposphere coupling. J. Geophys. Res. Atmos.*, **125**, e2019JD030923, https://doi.org/10.1029/2019JD030923.

DW, 2023: Storm 'Hans' batters Scandinavia. DW, accessed 20 February 2024, https://www.dw.com/en/storm-hans-batters-scandinavia/a-66477645.

ESA, 2023: European Space Agency SMOS-CryoSat L4 sea ice thickness, version 206 accessed 3 October 2023, https://doi.org/10.57780/sm1-4f787c3.[463151][MLD2]

Fausto, R. S., and Coauthors, 2021: Programme for Monitoring of the Greenland Ice Sheet (PROMICE) automatic weather station data. *Earth Syst. Sci. Data*, **13**, 3819–3845, https://doi.org/10.5194/essd-13-3819-2021.

Fetterer, F., K. Knowles, W. N. Meier, M. Savoie, and A. K. Windnagel, 2017: Sea Ice Index, version 3 (updated daily). National Snow and Ice Data Center, accessed 27 August 2021, https://doi.org/10.7265/N5K072F8.

Fettweis, X., and Coauthors, 2020: GrSMBMIP: Intercomparison of the modelled 1980–012 surface mass balance over the Greenland Ice Sheet. *Cryosphere*, **14**, 3935–3958, https://doi.org/10.5194/tc-14-3935-2020.

Friedel, M., G. Chiodo, A. Stenke, D. I. V. Domeisen, and T. Peter, 2022: Effects of Arctic ozone on the stratospheric spring onset and its surface impact. *Atmos. Chem. Phys.*, **22**, 13 997–14 017, https://doi.org/10.5194/acp-22-13997-2022.

Garfinkel, C. I., D. L. Hartmann, and F. Sassi, 2010: Tropospheric precursors of anomalous Northern Hemisphere stratospheric polar vortices. *J. Climate*, **23**, 3282–3299, https://doi.org/10.1175/2010JCLI3010.1.

GMAO, 2015a: MERRA-2 inst3_3d_asm_nv: 3d, 3-hourly, instantaneous, model-level, assimilation, assimilated meteorological fields v5.12.4. Goddard Earth Sciences Data and Information Services Center (GES DISC), accessed 3 August 2023, https://doi.org/10.5067/WWQSXQ8IVFW8.

——, 2015b: MERRA-2tavg1_2d_lnd_Nx:2d, 1-hourly, time-averaged, single-level, assimilation, land surface diagnostics V5.12.4. Goddard Earth Sciences Data and Information Services Center (GESDISC), accessed 3 August 2023, https://doi.org/10.5067/RKPHT8KC1Y1T.

——, 2022: M2-SCREAM: 3d, 3-hourly, instantaneous, model-level, assimilation, assimilated constituent fields, replayed MERRA-2 meteorological fields. Goddard Earth Sciences Data and Information Services Center (GES DISC), accessed 3 August 2023, https://doi.org/10.5067/7PR3XRD6Q3NQ.

Hersbach, H., and Coauthors, 2020: The ERA5 global reanalysis. *Quart. J. Roy. Meteor. Soc.*, **146**, 1999–2049, https://doi.org/10.1002/qj.3803.

——, and Coauthors, 2023a: ERA5 hourly data on pressure levels from 1940 to present. Copernicus Climate Change Service (C3S) Climate Data Store (CDS[NR3][MLD4]), accessed 7 February 2024, https://doi.org/10.24381/cds.bd0915c6.

——, and Coauthors, 2023b: ERA5 hourly data on single levels from 1940 to present. Copernicus Climate Change Service (C3S) Climate Data Store (CDS[NR5][MLD6]), accessed 7 February 2024, https://doi.org/10.24381/cds.adbb2d47.

High North News, 2023: China pushes northern sea route transit cargo to new record. Accessed 10 February 2024, https://www.highnorthnews.com/en/china-pushes-northern-sea-route-transit-cargo-new-record.

Hjort, J., D. Streletskiy, G. Doré, Q. Wu, K. Bjella, and M. Luoto, 2022: Impacts of permafrost degradation on infrastructure. *Nat. Rev. Earth Environ.*, **3**, 24–38, https://doi.org/10.1038/s43017-021-00247-8.

Huang, B., C. Liu, V. Banzon, E. Freeman, G. Graham, B. Hankins, T. Smith, and H. Zhang, 2021: Improvements of the Daily Optimum Interpolation Sea Surface Temperature (DOISST) version 2.1. *J. Climate*, **34**, 2923–2939, https://doi.org/10.1175/JCLI-D-20-0166.1.

Hugonnet, R., and Coauthors, 2021: Accelerated global glacier mass loss in the early twenty-first century. *Nature*, **592**, 726–731, https://doi.org/10.1038/s41586-021-03436-z.

Icelandic Met Office, 2023: Flood in Skaftá. Accessed 8 February 2024, https://en.vedur.is/about-imo/news/flood-in-skafta.

Isaksen, K., and Coauthors, 2022a: Exceptional warming over the Barents area. *Sci. Rep.*, **12**, 9371, https://doi.org/10.1038/s41598-022-13568-5.

——, J. Lutz, A. M. Sorensen, O. Godoy, L. Ferrighi, S. Eastwood, and S. Aaboe, 2022b: Advances in operational permafrost monitoring on Svalbard and in Norway. *Environ. Res. Lett.*, **17**, 095012, https://doi.org/10.1088/1748-9326/ac8e1c.

Ivanova, N., O. M. Johannessen, L. T. Pedersen, and R. T. Tonboe, 2014: Retrieval of Arctic sea ice parameters by satellite passive microwave sensors: A comparison of eleven sea ice concentration algorithms. *IEEE Trans. Geosci. Remote Sens.*, **52**, 7233–7246, https://doi.org/10.1109/TGRS.2014.2310136.

Jóhannesson, T., H. Björnsson, E. Magnússon, S. Gu?mundsson, F. Pálsson, O. Sigur?sson, T. Thorsteinsson, and E. Berthierand, 2013: Ice-volume changes, bias estimation of mass-balance measurements and changes in subglacial lakes derived by lidar mapping of the surface of Icelandic glaciers. *Ann. Glaciol.*, **54**, 63–74, https://doi.org/10.3189/2013AoG63A422.

Karpechko, A. Y., P. Hitchcock, D. H. Peters, and A. Schneidereit, 2017: Predictability of downward propagation of major sudden stratospheric warmings. *Quart. J. Roy. Meteor. Soc.*, **143**, 1459–1470, https://doi.org/10.1002/qj.3017.

Kaverin, D., and Coauthors, 2021: Long-term active layer monitoring at CALM sites in the Russian European North. *Polar Geogr.*, **44**, 203–216, https://doi.org/10.1080/1088937X.2021.1981476.

Kjøllmoen, B., Ed., L. M. Andreassen, and H. Elvehøy, 2023: Glaciological investigations in Norway 2022. NVE Rapport 23-2023, 100 pp., https://publikasjoner.nve.no/rapport/2023/rapport2023_23.pdf.

Kokhanovsky, A., J. E. Box, B. Vandecrux, K. D. Mankoff, M. Lamare, A. Smirnov, and M. Kern, 2020: The determination of snow albedo from satellite measurements using fast atmospheric correction technique. Remote Sens., 12, 234, https://doi.org/10.3390/rs12020234.

Lambert, A., N. Livesey, W. Read, and R. Fuller, 2021: MLS/Aura level 3 daily binned water vapor (H2O) mixing ratio on zonal and similar grids V005. Goddard Earth Sciences Data and Information Services Center (GES DISC[NR7][MLD8]), accessed 26 February 2024, https://doi.org/10.5067/Aura/MLS/DATA3568.

Larson, C., and M. Sabbatini, 2023: Record flooding from Suicide Basin destroys one home, swamps others and cuts off access. Juneau Empire, 6 August, accessed 21 February 2024, https://www.juneauempire.com/news/record-flooding-from-suicide-basin-swamps-homes-cuts-off-access/.

Lavergne, T., and Coauthors, 2019: Version 2 of the EUMETSAT OSI SAF and ESA CCI sea-ice concentration climate data records. *Cryosphere*, **13**, 49–78, https://doi.org/10.5194/tc-13-49-2019.

LEO Network, 2023: Rain continues to impact the Noatak River. Accessed 10 February 2024, https://www.leonetwork.org/en/posts/show/F7361480-8E14-44C2-B42A-FED1F3D9AED4.

Loeb, N. G., M. Mayer, S. Kato, J. T. Fasullo, H. Zuo, R. Senan, J. M. Lyman, G. C. Johnson, and M. Balmaseda, 2022: Evaluating twenty-year trends in Earth's energy flows from observations and reanalyses. *J. Geophys. Res. Atmospheres*, **127**, e2022JD036686, https://doi.org/10.1029/2022JD036686.

López-Blanco, E., and Coauthors, 2024: Towards an increasingly biased view on Arctic change. *Nat. Climate Change*, **14**, 152–155, https://doi.org/10.1038/s41558-023-01903-1.

Luojus, K., and Coauthors, 2022: ESA Snow Climate Change Initiative (Snow_cci): Snow Water Equivalent (SWE) level 3C daily global climate research data package (CRDP) (1979–2020), version 2.0. NERC EDS Centre for Environmental Data Analysis, accessed 27 August 2023, https://doi.org/10.5285/4647cc9ad3c044439d6c643208d3c494.

Magnússon, R. Í., F. Groten, H. Bartholomeus, K. Van Huissteden, and M. M. P. D. Heijmans, 2023: Tundra browning in the Indigirka Lowlands (north?eastern Siberia) explained by drought, floods and small?scale vegetation shifts. *J. Geophys. Res. Biogeosci.*, **128**, e2022JG007330, https://doi.org/10.1029/2022JG007330.

Malkova, G., and Coauthors, 2022: Spatial and temporal variability of permafrost in the western part of the Russian Arctic. *Energies*, **15**, 2311, https://doi.org/10.3390/en15072311.

Mankoff, K. D., A. Solgaard, W. Colgan, A. P. Ahlstrøm, S. A. Khan, and R. S. Fausto, 2020: Greenland Ice Sheet solid ice discharge from 1986 through March 2020. *Earth Syst. Sci. Data*, **12**, 1367–1383, https://doi.org/10.5194/essd-12-1367-2020.

Martius, O., L. M. Polvani, and H. C. Davies, 2009: Blocking precursors to stratospheric sudden warming events. *Geophys. Res. Lett.*, **36**, L14806, https://doi.org/10.1029/2009GL038776.

McCague, F., 2023: Record year in the Northwest Passage as part of busy Arctic season. Chartered Institute of Logistics and Transport, 30 October, accessed 10 February 2024, https://ciltna.com/2023/10/30/record-year-in-the-northwest-passage-as-part-of-busy-arctic-season-by-fred-mccague-cmilt/.

Meier, W. N., F. Fetterer, A. K. Windnagel, and J. S. Stewart, 2021a: NOAA/NSIDC Climate Data Record of passive microwave sea ice concentration, version 4. National Snow and Ice Data Center, accessed 10 September 2022, https://doi.org/10.7265/efmz-2t65.

—— , —— , —— , and —— , 2021b: Near-real-time NOAA/NSIDC Climate Data Record of passive microwave sea ice concentration, version 2. National Snow and Ice Data Center, accessed 5 February 2024, https://doi.org/10.7265/tgam-yv28.

Mekonnen, Z. A., and Coauthors, 2021: Arctic tundra shrubification: A review of mechanisms and impacts on ecosystem carbon balance. *Environ. Res. Lett.*, **16**, 053001, https://doi.org/10.1088/1748-9326/abf28b.

Meredith, M., and Coauthors, 2019: Polar regions. The Ocean and Cryosphere in a Changing Climate, H.-O. Pörtner et al., Eds., Cambridge University Press, 203–320, https://doi.org/10.1017/9781009157964.005.

Millán, L., and Coauthors, 2022: The Hunga Tonga?Hunga Ha'apai hydration of the stratosphere. *Geophys. Res. Lett.*, **49**, e2022GL099381, https://doi.org/10.1029/2022GL099381.

Miner, K. R., and Coauthors, 2022: Permafrost carbon emissions in a changing Arctic. *Nat. Rev. Earth Environ.*, **3**, 55–67, https://doi.org/10.1038/s43017-021-00230-3.

Moon, T. A., and Coauthors, 2019: The expanding footprint of rapid Arctic change. *Earth's Future*, **7**, 212–218, https://doi.org/10.1029/2018EF001088.

—— , R. Thoman, and M. L. Druckenmiller, Eds., 2023: The Arctic [in "State of the Climate in 2022"]. *Bull. Amer. Meteor. Soc.*, **104** (9), S271–S321, https://doi.org/10.1175/BAMS-D-23-0079.1.

Mote, T., 2007: Greenland surface melt trends 1973–2007: Evidence of a large increase in 2007. *Geophys. Res. Lett.*, **34**, L22507, https://doi.org/10.1029/2007GL031976.

Müller, R., J.-U. Grooß, C. Lemmen, D. Heinze, M. Dameris, and G. Bodeker, 2008: Simple measures of ozone depletion in the polar stratosphere. *Atmos. Chem. Phys.*, **8**, 251–264, https://doi.org/10.5194/acp-8-251-2008.

Muñoz Sabater, J., 2019: ERA5-Land hourly data from 1981 to present. Copernicus Climate Change Service (C3S) Climate Data Store (CDS), accessed 3 October 2023, https://doi.org/10.24381/cds.e2161bac.

NOAA, 2024a: Optimum Interpolation Sea Surface Temperature (OISST) high resolution dataset, version 2.1. NOAA/PSL[NR9][MD10], accessed 5 February 2024, https://psl.noaa.gov/data/gridded/data.noaa.oisst.v2.highres.html.

—— , 2024b: North American Drought Monitor (MADM) map. NOAA/NCEI, accessed 8 February 2024, https://www.ncei.noaa.gov/access/monitoring/nadm/maps.

Nyland, K. E., N. I. Shiklomanov, D. A. Streletskiy, F. E. Nelson, A. E. Klene, and A. L. Kholodov, 2021: Long-term Circumpolar Active Layer Monitoring (CALM) program observations in Northern Alaskan tundra. *Polar Geogr.*, **44**, 167–185, https://doi.org/10.1080/1088937X.2021.1988000.

O'Neill, H. B., S. L. Smith, C. R. Burn, C. Duchesne, and Y. Zhang, 2023: Widespread permafrost degradation and thaw subsidence in northwest Canada. *J. Geophys. Res.: Earth Surf.*, **128**, e2023JF007262, https://doi.org/10.1029/2023JF007262.

Peng, G., W. N. Meier, D. J. Scott, and M. H. Savoie, 2013: A long-term and reproducible passive microwave sea ice concentration data record for climate studies and monitoring. *Earth Syst. Sci. Data*, **5**, 311–318, https://doi.org/10.5194/essd-5-311-2013.

Petty, A. A., N. T. Kurtz, R. Kwok, T. Markus, and T. A. Neumann, 2020: Winter Arctic sea ice thickness from ICESat?2 freeboards. *J. Geophys. Res. Oceans*, **125**, e2019JC015764, https://doi.org/10.1029/2019JC015764.

—— , N. Keeney, A. Cabaj, P. Kushner, and M. Bagnardi, 2023a: Winter Arctic sea ice thickness from ICESat-2: Upgrades to freeboard and snow loading estimates and an assessment of the first three winters of data collection. *Cryosphere*, **17**, 127–156, https://doi.org/10.5194/tc-17-127-2023.

—— , N. Kurtz, R. Kwok, T. Markus, and T. A. Neumann, and N. Keeney, 2023b: ICESat-2 L4 monthly gridded sea ice thickness, version 3. NASA National Snow and Ice Data Center Distributed Active Archive Center, accessed December 2023, https://doi.org/10.5067/ZCSU8Y5U1BQW.

Pinzon, J. E., C. J. Tucker, U. S. Bhatt, G. V. Frost, and M. J. Macander, 2023: Global Vegetation Greenness (NDVI) from AVHRR GIMMS-3G+, 1981-2022. ORNL DAAC[NR11][MLD12], accessed 20 May 2024, https://doi.org/10.3334/ORNLDAAC/2187.

Polvani, L. M., M. Previdi, M. R. England, G. Chiodo, and K. L. Smith, 2020: Substantial twentieth-century Arctic warming caused by ozone-depleting substances. *Nat. Climate Change*, **10**, 167, https://doi.org/10.1038/s41558-020-0711-6.

Raynolds, M. K., and Coauthors, 2019: A raster version of the Circumpolar Arctic Vegetation Map (CAVM). Remote Sens. *Environ.*, **232**, 111297, https://doi.org/10.1016/j.rse.2019.111297.

Reuters, 2023: Smoke from forest fires engulfs city in Russia's far east. 9 August, accessed 20 March 2024, https://www.reuters.com/world/europe/smoke-forest-fires-engulfs-city-russias-far-east-2023-08-09/.

Reynolds, R. W., N. A. Rayner, T. M. Smith, D. C. Stokes, and W. Wang, 2002: An improved in situ and satellite SST analysis for climate. *J. Climate*, **15**, 1609–1625, https://doi.org/10.1175/1520-0442(2002)015<1609:AIISAS>2.0.CO;2.

—— , T. M. Smith, C. Liu, D. B. Chelton, K. S. Casey, and M. G. Schlax, 2007: Daily high-resolution-blended analyses for sea surface temperature. *J. Climate*, **20**, 5473–5496, https://doi.org/10.1175/2007JCLI1824.1.

RGI Consortium, 2023: Randolph Glacier Inventory – A dataset of global glacier outlines, version 7.0. National Snow and Ice Data Center[NR13][MLD14], accessed 16 October 2024, https://doi.org/10.5067/f6jmovy5navz.

Ricker, R., S. Hendricks, L. Kaleschke, X. Tian-Kunze, J. King, and C. Haas, 2017: A weekly Arctic sea-ice thickness data record from merged CryoSat-2 and SMOS satellite data. *Cryosphere*, **11**, 1607–1623, https://doi.org/10.5194/tc-11-1607-2017.

Robinson, D. A., T. W. Estilow, and NOAA CDR Program, 2012: NOAA Climate Data Record (CDR) of Northern Hemisphere (NH) Snow Cover Extent (SCE), version 1. NOAA National Centers for Environmental Information, accessed 3 August 2023, https://doi.org/10.7289/V5N014G9.

Román, M. O., and Coauthors, 2024: Continuity between NASA MODIS Collection 6.1 and VIIRS Collection 2 land products. *Remote Sens. Environ.*, **302**, 113963, https://doi.org/10.1016/j.rse.2023.113963.

Romanovsky, V., and Coauthors, 2017: Changing permafrost and its impacts. Snow, Water, Ice and Permafrost in the Arctic (SWIPA) 2017, Arctic Monitoring and Assessment Programme, 65–102, https://www.amap.no/documents/doc/snow-water-ice-and-permafrost-in-the-arctic-swipa-2017/1610.

Schaefer, J. A., 2023: Increases in graminoids after three decades of change in the High Arctic. Polar Res., 42, https://doi.org/10.33265/polar.v42.9560.

Schneider, U., P. Finger, E. Rustemeier, M. Ziese, and S. Hänsel, 2022: Global precipitation analysis products of the GPCC. DWD, 17 pp., https://opendata.dwd.de/climate_environment/GPCC/PDF/GPCC_intro_products_v2022.pdf.

Schoeberl, M. R., Y. Wang, R. Ueyama, A. Dessler, G. Taha, and W. Yu, 2023: The estimated climate impact of the Hunga Tonga-Hunga Ha'apai eruption plume. *Geophy. Res. Lett.*, **50**, e2023GL104634, https://doi.org/10.1029/2023GL104634.

Schuur, E. A. G., and Coauthors, 2022: Permafrost and climate change: Carbon cycle feedbacks from the warming Arctic. *Annu. Rev. Environ. Resour.*, **47**, 343–371, https://doi.org/10.1146/annurev-environ-012220-011847.

Sciencenorway.no, 2024: Svalbard in 2023: Record hot, record cold, record wet, and record dry. 8 January, accessed 22 February 2024, https://www.sciencenorway.no/climate-ntb-english-svalbard/svalbard-in-2023-record-hot-record-cold-record-wet-and-record-dry/2304908.

Serreze, M. C., and R. G. Barry, 2011: Processes and impacts of Arctic amplification: A research synthesis. *Global Planet. Change*, **77**, 85–96, https://doi.org/10.1016/j.gloplacha.2011.03.004.

—— , M. P. Clark, and D. H. Bromwich, 2003: Monitoring precipitation over the Arctic terrestrial drainage system: Data requirements, shortcomings, and applications of atmospheric reanalysis. *J. Hydrometeor.*, **4**, 387–407, https://doi.org/10.1175/1525-7541(2003)4<387:MPOTAT>2.0.CO;2.

—— , J. Gustafson, A. P. Barrett, M. L. Druckenmiller, S. Fox, J. Voveris, J. Stroeve, B. Sheffield, B. C. Forbes, and S. Rasmus, 2021: Arctic rain on snow events: bridging observations to understand environmental and livelihood impacts. *Environ. Res. Lett.*, **16**, 105009, https://doi.org/10.1088/1748-9326/ac269b.

Skarin, A., Ö. Danell, R. Bergström, and J. Moen, 2004: Insect avoidance may override human disturbances in reindeer habitat selection. *Rangifer*, **24**, 95–103, https://doi.org/10.7557/2.24.2.306.

Smith, B., 2023: Algorithm Theoretical Basis Document (ATBD) for Land-ice DEM (ATL14) and Land-ice height change (ATL15). https://nsidc.org/sites/default/files/documents/technical-reference/icesat2_atl14_atl15_atbd_v003.pdf.

Smith, S. L., H. B. O'Neill, K. Isaksen, J. Noetzli, and V. E. Romanovsky, 2022: The changing thermal state of permafrost. *Nat. Rev. Earth Environ.*, **3**, 10–23, https://doi.org/10.1038/s43017-021-00240-1.

—— , V. E. Romanovsky, K. Isaken, K. Nyland, N. I. Shiklomanov, D. A. Streletskiy, and H. H. Christiansen, 2023: Permafrost [in "State of the Climate in 2022"]. *Bull. Amer. Meteor. Soc.*, **104** (9), S301–S305, https://doi.org/10.1175/10.1175/BAMS-D-23-0079.1.

—— , C. Duchesne, and H. B. O'Neill, 2024: Long-term permafrost monitoring in northern Canada – What have we learned? 12th Int. Conf. on Permafrost, Whitehorse, Yukon, Canada, Yukon University, 398–404, https://doi.org/10.52381/ICOP2024.84.1.

Tapley, B. D., and Coauthors, 2019: Contributions of GRACE to understanding climate change. *Nat. Climate Change*, **9**, 358–369, https://doi.org/10.1038/s41558-019-0456-2.

The Guardian, 2023: Storm Hans causes havoc in Norway with heaviest rain in 25 years forecast. Guardian, 9 August, https://www.theguardian.com/world/2023/aug/08/storm-hans-causes-havoc-in-norway-with-heaviest-rain-in-25-years-forecast.

Thoman, R. L., M. L. Druckenmiller, and T. Moon, Eds, 2022: The Arctic [in "State of the Climate in 2021"]. *Bull. Amer. Meteor. Soc.*, **103** (8), S257–S306, https://doi.org/10.1175/BAMS-D-22-0082.1.

—— , —— , and —— , Eds., 2023: Arctic Report Card 2023: Executive Summary. NOAA Tech. Rep. OAR ARC, 23-01, 5 pp., https://doi.org/10.25923/5vfa-k694.

Thompson, S., 2023: Remarks on September 28, 2023. Government of Northwest Territories, accessed 10 February 2024, https://www.gov.nt.ca/en/newsroom/shane-thompson-historic-2023-wildfire-season.

Timmermans, M.-L., and Z. M. Labe, 2023: Sea surface temperature. NOAA Arctic Report Card 2023, NOAA Tech. Rep. OAR ARC, 23-07, 7 pp., https://doi.org/10.25923/e8jc-f342.

Tschudi, M., W. N. Meier, and J. S. Stewart, 2019a: Quicklook Arctic weekly EASE-Grid Sea Ice Age, version 1. NASA National Snow and Ice Data Center Distributed Active Archive Center, accessed 1 September 2021, https://doi.org/10.5067/2XXGZY3DUGNQ.

—— , —— , —— , C. Fowler, and J. Maslanik, 2019b: EASE-Grid Sea Ice Age, version 4. NASA National Snow and Ice Data Center Distributed Active Archive Center, accessed 1 September 2021, https://doi.org/10.5067/UTAV7490FEPB.

U.S. National Ice Center, 2008: IMS daily Northern Hemisphere snow and ice analysis at 1 km, 4 km, and 24 km resolutions, version 1. National Snow and Ice Data Center, accessed 18 August 2023, https://doi.org/10.7265/N52R3PMC.

Walsh, J. E., T. J. Ballinger, E. S. Euskirchen, E. Hanna, J. Mård, J. E. Overland, H. Tangen, and T. Vihma, 2020: Extreme weather and climate events in northern areas: A review. *Earth-Sci. Rev.*, **209**, 103324, https://doi.org/10.1016/j.earscirev.2020.103324.

—— , S. Bigalke, S. A. McAfee, R. Lader, M. C. Serreze, and T. J. Ballinger, 2023: Precipitation [in "State of the Climate in 2022"]. *Bull. Amer. Meteor. Soc.*, **104** (9), S281–S284, https://doi.org/10.1175/BAMS-D-23-0079.1.

Wargan, K., B. Weir, G. L. Manney, S. E. Cohn, K. E. Knowland, P. A. Wales, and N. J. Livesey, 2023: M2-SCREAM: A stratospheric composition reanalysis of Aura MLS data with MERRA-2 transport. *Earth Space Sci.*, **10**, e2022EA002632, https://doi.org/10.1029/2022EA002632.

Wehrlé, A., J. E. Box, A. M. Anesio, and R. S. Fausto, 2021: Greenland bare-ice albedo from PROMICE automatic weather station measurements and Sentinel-3 satellite observations. *GEUS Bull.*, **47**, 5284, https://doi.org/10.34194/geusb.v47.5284.

WGMS, 2024: Fluctuations of glaciers database. World Glacier Monitoring Service[NR15][MLD16], accessed 6 February 2024, https://doi.org/10.5904/wgms-fog-2024-01.

White, J., J. E. Walsh, and R. L. Thoman Jr., 2021: Using Bayesian statistics to detect trends in Alaskan precipitation. *Int. J. Climatol.*, **41**, 2045–2059, https://doi.org/10.1002/joc.6946.

Wolken, G. J., and Coauthors, 2021: Glacier and permafrost hazards. Arctic Report Card 2021, NOAA Tech. Rep. OAR ARC; 21-13, 9 pp., https://doi.org/10.25923/v40r-0956.<<?CE: Please check and confirm the edits to the reference is correct>>

World Meteorological Organization, 2022: Scientific assessment of ozone depletion: 2022. WMO GAW Rep. 278, 509 pp.

Wouters, B., A. Gardner, and G. Moholdt, 2019: Global glacier mass loss during the GRACE Satellite Mission (2002-2016). Front. *Earth Sci.*, **7**, 96, https://doi.org/10.3389/feart.2019.00096.

Ye, H., D. Yang, A. Behrangi, S. L. Stuefer, X. Pan, E. Mekis, Y. Dibike, and J. E. Walsh, 2021: Precipitation characteristics and changes. Arctic Hydrology, Permafrost and Ecosystems, D. Yang and D. L. Kane, Eds., Springer, 25–59, https://doi.org/10.1007/978-3-030-50930-9_2.

Yu, L., and S. Zhong, 2021: Trends in Arctic seasonal and extreme precipitation in recent decades. *Theor. Appl. Climatol.*, **145**, 1541–1559, https://doi.org/10.1007/s00704-021-03717-7.

Zemp, M., and Coauthors, 2019: Global glacier mass changes and their contributions to sea-level rise from 1961 to 2016. *Nature*, **568**, 382–386, https://doi.org/10.1038/s41586-019-1071-0.

Zhu, X., X. Xu, and G. Jia, 2023: Recent massive expansion of wildfire and its impact on active layer over pan-Arctic permafrost. *Environ. Res. Lett.*, **18**, 084010, https://doi.org/10.1088/1748-9326/ace205.